Stony Brook University

Motion of Bubbles in Confined Microgeometries: Flow Behavior and CO_2 Dissolution Regimes

A Dissertation Presented

by

Martin Sauzade

to

The Graduate School

in Partial Fulfillment of the Requirements

for the Degree of

Doctor of Philosophy

in

Mechanical Engineering

Stony Brook University

December 2014

Stony Brook University

The Graduate School

Martin Sauzade

We, the dissertation committee for the above candidate for the Doctor of Philosophy degree, hereby recommend acceptance of this dissertation.

Thomas Cubaud – Dissertation Advisor
Professor, Department of Mechanical Engineering

Jon Longtin – Chairperson of Defense
Professor, Department of Mechanical Engineering

Foluso Ladeinde, Member
Professor, Department of Mechanical Engineering

Eric Brouzes, Outside Member
Professor
Department of Biomedical Engineering, Stony Brook University

This dissertation is accepted by the Graduate School.

Charles Taber
Dean of the Graduate School

Abstract of the Dissertation

Motion of Bubbles in Confined Microgeometries: Flow Behavior and CO_2 Dissolution Regimes

by

Martin Sauzade

Doctor of Philosophy

in

Mechanical Engineering

Stony Brook University

2014

The motion and dissolution of bubbles in confined microgeometries is of pivotal importance for many natural and industrial flow processes such as microchemical systems and the development of models for unveiling the fundamentals of oil recovery in porous-like media. In this thesis, we experimentally study the formation, morphology, dynamics and mass transfer of bubbles flowing through a liquid in a microchannel with a particular emphasis on the behavior and dissolution of CO_2 micro-bubbles in high viscosity oils. A significant part of the thesis addresses the initial dynamical behavior of dissolving CO_2 monodisperse micro-bubbles in numerous solvents (water, silicone oils, alcohols, alkanes) over a range of flow rates and pressure conditions. The effective mass diffusion flux across the bubble interface is measured by tracking individual

bubbles and monitoring their shape as they shrink. The initial steady mass flux is characterized using a practical dissolution coefficient that is shown to depend on the fluids physicochemical properties. Our findings show the possibility to control and exploit the interplay between capillary and mass transfer phenomena in small-scale systems. We also tackle the generation of periodic trains of monodisperse bubbles at the hydrodynamic focusing section of a square microchannel, underlining the hydrodynamics resulting in the bubble breakup under various flow conditions. Finally, we investigate the flow of bubbles in complex microgeometries at large capillary numbers, highlighting the rich variety of flow morphology attainable.

à Alena

Acknowledgements

I would like to thank my advisor, Dr. Thomas Cubaud for his time, guidance, and encouragement throughout my Ph.D. studies. I would like to extend my sincerest thanks and appreciation to my dissertation defense committee members, Dr. Jon Longtin, Dr. Foluso Ladeinde, Dr. Eric Brouzes and Dr. Vera Gorfinkel for their time spent reviewing this work and their valuable comments.

I would also like to thank my mentors during my time as a Master's student in Paris and lab research assistant at UCSD, Dr. Olivier Doare and Dr. Eric Lauga, for their constant support and assistance throughout my studies and for encouraging me to pursue my interest in Fluid Mechanics.

I am indebted to fellow students I have worked with along the way, including but not limited to Samira, Bibin, Xiaoyi and Sara.

I acknowledge the research funding I received over the years from the National Science Foundation.

Finally, I am deeply grateful to my parents, Yannick and Didier for their encouragement, love and support.

Contents

Chapter 1

Introduction

1.1 Motivations

1.1.1 Microfluidics

The miniaturization of electronic systems to the micro scale in the late 1970's, driven by silicon technology, engendered the integrated circuit revolution and fundamentally transformed our society. The subsequent miniaturization of devices combining both electronic and mechanical components gave rise to a field known as MEMS (MicroEletro-Mechanical Systems) in the 1980's. As the technology developed, it appeared in chemical, biological and biomedical devices, many of which operate using a fluid flow. At this scale (10^{-6}m), fluids flow in an unfamiliar fashion, which had not been highly controllable until then. A new domain, microfluidics, surfaced to investigate the fundamental mechanisms governing the flow of fluids at the micro-scale and to explore its prospects.

Over the last twenty years, microfluidics has demonstrated its potential, allowing the integration of complex bio-chemical and control systems [1–4]. The early 1990's saw the development of microfluidic systems with usage in consumer products, (such as inkjet printing, liquid crystal displays) but also in chromatography [5], in cytometry [6] and in micro-chemistry [7]. Microfluidics has notably revolutionized the field of bio-analytical chemistry, allowing the

full-automation of complex processes using the concept of a Lab-on-a-Chip [8–11]. A Lab-on-a-Chip (LOC) device, also known as a micro-total-analytical system (microTAS), is a device that can integrate miniaturized laboratory functions (such as separation and analysis of components of a mixture) on a single microprocessor chip using extremely small fluid volumes on the order of nanoliters to picoliters. For instance, the area of DNA sequencing has been fundamentally disrupted with the emergence of microfluidic automated analysis, reducing drastically the cost and labor of genome sequencing [12–15].

The physics of the flow field at the microscale is of fundamental interest, as it allows researchers to explore phenomena that are difficult to control and monitor, or simply unattainable at the macro-scale. Comparably to the shift from classical mechanics to quantum mechanics when reaching atomic and sub-atomic scales, the physics of the fluid flow changes drastically at the microscale. The small length scale brings to prominence surface forces, allowing boundary effects to drive the flow (electrokinetic effects, acoustic streaming, ...) and the observation and production of complex interfacial phenomena.

1.1.2 Thesis aims and scope

Microscale multiphase flows involve the transport of two or more immiscible or partially miscible fluids in geometries with characteristic cross-sectional dimension varying from tens to hundreds of microns. The resulting flows display a rich phase behavior, which depends on the relative flow rates of the fluid phases involved, the interaction between gravitational, interfacial, inertial and viscous forces, as well as the wetting behavior of the confining environment.

Microfluidic multiphase flows take place in a wide array of systems, such as proteomics assays [16, 17], fuel-cells [18–20], and physiological flows in the respiratory system [21] (see also figure 1.1). Particularly, the motion of bubbles in confined microgeometries is of pivotal importance in many natural and industrial flow processes. In chemistry, such dispersed multiphase flow features large interfacial areas, rapid mixing and reduced mass transfer limitations, allowing microchemical systems to achieve improved performance and selec-

tivity compared to bench-scale systems (see reviews by Kashi et al. [22, 23]). Geophysical flows in porous media are experimentally modeled by injecting fluids in a microfluidic chip mimicking the features of the geologic medium. Such an experimental micro-model allows the examination and optimization of gas-assisted oil recovery as well as carbon sequestration [24–27]. All aforementioned processes depend on numerous parameters, such as viscosity, flow rates, pressures and diffusive behavior of gas-liquid systems.

Whether it be for unveiling the fundamentals of oil recovery or to screen potential biochemicals, microfluidic techniques have been copiously employed to study gas-liquid multiphase flow in a microchannel. The strengths of the microfluidic approach to study forced-convection mass transfer are multifold: (1) initial conditions are well controlled and reproducible, (2) a wide range of magnifications, times-scales, flow rates, and pressures are attainable using a robust microfluidic setup, (3) the large specific interfacial area of micro bubbles allows for enhancing mass exchange processes, (4) the relatively large pressure required to displace fluids in microchannels can be utilized to enhance gas solubility and mass exchange rates, and (5) segmented flows permit a recirculation motion in the liquid plugs, which facilitates the rapid mixing of dissolved species in the liquid.

Moreover, microfluidic devices provide useful platforms for examining the interaction between bubble dynamics and dissolution processes in an highly controllable manner. By manipulating the gas and liquid flow rates, monodisperse bubbles are created on a chip with a given dimension and spacing, therefore allowing the species concentration in the chip to be controlled.

The behavior of CO_2 micro bubbles is of particular importance, as it is involved in processes from advanced oil recovery [35, 36], CO_2 capture and storage (CCS) [37, 38], respiration [39] to material synthesis where supercritical CO_2 is used as a green solvent [40]. Studies of time-dependent bubbles at the microscale are relatively limited and the behavior of carbonated microflows has only recently been studied [41–45] .Numerous aspects of the flow remain unexplored or unsettled, such as the early behavior of dissolving bubbles, the

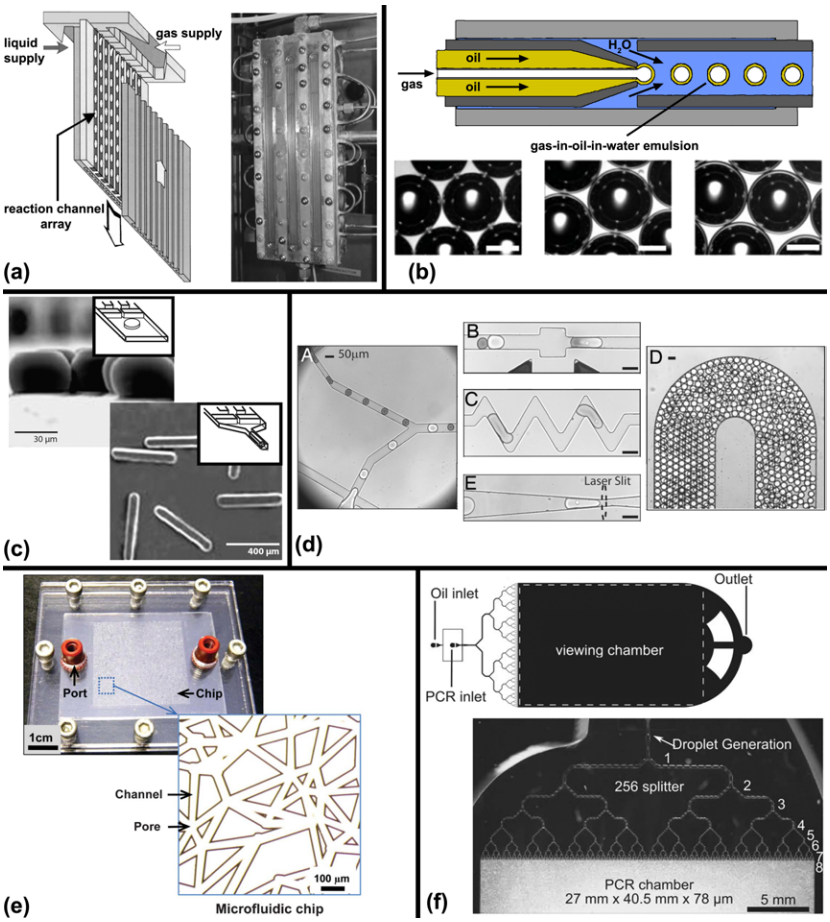

FIG. 1.1: Examples of microfluidic multiphase flows applications. (a)Schematic diagram of a micro bubble column and a photograph of the associated microreactor device. This device generates an highly dispersed flow to conduct direct fluorination [28]. (b) Sketch of the microfluidic capillary device for the generation of Gas/Oil/Water emulsions (pictured below) [29]. Such emulsions are used as ultrasound contrast agents or for the preparation of hollow particles [30]. (c) Continuous microfluidic synthesis of particles with nonspherical shapes using photopolymerization and continuous flow lithography [31]. (d) Droplet-based microfluidic technology that enables high-throughput screening of single cells. This integrated platform allows for the encapsulation of single cells and reagents in independent aqueous microdroplets dispersed in an immiscible carrier oil and enables the digital manipulation of these reactors at a very high-throughput [32] (e) The lab-on-a-chip based approach to the study of CO_2 injection and salt precipitation in saline aquifers [33]. (f) A droplet microfluidic platform integrating multiple high-throughput droplet processing schemes on the chip and is capable of generating over 1-million, monodisperse, 50 picolitre droplets in 2-7 minutes. This device then undergoes on-chip polymerase chain reaction (PCR) amplification and fluorescence detection [34].

impact of the viscosity on the flow behavior, or a unifying picture to describe the mechanisms underlying bubble generation.

In this thesis, we experimentally study the formation, morphology, dynamics and mass transfer of bubbles flowing through a liquid in a microchannel with a particular emphasis on the behavior and dissolution of CO_2 microbubbles in high-viscosity silicone oils.

A significant part of the thesis addresses the initial dynamical behavior of dissolving CO_2 monodisperse microbubbles in numerous solvents (water, silicone oils, alcohols, alkanes) over a range of flow rates and pressure conditions. The effective mass diffusion flux across the bubble interface is measured by tracking individual bubbles and monitoring their shape as they shrink. Sun et al. [41] showed that for short time scales after fluid initial contact, bubbles display a fast diffusive behavior associated with a linear decrease of their axial dimension. In this dissertation, we first tackle the morphology and hydrodynamic stability of dissolving bubbles at a long scale for the system CO_2-water before investigating in detail the aforementioned fast diffusive regime. This early fast diffusive mode coincides with the numerous observations of an initial fast dissolution of micro bubbles, during which most of the volume loss occurs. In this thesis, we report the first investigation on the early microfluidic dissolution of CO_2 bubbles in alcohols, alkanes and silicone oils. A simple model is built to characterize the initial steady mass flux using a practical dissolution coefficient that is shown to depend on the fluids' physicochemical properties. While microfluidic studies have shed light on the dissolution dynamics of carbon dioxide gas in low-viscosity solvents [41, 42, 45, 46], many technological fluids are highly viscous. In this case, bubbles are confined by a thick liquid film adjoining the solid walls and adopt a complex bullet shape depending on flow conditions [47]. Directly characterizing the combined effect of carbon dioxide absorption and diffusion processes in this situation would improve the modeling and practical use of high-viscosity carbonated microflows. We examine the early behavior of CO_2 micro bubbles in viscous silicone oils, highlighting the similarities and differences with the low-viscosity dissolution.

In this thesis, we also tackle the generation of periodic trains of monodisperse bubbles at the hydrodynamic focusing section of a square microchannel, underlining the hydrodynamics resulting in the bubble breakup under various flow conditions.

Finally, we investigate the flow of bubbles in complex microgeometries at large capillary numbers, highlighting the rich variety of flow morphology attainable.

1.2 Single phase flow in microchannels

When shrinking the characteristic length scale of a fluidic system to the microscale, the fundamental physics change drastically compared to our everyday experience [48, 49]. For instance, one may have observed the swimming strategies of microorganisms using a microscope. From spermatozoa to *Escherichia coli*, moving microorganisms employ sets of mechanisms for swimming that are entirely different from their larger counterparts [49]. But why is rotating a long flagella or whipping arrays of cilia a better swimming strategy compared to paddling? It is because at the microscale inertia plays a small role and viscous damping is paramount, which makes any attempt to move by imparting momentum to the fluid (e.g. paddling) inefficient. Since inertia provides the nonlinearity that is responsible for turbulences, micro flows are therefore almost always laminar and consequently deterministic, which offers great promises for product-oriented research.

The small dimensions that suppress inertial nonlinearity bring other physical phenomena, less familiar on our macroscale, to prominence. By understanding such microscale phenomena, and using well-designed microfluidics systems, one can leverage their importance and perform experiments not doable at the macroscale, allowing new uses and experimental paradigms to emerge.

The essential fluid physics of a system is dictated by a competition between various phenomena, which is captured by a series of dimensionless numbers

expressing their relative importance. These dimensionless numbers form a sort of parametered space for microfluidic physics.

1.2.1 The Reynolds number

An incompressible Newtonian fluid with density ρ and viscosity μ satisfies the Navier-Stokes equations (which represent the conservation of momentum) as well as the conservation of mass:

$$\rho\left(\frac{\partial \mathbf{u}}{\partial t} + \mathbf{u}\cdot\nabla\mathbf{u}\right) = -\nabla p + \mu\nabla^2\mathbf{u} + \mathbf{f}, \qquad \nabla\cdot\mathbf{u} = 0. \tag{1.1}$$

where $\mathbf{u}$ is the velocity field, p the pressure and $\mathbf{f}$ the body force(s) applied to the system.
Using a reference velocity U, a reference length L as well as the properties of the fluid (μ, ρ) one can obtain (the dimensionless variables are denoted by an asterisk):

$$\rho\left(\frac{U\partial\mathbf{u}^*}{L/U\partial t^*} + U^2\mathbf{u}^*\cdot\frac{\nabla^*}{L}\mathbf{u}^*\right) = -\frac{\mu U}{L}\frac{\nabla^*}{L}p^* + \mu U\frac{\nabla^{*2}}{L^2}\mathbf{u}^* + \mathbf{f}, \quad \nabla^*\cdot\mathbf{u}^* = 0. \tag{1.2}$$

Leading to:

$$\frac{\rho LU}{\mu}\left(\frac{\partial\mathbf{u}^*}{\partial t^*} + \mathbf{u}^*\cdot\nabla^*\mathbf{u}^*\right) = -\nabla^* p^* + \nabla^{*2}\mathbf{u}^* + \frac{L^2}{\mu U}\mathbf{f}, \quad \nabla^*\cdot\mathbf{u}^* = 0. \tag{1.3}$$

The non-dimensional ratio $\rho LU/\mu$ naturally appears in the equation and one can find that it is equivalent to the ratio between the typical inertial forces (the advection term $\rho\mathbf{u}\cdot\nabla\mathbf{u}$ scales as $\rho U^2/L$) over the typical viscous forces acting on a body (scaling as $\mu U/L^2$). This non-dimensional number is referred to as the Reynolds number and is given by:

$$\mathrm{Re} \equiv \rho UL/\mu. \tag{1.4}$$

When considering a flow within a microfluidic device, inertial forces are usually small compared to viscous forces. Considering for instance the flow of water

through a square micro channel of width $1 - 250$ μm at a typical velocity of 1μm/s -1 dm/s, the Reynolds numbers range between $O(10^{-6})$ and $O(10)$, i.e well within the laminar range.
We consequently assert that viscous forces typically overwhelm inertial forces, and equation 1.3 can be further simplified by neglecting the left side of the equation, which leads to the Stokes equation:

$$0 = -\nabla p + \mu \nabla^2 \mathbf{u} + \mathbf{f}, \qquad \nabla \cdot \mathbf{u} = 0. \tag{1.5}$$

A Stokes flow has no dependence on time other than through time-dependent boundary conditions. At a very low Reynolds number, inertia plays no role whatsoever, and a flow current state is entirely determined by the forces that are exerted on it at that moment, and not by any of its past states. Another property of Stokes flow is its time-reversibility which notably limits the mixing abilities of creeping flows (see section 1.3.2).
Note however that inertial effects can come into play in certain situations of high-speed flows (when the Reynolds number reaches $Re \sim 10^1 - 10^2$), for example when characterizing high throughput flows or highly transient phenomenon (e.g. bubble generation). When reaching that range of Reynolds number, inertial effects are significant, even though the flow is still laminar (i.e without turbulence).

Without the inertial nonlinearity, straightforward microfluidic systems have regular, deterministic flow. However, the microscale at which microfluidic systems operate also prompt the rise of other physical processes - such as capillary effects at free surfaces - whose nonlinearities give rise to a rich variety of microfluidic phenomena.

1.2.2 Fluid dynamics of the single phase flow

While micrometer-scale structures are small enough to ensure low-Re behavior, they are not so small that molecular graininess of fluids becomes important. Even for gases in microchannels, many billions of molecules occupy a

characteristic volume element of the flow in a microchannel; the fluid behaves like a continuum, and the Stokes equation gives an accurate description of the flow.

At low Re, the nonlinearities associated with the Navier-Stokes equation are absent. For a fully developed, uniaxial, steady, incompressible flow at low Re in the absence of body forces, Stokes equation 1.5 can be rewritten for a flow driven by a pressure gradient in the x direction:

$$0 = -\frac{dp}{dx} + \mu\Big(\frac{\partial^2 u}{\partial y^2} + \frac{\partial^2 u}{\partial z^2}\Big) \tag{1.6}$$

The coordinate system is defined figure 1.2, and u is the velocity field along the channel and p the pressure field. The boundary condition at the channel walls (solid interface) is $u_x = 0$ (no-slip boundary condition). A pressure gradient, dp/dx, generated by applying an overpressure at the inlet, along a channel produces a parabolic or Poiseuille flow profile in the channel. The velocity of the flow varies across the entire cross-sectional area of the channel.

In the long, narrow geometries of microchannels, flows are predominantly uniaxial: the entire fluid moves parallel to the local orientation of the walls. The significance of uniaxial laminar flow is that all transport of momentum, mass, and heat in the direction normal to the flow is left to molecular mechanisms: molecular viscosity, molecular diffusivity, and thermal conductivity.

A Poiseuille flow is characterized by a parabolic velocity profile over the cross section of the channel, with zero velocity at the walls and a maximum at the channel's center. The exact solution of a Poiseuille flow through a duct of square cross section of width w is given by [50]:

$$u(y,z) = \frac{4w^2}{\mu\pi^3}\Big(-\frac{dp}{dx}\Big)\sum_{i=1,3,5,\ldots}^{\infty}(-1)^{(i-1)/2}\Big[1-\frac{\cosh(i\pi z/w)}{\cosh(i\pi/2)}\Big]\times\frac{\cos(i\pi y/w)}{i^3} \tag{1.7}$$

The maximum velocity is attained at the center of the duct and:

$$u_{max} = 2.1u_a, \tag{1.8}$$

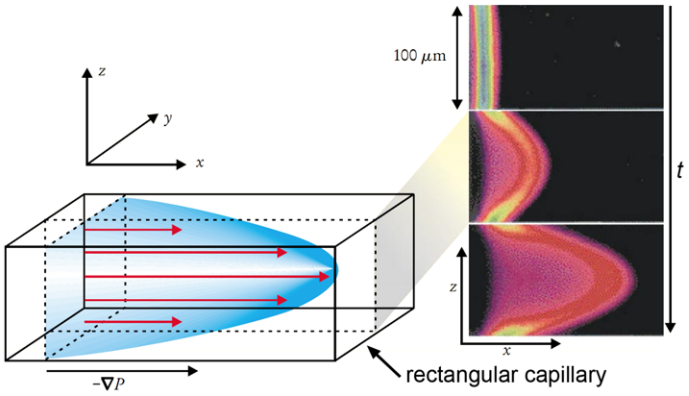

FIG. 1.2: Flow profiles in microchannels. A pressure gradient, dp/dx, along a channel generates a parabolic or Poiseuille flow profile in the channel. The velocity of the flow varies across the entire cross-sectional area of the channel. On the right is an experimental measurement of the distortion of a volume of fluid in a Poiseuille flow using fluorescent molecules [51]

where $u_a = Q/w^2$ is the average velocity and Q the volumetric flow rate. As depicted figure 1.2, the parabolic flow profile distorts a volume of fluid as it flows down the channel. When used to separate different molecules in a solution, such a flow spatially broadens the bands of distinct species.

1.3 Behavior of multiphase flows in microfluidic devices

The loss of the nonlinearities related to inertia (such as inertia associated-instabilities and turbulences) when attaining the microscale makes single phase flow in microchannel of little interest. However, the introduction of a second phase in the microgeometries introduces a wealth of behaviors and instabilities. As the dimension shrinks to the micro-metric scale, the relative importance of surface forces to volume forces increases, and surface tension effects and viscous forces become predominant compared to inertia and buoyancy forces.

In this section, we present some of the dimensionless numbers associated with multiphase flows as well as some of the important physical phenomena af-

fecting such flows at the microscale. We then discuss the different fluid phase distributions attainable and the mechanisms responsible for their establishment.

1.3.1 The Capillary number: a competition between viscous forces and interfacial tension

At the interface between immiscible fluids, interfacial tensions affect the dynamics of the free surface. While surface tension effects are typically weak at the macro scale, fluid flows at the microscale also differ from their macroscopic analogs because of their large surface-area-to-volume ratio. This leads to negligible gravity effects as well as significant surface tension forces.
Combined with the absence of inertia, the behavior of a multiphase flow in a microfluidic device is therefore governed for the most part by interfacial tension and viscous effects. The relative strength of the two is expressed by the Capillary number

$$\mathrm{Ca} \equiv \mu U/\gamma. \tag{1.9}$$

In the case of a liquid/gas flow, μ is the liquid viscosity acting in the system and γ the surface tension between the two phases. A low value of Ca indicates that the stresses due to interfacial tension are strong compared to viscous stresses. Currently, most of the research and applications use microfluidic systems with typical values of $\mathrm{Ca} \sim 10^{-2}$, i.e when interfacial forces dominate over viscous forces. Under such flow conditions, bubbles and droplets minimize their surface area by producing slugs with spherical ends in confined channels and coin-like shape in between parallel plates.

The surface tension between two media also causes a pressure jump at the interface; this pressure jump is given by Laplace's law $\Delta P = \gamma(1/R_1 + 1/R_2)$, where R_1 and R_2 are the two radii of curvature. For instance, the overpressure inside a drop of oil in equilibrium in water can be found by $\Delta P = P_o - P_w = 2\gamma/R$), where R is the radius of the droplet and P_o and P_w are the pressures in the water and oil phase respectively. However, this law is only valid at static or quasi-static state, greatly limiting its applications.

1.3.2 The Peclet number and the problem of mixing

The Peclet number, Pe, provides an indication of the relative importance of diffusion and convection, diffusion being caused by the random thermal motion of molecules within their surrounding environment (i.e Browninan motion) and convection being the mass transport resulting from a bulk fluid motion [52]. In a purely laminar flow, the absence of turbulent mixing, which normally chaotically stretch and fold fluid elements [53], increases dramatically the time scales for mixing. The Peclet number, relating convective to diffusive transport, is defined as

$$\mathrm{Pe} \equiv u_a h/D, \tag{1.10}$$

where u_a is the average velocity of the flow, h is a characteristic length of the system perpendicular to the direction of the flow and D is the diffusion coefficient of the particle or molecule of interest. The Peclet number in microfluidic systems is typically greater than 100, diffusive mixing is therefore slow in contrast to the axial velocity of the fluid along the channel. This can result in long mixing times of the order of minutes or more.

The Taylor-Aris dispersion provides a classic example of the role of convection in dispersing inhomogeneous flows [54, 55], as it tackles the transport and spreading of a solute pulse of material A introduced into a fluid B in steady laminar flow. The thin stripe of tracer A, placed into a parabolic Haggen-Poiseuille flow (see section 1.2.2), is stretched into a parabola before the molecular diffusion smears the parabolic stripe into a plug of material A. This example demonstrates a pattern that emerges when dealing with the dispersion of traces at low Reynolds number: tracer dispersion is initially dominated by convective stretching, and is then followed by diffusive homogenization.

Two basic principles induce mixing at the microscale. In active mixing, an exterior energy input is exploited. Possible energy sources include ultrasound and acoustic waves, bubble-induced vibrations (see figure 1.3(c)), electrokinetic instabilities, piezoelectric vibrating membranes, integrated microvalves/pumps and much more (see extensive review by Hessel et al [56]).

A second mean to induce mixing, known as passive mixing, exploits the flow energy (e.g. due to pumping action or hydrostatic potential) to rearrange the flow to intensify mixing. For instance, the folding and stretching of fluids in extremely narrow striations maintains large concentration gradients. Methods to obtain such flows include hydrodynamic focusing [57] and geometries imposing a striated flow distribution (see figure 1.3(a-b)). Other concepts have been successfully employed in a variety of micro mixers involving complex spatially varying geometries, or a series of periodically forced cross streams as depicted in figure 1.3(b). Other passive mixers include micro mixers based on droplet-based chaotic advection [58] or jets collisions[59]. Passive mixers have been utilized to probe the transient events which occur during rapid chemical/biological processes or to achieve optimum synthesizing results in chemical kinetic studies [60] and nano-material synthesis [61].

1.3.3 On the importance of the wetting properties in a microchannel

Solid surfaces are characterized by their roughness and wetting behavior, which is dependent on the angle θ observed when a liquid/vapor phase meets a solid surface. However, the situation is sometimes more complex and an absorbed film sometimes separates the gas phase from the wall (see figure 1.4). It is very difficult to distinguish between the situations experimentally, so it is common to introduce an apparent contact angle θ_{app} (see review by Ajaev and Homsy [47]). Here, we refer to the contact angle as θ_{app} or θ depending on the situation. The value of the gas-liquid-solid contact angle θ indicates the wetting behavior of the system. Liquids exhibiting a low small contact angle approaching zero are considered wetting and liquids with large contact angles are referred to as non-wetting.

The wetting properties of the system fluids-channel wall can dramatically alter the flow structure. In figure 1.5(c), Zhao et al. [64] have chemically modified the surface of the microchannel, creating hydrophilic and hydrophobic areas. Aqueous liquids introduced into these patterned channels are confined

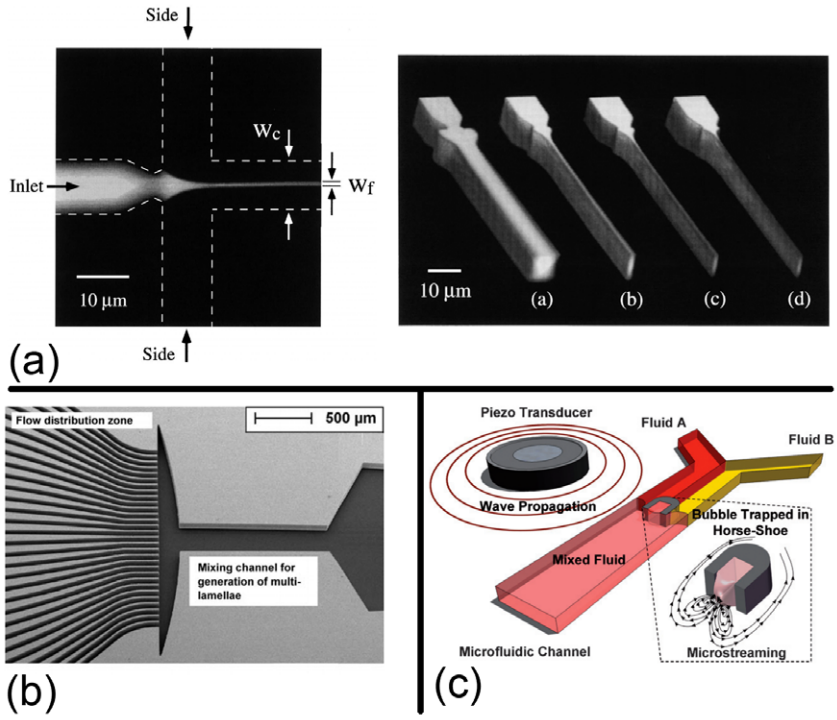

FIG. 1.3: (a) Passive mixing using hydrodynamic focusing by reducing the width of a central stream to a micro size to enhance diffusion. Mixing is visualised in a reaction-type experiment [57].(b) Another passive micromixer: slit-type interdigital micromixer made in glass for laboratory-scale applications [62].(c) Active mixing by acoustic microstreaming. An air bubble is trapped within the horseshoe structure and when activated by the piezo transducer generates a microstreaming around it [63].

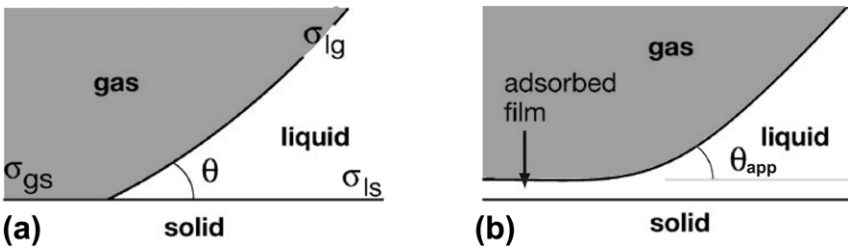

FIG. 1.4: Two different local configurations in the three-phase region: (a) all three phases intersect at a contact line with contact angle θ. (b) gas and solid remain separated by an adsorbed film [47]

to the hydrophilic pathways as long as the injection pressure is below a critical value. Additionally, micrometer- or submicrometer-scale roughness elements are routinely employed during the microfabrication process to alter wetting behavior of microfabricated surfaces either permanently or temporarily (see figure 1.5(a)). Electrowetting techniques (see review [65]), are probably the most popular means of driving microfluidic motion by controlling the wettability gradient. In this technology, a potential difference is applied between the dispersed phase and the solid dielectric surface, consequently altering the surface tension and the structure of the flow (see figure 1.5(b)). Thermal gradients manipulation, optowetting (wetting modification driven by light using photosensitive materials) and droplets are other methods commonly used to manipulate fluid lows by controlling the dynamics of surface tension.

1.3.4 Surfactants and micro-particles

Surfactants are referred to as tensio-active molecules because of their ability to modify the surface tension at the interface between two fluids. Surfactants are very often used in multiphase flow as they have a detergent and stabilizing effect.
A typical usage of surfactant is in the case of oil and water: depending on the structure of the surfactant, it can favor formation of oil drops in water or the reverse. The role of these molecules is to reduce the surface tension in the system, favoring the formation of a dispersed phase. Furthermore, surfactants are often used to avoid the coalescence of droplets in an emulsion or bubbles in a foam, as it can be seen figure 1.6(a).

Emulsions can also be stabilized by solid particles alone. These so-called Pickering emulsions exhibit very high energies of attachment when held at a liquid/liquid interface, consequently greatly limiting the emulsions tendency to coalesce. Moreover, colloidal particles absorbed on bubble surfaces (armored bubbles) can increase bubble and foam lifetime by several orders of magnitude (see figure 1.6(b)). Abkarian et al. [69] also showed that colloidal particles on the bubble surface can be used to control and arrest dissolution of bubbles,

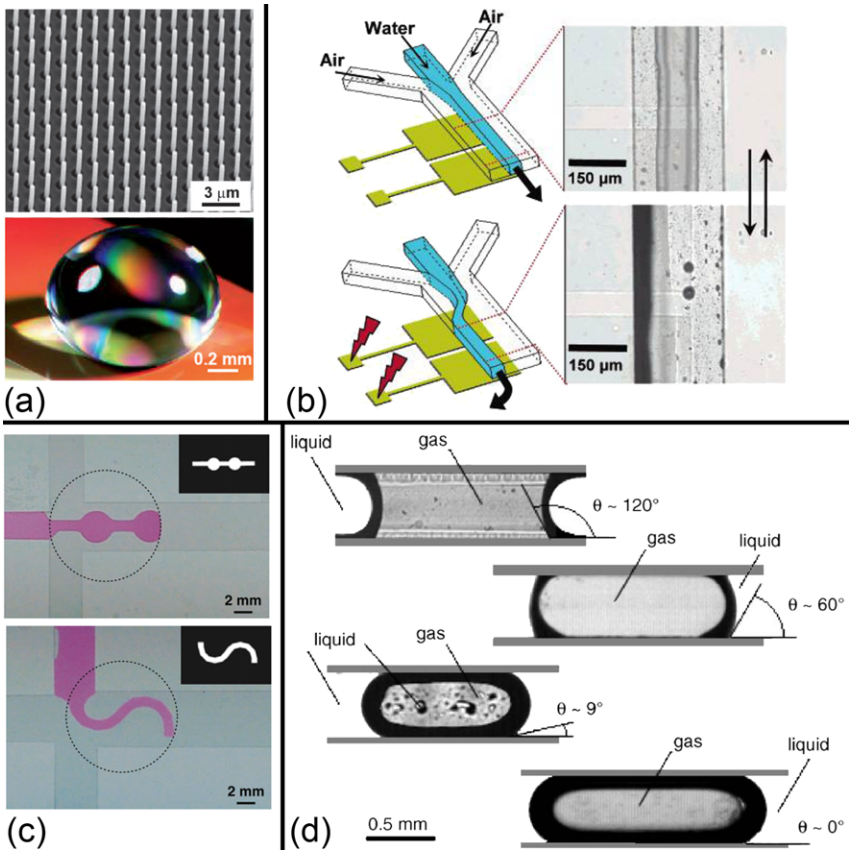

FIG. 1.5: (a) Superhydrophobic high-aspect-ratio silicon nanostructures and a demonstration of its hydrophobicity when a water droplet is deposited on top of the nanostructures [66].(b) Electrically induced switching of surface energy caused a focused high-speed water stream in the middle to swerve to flow along the sidewall [67]. (c) Microchannel altered by optowetting to fabricate hydrophilic and hydrophobic surface patterns inside microchannels. The aqueous liquids introduced into these patterned channels are confined to the hydrophilic pathways [64]. (d) Shapes of static bubble in square microchannel for different contact angles. From top to bottom: hydrophobic plug bubble, hydrophilic plug bubble, wedging bubble with contact line and lubricated bubble. The dark color represents a large liquid/gas curvature [68].

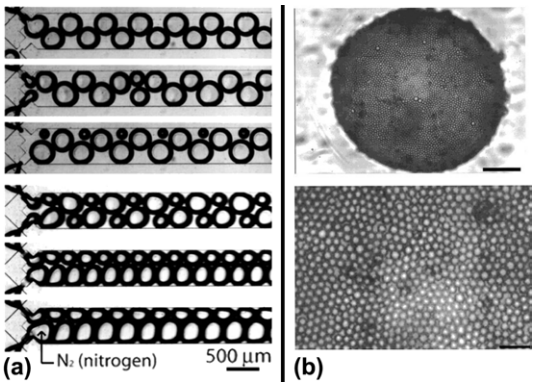

FIG. 1.6: (a) Optical micrographs of the self-assembled structures of nitrogen bubbles in an aqueous solution of surfactants [70]. The use of surfactant enables the formation of patterns unattainable using pure fluids (a small and a large bubble would coalesce due to the difference in Laplace pressure) (b) Optical microscope image of an emulsion drop coated with 3.2 μm diameter hydrophilic latex particles. Scale bar 50 μm and 15μm [71]. The colloidal particles coating greatly extends the droplet lifetime.

allowing the production of small and large bubbles depending on the particle concentration.

1.3.5 Instabilities

The flow of fluids within microstructures yield intriguing effects, most notably a variety of fluid instabilities difficult to reproduce or unattainable at the macro scale. Microfluidic systems enable us to generate such instabilities in a highly controllable manner. Periodic instabilities are notably responsible for the generation of uniform trains of bubbles/droplets at the junction of two co-flowing fluids. The wealth of behavior produced in microfluidics resides mainly in the development of these instabilities (see figure 1.7).
In addition to classic instabilities that occur between two fluids in bounded systems, such as viscous fingering (i.e Saffman-Taylor) and capillary (i.e Rayleight-Plateau) instabilities, micro devices have provided insight into elastic instabilities for non-Newtonian fluids at low Re [72], and inertial instabilities at moderate Re [44].

Capillary instability The formation of droplets or bubbles in microfluidic devices relates to the classical treatment of the capillary instability of sheared, cylindrical interfaces in unbounded flows by Plateau and Lord Rayleigh in the 1870s. In microfluidic devices, such instabilities allow the formation of monodisperse bubbles or drops in a flow focusing configuration shown in figure 1.7. In difference to the classical treatment of unbounded flows, fluid confinement between microchannel walls affects the breakup of a cylindrical liquid or gas core into droplets or bubbles. In many applications, a capillary instability is expected to produce liquid/liquid or gas/liquid segmented flows with uniform droplet or bubble sizes. Several attempts have focused on characterizing the rich dynamic behavior of segmented microflows that also includes very irregular flow behavior (see section 1.3.6).

Pressure-drop induced break-up At low capillary numbers, Garstecki [73] demonstrated that breakup of drops or bubbles at a microfluidic T-junction does not occur due to shear stress, but due to the pressure drop across the emerging bubble or drop (figure 1.7(b)).

1.3.6 Flow regimes

A number of flow regimes can occur depending on several factors, including the gas and liquid flow rates, the fluid properties (e.g., surface tension, viscosity, density), the wettability of the microchannel wall by the liquid (i.e., contact angle) as well as the channel size and geometry (including the channel cross section and inlet geometry). A number of experimental studies presented in the literature have been dedicated to the study of flow regimes in microchannels. An extensive review of these studies has been published by Shao et al. [76]. The description of the flow patterns is slightly subjective, as they rely on visual observations and depend on numerous experimental parameters.

Here, we describe the patterns observed and reported by Cubaud et al. [68, 77] in a square micro channel of width 525μm with the system air-water(see figure 1.8). Five predominant flow regimes are typically observed in partially-wetting square microchannels: bubbly, wedging, slug, annular and dry flow.

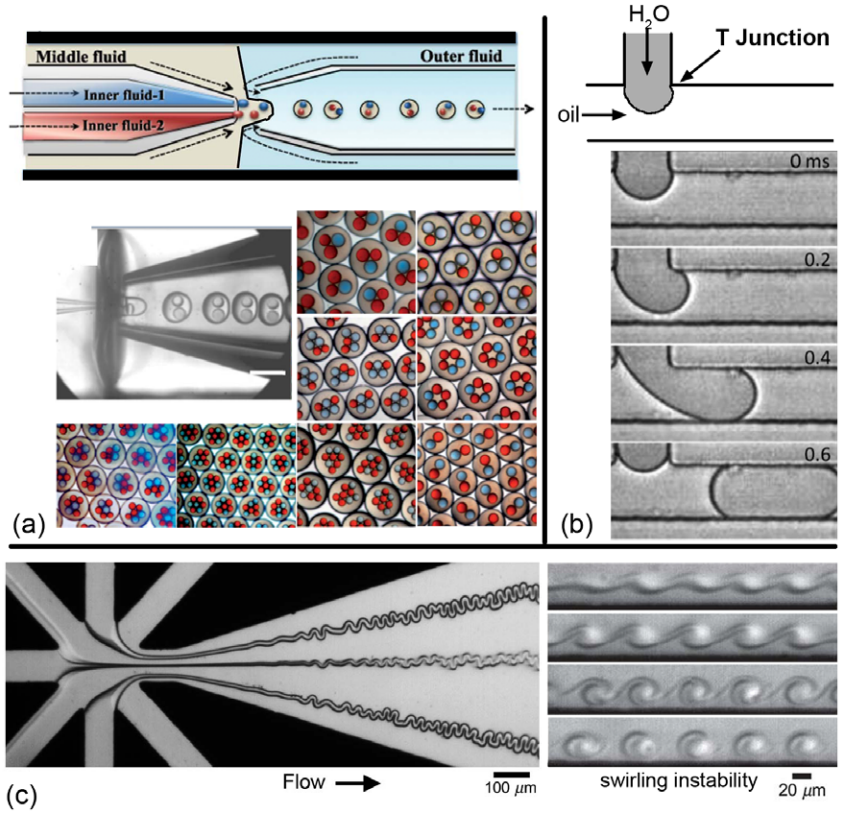

FIG. 1.7: (a) Schematic of a microfluidic capillary device for the preparation of multi-component double emulsions using a single-step emulsification. Optical microscopy images showing double emulsion generation and monodisperse double emulsions with two different inner drops [74]. (b)T-junction drop maker. Image sequence showing the formation of a water drop in oil using a T-junction [75]. (c) Images of folding instability that results when threads are subject to a compressive stress and deceleration along the flow direction in a diverging channel, and a viscous swirling instability that results when a thread is significantly sheared in a velocity gradient of the less viscous fluid, i.e., near the channelÕs side-walls [44]

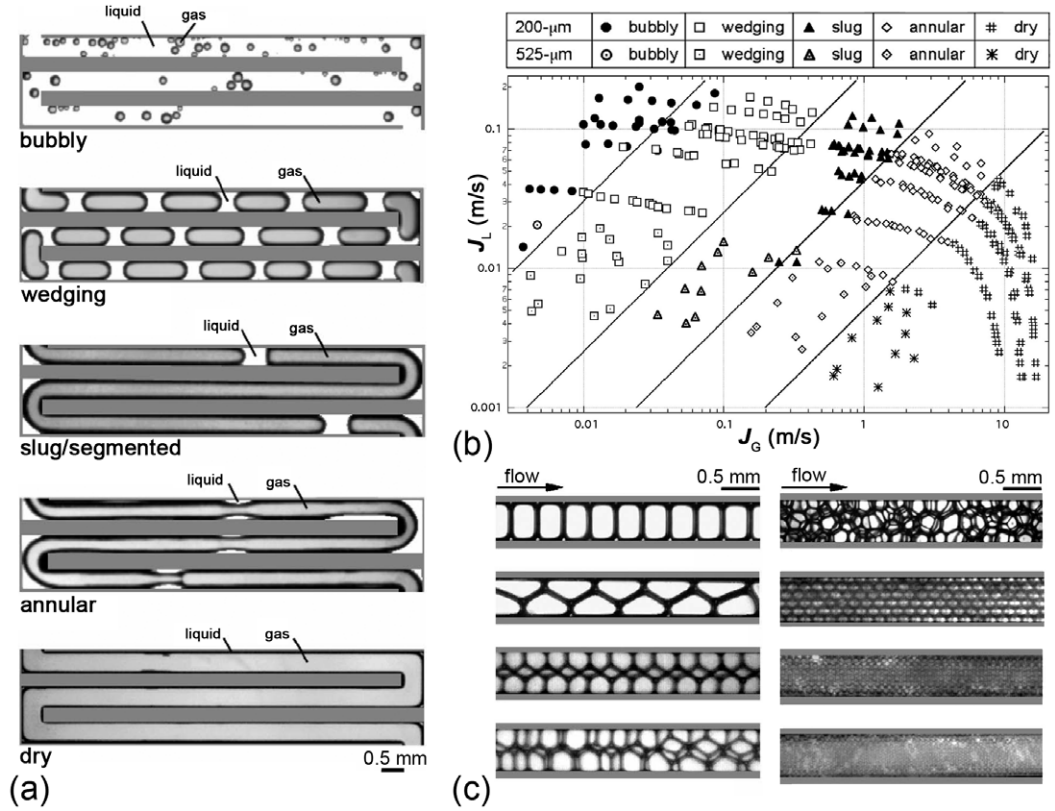

FIG. 1.8: (a) Pure water/air flow patterns in a square hydrophilic channels. (b) Associated flow pattern map for a microchannel height $h = 200\mu m$ and $h = 525\mu m$. (c) Water with surfactant/air flow patterns in hydrophilic channels [68, 77]

Bubbly flow : The flow is composed of discrete almost spherical gas bubbles. The size of the bubble is typically smaller than the channel width w, but coalescence in the microchannel results in larger bubbles and significant polydispersity.

Wedging flow : Bubbles are larger than w and considerably elongated due to the confinement. The bubbles are equally spaced and relatively mono disperse. Depending on the bubble size and velocity, gas may dry out the center of the channel creating contact lines. This regime is only attainable in partially wetting microchannels.

Slug flow : The slug flow consists of long elongated bubbles lubricated by a liquid film between the gas and the walls. The bubbles typically display a bullet-shaped front interface. The difference between the wedging and the slug flow is essentially due to the thickness of the liquid film between the bubbles and the center of the walls. For the wedging flow, the film is metastable and can break by nucleation of dewetting patches. For the slug flow, the film is stable and its thickness increases with the capillary number [77]. This regime is also known as the Taylor flow, segmented flow or intermittent flow and these terms are used interchangeably in this thesis.

Annular flow : The flow becomes annular when the bubble length is equal to the channel length. Gas continually flows in the center of the channel as a core, while the thin liquid film experiences wall shear.

Dry flow :When the void fraction is close to unity, liquid is confined to flow in the channel wedges. The gas dries the center of the channel wall.

The type of flow regime occurring in the microchannel strongly influences the performance of the operation being carried out in the reactor and it is therefore important to be able to predict the flow regime generated. Flow regime maps, similar to the one shown in figure 1.8(b), depict the regions in which a given flow pattern occurs as a function of operating conditions, typically the superficial gas and liquid velocities (see section 1.4.1). A number of flow regime maps for gas- liquid flow in microchannels have been proposed in the literature, but no single universal map, which is independent of fluid and microchannel characteristics, has successfully been derived for the prediction of gas-liquid flow regimes [78, 79].

Slug flow (alternatively referred to as segmented flow or Taylor flow) is the most scrutinized, as numerous industrial and practical applications rely on this regime. These include enhanced oil recovery, trickle-bed reactors, coating technology, polymer processing (see [80] and [81]).

1.4 Hydrodynamics of microscale segmented flows

Here, we report a few characteristics of the hydrodynamics of gas-liquid flows with an emphasis on rectangular microchannels. We first introduce convenient parameters when describing the hydrodynamics and mass exchange of a multiphase flow.

1.4.1 Introduction

A useful parameter to characterize a multiphase flow is the homogeneous liquid fraction α_L, defined as the ratio of the liquid flow rate over the total flow rate:

$$\alpha_L = \frac{Q_L}{Q_L + Q_G}. \tag{1.11}$$

Cubaud and Ho [77] notably showed that the liquid fraction is the key parameter to predict the structure of the flow, as the bubble length d is proportional to $1/\alpha_L$.

Another practical tool to describe a multiphase flow is the concept of superficial velocity. The superficial velocity of a phase is the hypothetical velocity calculated if the given phase were the only one flowing through the channel. By extension, the average superficial velocity is the sum of the superficial velocities and is equal to the total flow rate per unit of cross sectional area. If A_c is the cross sectional area of the channel, we define the liquid superficial velocity J_L, the gaseous superficial velocity J_G and the average superficial velocity J_{tot} as:

$$J_L = \frac{Q_L}{A_c},\ J_G = \frac{Q_G}{A_c},\ J_{tot} = J_L + J_G. \tag{1.12}$$

In the case of a square microchannel ($w = h$), we therefore have:

$$J_L = \frac{Q_L}{h^2},\ J_G = \frac{Q_G}{h^2}\ , J_{tot} = \frac{Q_L + Q_G}{h^2}. \tag{1.13}$$

These parameters are notably useful when compared with the bubble velocity

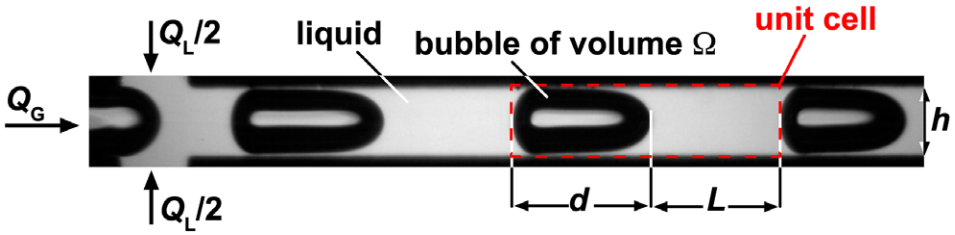

FIG. 1.9: Representation of the concept of unit cell in a periodic multiphase flow.

V_B.

The concept of unit cell is also useful when examining microscale multiphase flow. As the flow is periodic, is can be considered as a repetition of a unit cell consisting of a bubble plug and a liquid slug. The bubble has a length d, while the liquid slug has a length of L, and the unit cell has therefore a length $d + L$ (see figure 1.9).

A key parameter when discussing mass exchange between two phases is the interfacial area. The interfacial area A is the area of contact between the two phases. For low capillary segmented flows (surface tension effects are predominant), researchers often distinct the area of the two end caps (almost hemispherical at low speed) and the area of the bubble body, when the bubble is separated from the channel wall by a thin liquid film. The specific interfacial area a is defined as the interfacial area per volume of liquid in a unit cell:

$$a = \frac{A}{(L+d)h^2 - \Omega}, \tag{1.14}$$

where Ω is the bubble's volume.

1.4.2 Prologue

In 1924, Lewis and Whitman from M.I.T. first reported on one of the appealing characteristics of the flow of bubbles in a small capillary. In collaboration with H. G. Becker, they found that the most effective method for the absorption of gases by a liquid is a bubble rising through the liquid in a fairly narrow tube. Interestingly, they also point out the importance of the specific area (that is the interfacial area per volume of solvent) as well the bubble

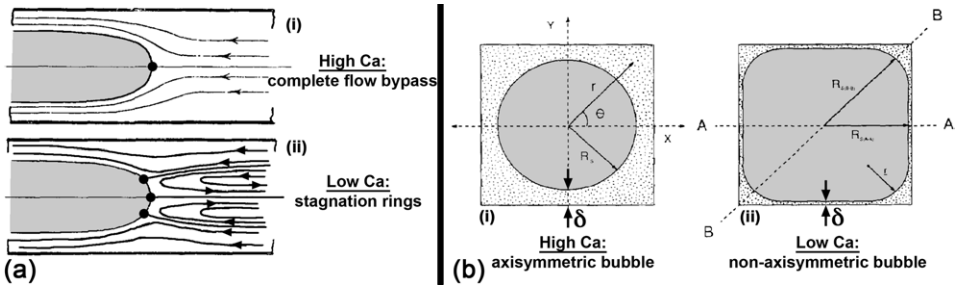

FIG. 1.10: (a)Sketch of the streamlines in the liquid slug for a long bubble flowing in a circular capillary, as postulated by Taylor [84]. The width of the liquid film δ is exaggerated in (ii). (b) View of the cross section of a bubble in a square channel for high and low capillary numbers.

shape on the mass exchange process [82]. In 1935, Fairbrother and Stubbs [83] were the first to pay attention to the motion of segmented bubbles in capillary channels. They were interested in determining the flow rate of the liquid in the capillary by measuring the speed of long bubbles convected through the capillary. They discovered that if the liquid wets the tube, the bubbles move faster than the average velocity of the liquid due to the deposition of a thin film of liquid on the walls of the tube, with a thickness depending on the capillary number Ca. The problem was rediscovered in 1961 by Taylor and Bretherton, both from the Cavendish Laboratory in Cambridge. Taylor [84] postulated the main features of the flow patterns, such as the presence of recirculation vortexes in the slug. Qualitative sketches of these streamline patterns are shown figure 1.10(a). At high capillary numbers, Taylor postulates the complete bypass of the flow while at low capillary numbers, he postulates the existence of stagnation rings around the bubble front. These features were all confirmed by later studies [85–87].

Bretherton [88] applied a lubrication analysis (developed to study the contact between bearings) to the Taylor flow and provided an expression for the pressure drop across a bubble as well as an expression for the thickness of the liquid film δ for very long bubble in a circular capillary. The theoretical results are validated by experimental data for capillary numbers $10^{-4} <\text{Ca}< 10^{-2}$ [79]. Consequently, the flow behavior of long bubbles in circular capillaries at low capillary numbers is relatively well understood.

Over the years, reliable correlations for the flow patterns of bubbles in circular capillaries were reported (see review by Kreutzer et al.[79]). While the motion of a single Taylor bubble inside circular capillaries has been studied extensively, both experimentally and theoretically, their square counterpart has been overshadowed. Thanks to novel microfabrication techniques researchers have started to conduct experimental studies in non-circular capillaries. Here, we summarize important results (bubble velocity, film thickness, velocity field...) obtained in square or rectangular microchannels.

1.4.3 Bubble shape - liquid film thickness

The motion of a Taylor bubble inside square capillaries differs from those inside circular ones because circular capillaries lack the corner flow of the liquid film. In circular capillaries, the bubble is axisymmetric, acting like a tight fit piston with a liquid film lubricating the bubbles. The flow inside square capillaries, however, is essentially three-dimensional and the bubble acts like a leaky piston. Kolb and Cerro [89, 90] studied experimentally and theoretically Taylor flow in square channels and identified two bubble shapes depending on the value of the capillary number. They applied the method employed by Taylor and Bretherton to find that when Ca$<$ 0.1, the bubble is not axisymmetric and flattens against the tube walls, leaving liquid regions in the corners separated by a thin flat film at the channel's side (figure 1.10(b)(ii). Even at low Ca, a finite film remains in the corner. This results from the corners being affected by viscous forces to a greater extent than regions near the walls. At higher Ca the bubble cross-sectional radius reaches an asymptotic value:

$$r_b^{lim} = 0.34h \tag{1.15}$$

Thulasidas [91] showed that the film surrounding the bubble offers minimum resistance to the flow and is always present, even if very thin. They identified more precisely than Kolb and Cerro [89] the transition between axysymmetric and non-axisymmetric at Ca $\approx$ 0.04. Hazel and Heil [92] computed the shape of bubbles in square capillaries using a finite-element free-surface formulation. Kreutzer et al. [79] compiled all data available and reported that while most

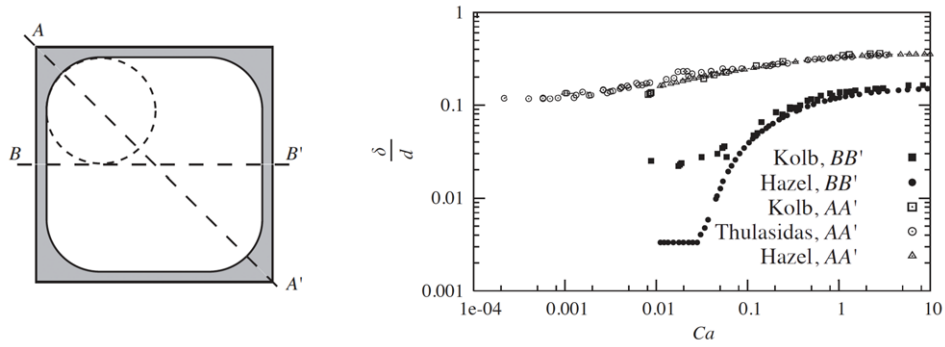

FIG. 1.11: Film thickness AA' and BB' versus Ca in square capillaries. Experimental data from [91] and [89], numerical data from [92] [79].

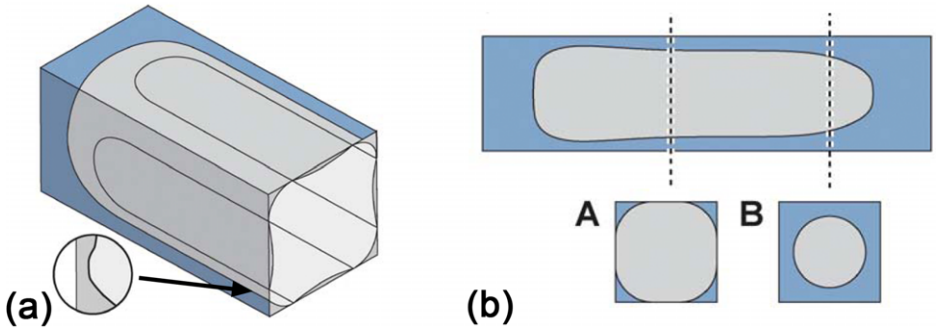

FIG. 1.12: Pressure-driven motion of bubbles in square channels. (a) The shape at small Ca showing the entrained films [93], half of the bubble is shown. (b) An illustration for the intermediate-Ca-model of Ratulowski and Chang [95] [47].

studies agree on the evolution of the thin film δ vs Ca, there is not such consensus for the thickness of the liquid film in the gutters (see figure 1.11).

Wong et al. [93, 94] reported that the bubble shape at low Ca is better illustrated by the sketch of figure 1.12(a), showing films of non-uniform thickness on the wall in the limit of low capillary numbers. They also showed that for a bubble of finite length, the film thickness is not constant (see 1.12(b)), as previously reported by Ratulowski and Chang [95].

In 2006, Taha et al. used a numerical simulation to investigate the shapes of bubbles at different values of Ca. At low Ca, the bubbles have spherical ends and tend to flatten out against the walls. With increasing Ca, the bubble ends lose their sphericity and a small indentation appears at the rear of the bubble.

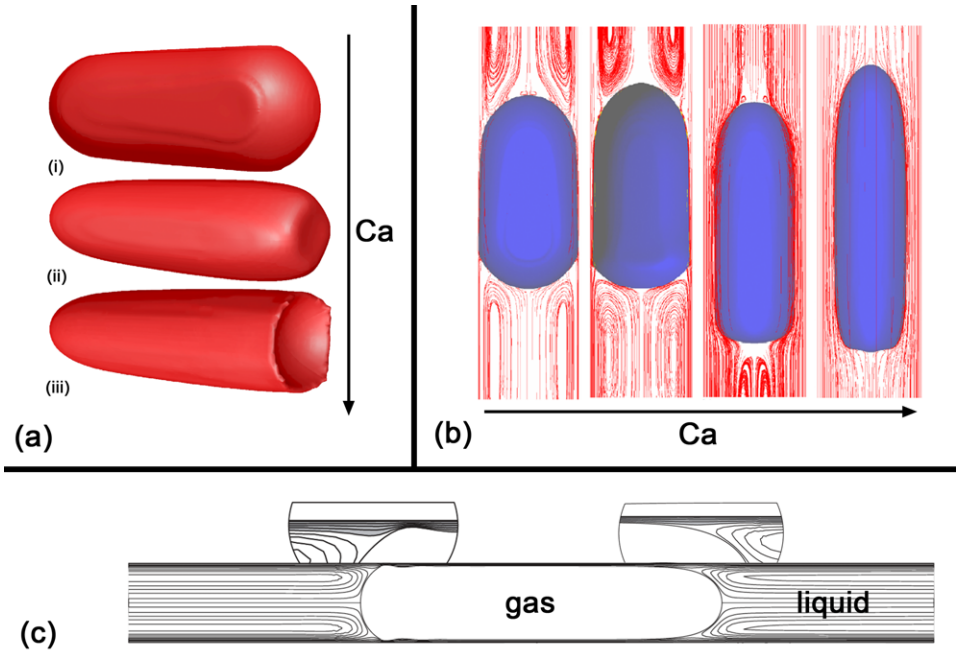

FIG. 1.13: Numerical simulations of slug flows in microchannels. (a) 3-D view of the bubble shape in a square microchannel (CFD simulation using the Volume Of Fluid (VOF) method) for (i) Ca = 0.009; (ii) Ca = 1.35; (iii) Ca = 3.04 [81].(b) Flow velocity field around a gas slug rising inside square capillary with a frame of reference moving with the bubble (CFD simulation) [81]. (c) Streamlines in the liquid phase. The film region is indicated in grey and the circulating region is indicated in white [101].

Moreover, the bubble becomes longer and cylindrical in shape; the liquid film is thicker and the nose is sharper, resembling those seen inside circular capillaries. Other researchers had made similar observations [96–100] but Taha et al. provide for the first time a 3D representation (see figure 1.13).

1.4.4 Bubble velocity

In Taylor flow, the bubbles travel only slightly faster than the sum of gas and liquid superficial velocity $V_B \approx J_{tot} = J_L + J_G$ at low capillary numbers. At high capillary numbers, when complete bypass occurs (all the liquid moves towards the bubble in its reference frame), the bubble velocity is equal to the maximum flow velocity, $V_B = 2.1 J_{tot}$. The transition between these two states

has been investigated by Liu et al. [102], and was found to depend only slightly on the microchannel cross section. Therefore, by combining experimental data in both circular and square capillaries, Liu et al. [102] obtain the following correlation:

$$\frac{V_B}{J_{tot}} = \frac{1}{1 - 0.61Ca^{0.33}}, \tag{1.16}$$

valid for $2 \times 10^{-4} <$Ca< 0.39.

1.4.5 Liquid plugs

As postulated by Taylor in 1961, numerous experimentalists have observed the existence of circulation loops in the liquid slugs of Taylor flows in microchannels. At low Ca, Zaloha et al. [103] reported that the recirculation velocity increases linearly with J_{tot} and is independent of the superficial velocity ratio J_G/J_L. On the other hand, they report that the recirculation time is proportional to L/J_{tot}. These results show that short liquid slugs at high J_{tot} provide the highest recirculation rates.

Thusalidas [91], as well as Kolb and Cerro [89] investigated the flow pattern within the liquid slug. They found that below Ca ≈ 0.5, the bubble is faster than the average, but slower than the maximum liquid velocity, which results in a stagnation ring on the bubble cap. On the other hand, above this threshold value of the capillary number, complete bypass occurs.

Streamlines patterns around the bubble rising inside a square capillary are presented in figure 1.13(b). The frame of reference is attached to the bubble and the wall moves down with a relative velocity equal to the bubble. At low Ca, one can clearly see the two vortexes ahead of the bubble. The vortices behind the bubble are nearly identical to those ahead of the bubble with the eye of the vortex easily identifiable. As the capillary number is increased the eye of the recirculating ring moves away from walls and shift towards the symmetry line. Augmentation in Ca results in a detachment of the back flow from the interface producing a new recirculating flow pattern where the recirculating rigs shrink toward the symmetry line. Finally, the flow recirculation vanishes producing a complete bypass when Ca is increased further. Apart from the stagnation point at the vertex of the meniscus and the above two stagnation

rings, there are two additional stagnation points located in the film region before the streamlines bow back. In this figure, the effect on the curvature of the streamlines near the bubble nose can be clearly seen. Figure 1.13(b) as well as figure 1.13(c) indicate that the stagnation points in the film region tend to recede toward the nose of the bubble as Ca increases.

1.5 Mass transfer in fluid systems

1.5.1 Equilibrium and solubility

The equilibrium of a gaseous phase in contact with a liquid phase can be modeled using Henry's law. For an easier understanding, let us consider a simple case that is closely related to the flows depicted later in this thesis: a pure gaseous CO_2 phase in contact with a liquid solution initially containing no CO_2. If the two phases have reached equilibrium and the liquid solution stays sufficiently dilute (less than 3 mol/mol according to [104, 105], the equilibrium concentration (solubility) in CO_2 within the liquid phase C_L^* [g.m^{-3}] is given by:

$$C_L^* = \frac{p_G}{k_H} = \frac{P_G}{k_H}, \tag{1.17}$$

where k_H is Henry's constant [atm.m^3.g^{-1}] for the system CO_2/solution and p_G [atm] is the partial pressure of CO_2 in the gas phase (i.e the gaseous pressure P_G since we consider a pure CO_2gas here). Thus, if left in contact for a long time with an infinite reservoir of gaseous CO_2 at a pressure P_G, the solution will ultimately reach a concentration in CO_2 equal to C_L^*. One can note that a larger pressure P_G results in an higher concentration while a larger Henry's constant has the opposite effect.

Additionally, to the sufficiently dilute solution limitation, Henry's law has to be used with great care when the solute reacts chemically with the solvent. Moreover, Henry's constants are technically a coefficients, as they vary with the system temperature [105] (the Henry's constant typically increases with temperature) and pressure. For pressure below 10atm, and approximately constant temperatures, we can however consider k_H constant.

1.5.2 Mass transfer at an interface

In the following we refer to the mass flux J_{mass} [g.m^{-2}.s^{-1}] as the mass of species exchanged from domain 1 to domain 2 per unit area per unit time (assuming no density variation):

$$J_{mass} \equiv \frac{1}{A}\frac{d(m)}{dt} \equiv \rho\frac{1}{A}\frac{d(\Omega)}{dt} \tag{1.18}$$

Here A [m^2] is the area between the two domains. m and Ω are respectively the instantaneous mass and volume of transported species in phase domain 2.

Here, we are interested in the transfer of mass from some interface into a well-mixed solution. We expect the amount transferred to be proportional to the concentration difference and the interfacial area. The mass transfer coefficient k [m.s^{-1}] is defined as the proportionality constant between the flux and the concentration difference:

$$J_{mass} = k(C_i - C_b) \tag{1.19}$$

The flux J_{mass} includes both diffusion and convection. The concentration C_i is at the interface, but in the same fluid as the bulk concentration C_b. When the fluid is a gas, partial pressures are better suited to describe the problem than concentrations.
The situation when the concentration at the interface is at equilibrium with the concentration across the interface in a second, adjacent fluid phase, is described in section 1.5.3.

Here, we present common models used to depict mass transfer from an interface into one bulk phase. Again, one should note that we are interested here in only one fluid: it is the difference in concentration from the interface to the bulk phase that drives the flux of species. Consequently, the models described below are displayed for $x \geq 0$ figure 1.14.

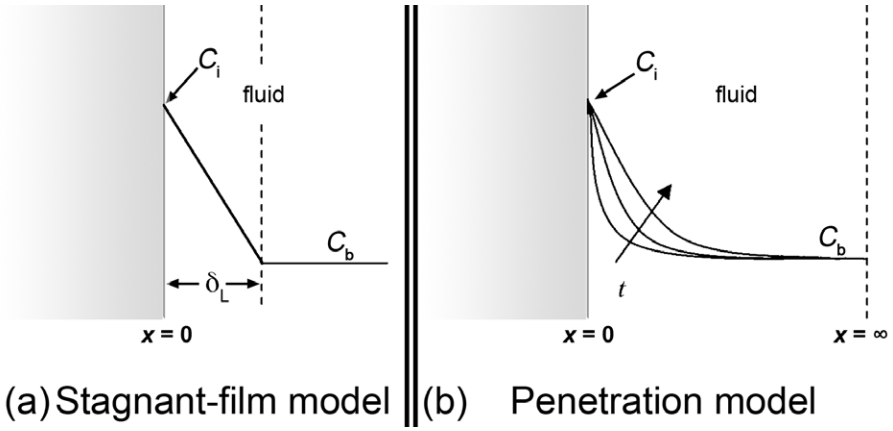

FIG. 1.14: Schematic representation of concentration profiles in a fluid for (a) the stagnant film model and (b) the film penetration model.

Stagnant-film model

This model was developed by Nernst [106] who postulated that near the interface exists a stagnant film. The mass transfer occurs only through this stagnant film within which the transport of species is governed by molecular diffusion (see figure 1.14(a) for $x \geq 0$). Moreover, there is a thermodynamic equilibrium between the interfacial phase concentrations, thus the interface itself does not hinder the mass transfer. Furthermore, there is no accumulation of diffusing species within the film. The concentration profile within the film is therefore linear and Fick's law describes the flux through the film:

$$\mathbf{J_{mass}} = -D\nabla C, \tag{1.20}$$

where J_{mass} is the mass flux of the diffusant, D [$m^2.s^{-1}$] is the species diffusion coefficient in the solvent and C is its concentration. If the thickness of the stagnant film is given by δ_{film}, the gradient can be approximated by

$$|\nabla C| \approx \frac{C_b - C_i}{\delta_{film}}, \tag{1.21}$$

where C_b and C_i are concentrations in the fluid bulk and at the interface, respectively. We therefore get:

$$J_{mass} = \frac{D}{\delta_{film}}(C_i - C_b) \tag{1.22}$$

Penetration and surface renewal models

More realistic models of the process have been proposed by Higbie in 1935 (penetration model) [107] and by Danckwerts in 1951 (surface renewal model) [108]. In both these models, the stagnant film is disrupted by fluid packets (eddies) from the fluid bulk. While at the interface, these eddies attempt to equilibrate with the gaseous phase under non-steady state conditions (see figure 1.14(b) for $x \geq 0$). Assuming that advection within the eddies can be neglected and the D is constant, the concentration profile in each eddy is determined by Fick's second law:

$$\frac{\partial C}{\partial t} = D\nabla^2 C. \tag{1.23}$$

In the penetration model, it is assumed that the eddy does not remain at the interface long enough to affect the concentration at the bottom of the eddy, and by solving equation 1.23 with such boundary conditions, one can find that the average flux at the interface over the time the eddy spends on the surface yields the following relationship:

$$J_{mass} = 2\sqrt{\frac{D}{\pi\tau_e}}(C_i - C_b). \tag{1.24}$$

Here τ_e is the average time that a fluid particle spends at the interface.
The surface-renewal theory is an extension of the previous theory that allows eddies of fluid to be exposed at the surface for varying lengths of time. On the assumption that the change of a surface element being replaced is independent of its age, one can get:

$$J_{mass} = \sqrt{Ds}(C_i - C_b), \tag{1.25}$$

where s is the surface renewal rate.

Mass transfer coefficients

In the case of the stagnant-film model, penetration model and surface renewal model, we respectively get:

$$k = \frac{D}{\delta_{film}}, \quad k = 2\sqrt{\frac{D}{\pi \tau_e}} \quad \text{and} \quad k = \sqrt{Ds} \tag{1.26}$$

Both the models by Higbie and Danckwerts predict that k is proportional to $D^{1/2}$ whereas the Nernst film model predicts that k is proportional to D. Typical observations report that none of the models accurately describe the dynamics of the mass transfer, but they are still useful to obtain an approximate result. Experimentally, k is found to be proportional to something between $D^{0.5}$ and D^1.

1.5.3 Mass transfer at a fluid-fluid interface

If two fluids are not in equilibrium (e.g. the species concentration do not follow Henry's law in the case of a gas/liquid system), there will be a transfer of mass across the interface until equilibrium is reached.

The flux equation

One can describe the mass transfer across an interface from one bulk phase into another different one by:

$$J_{mass} = K\Delta C, \tag{1.27}$$

J_mass is solute mass flux relative to the interface and K is called an overall mass transfer coefficient. To better understand what is an appropriate expression for the concentration difference ΔC, we consider the following example adapted from [109]

> Imagine that a benzene solution of bromine is placed on top of water containing the same concentration of bromine. After a while,

> we find that the initially equal concentrations have changed, that the bromine concentration in benzene is much higher than that in water. This is because the bromine is more soluble in benzene, so that its concentration in the final solution is higher.

This suggests that we should not use the concentration in benzene minus the concentration in water; it is initially zero, and yet there is a flux. Instead, we can use the concentration actually in benzene minus the concentration that would be in benzene in equilibrium with the actual concentration in water. Symbolically, we can write

$$J_{mass} = K(C_{benzene} - C^*_{water}), \tag{1.28}$$

where $C_{benzene}$ is the bromine concentration in benzene and C^*_{water} is the bromine concentration the benzene would have if it was at equilibrium with the actual concentration in water. Note that this does predict a zero flux at equilibrium.

The overal mass transfer coefficient

Let us consider the example of the gas-liquid interface in figure 1.15. In this example, a solute vapor is diffusing from the gas on the left into the liquid on the right. Because the solute concentration changes both in gas and in the liquid, the solute's flux must depend on a mass transfer coefficient in each phase.
The flux in the gas is given by (opposite of equation 1.19 since the solute is exiting this phase and using partial pressures):

$$J_{mass} = k_G(p_{b,G} - p_{i,G}), \tag{1.29}$$

where k_G is the gas mass transfer coefficient and $p_{b,G}$ and $p_{i,G}$ the solute partial pressure in the gas bulk and at the gas interface.
Likewise, in the liquid phase, we get:

$$J_{mass} = k_L(C_{i,L} - C_{b,L}), \tag{1.30}$$

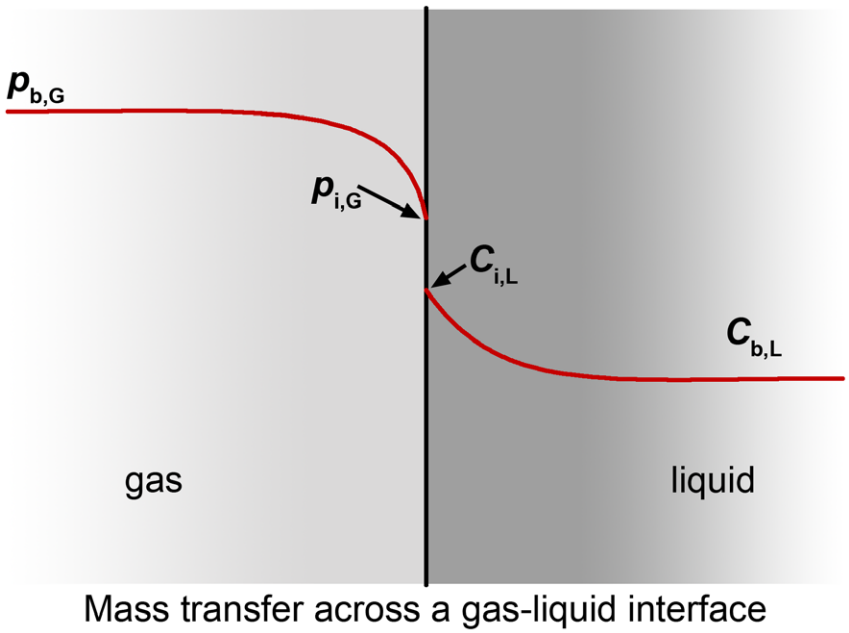

FIG. 1.15: Schematic representation of concentration profiles in gas-liquid system where both phases impact the mass transfer.

with k_L [m.s^{-1}] being the liquid mass transfer coefficient and $C_{b,L}$ and $C_{i,L}$ the solute concentration in the liquid bulk and at the liquid interface.
Because the interfacial region is thin, the flux across it will be in steady state, and the flux in the gas will equal that in the liquid.
In almost all cases, equilibrium exists across the interface, and we have using Henry's law 1.17:

$$p_{i,G} = C_{i,L} k_H \tag{1.31}$$

where k_H is the Henry's constant associated with the system.Combining equation 1.29 through 1.31, we can find the interfacial concentrations

$$C_{i,L} = \frac{p_{i,G}}{k_H} = \frac{k_G p_{b,G} + k_L C_{b,L}}{k_G k_H + k_L} \tag{1.32}$$

and the flux

$$J_{mass} = \frac{1}{1/k_G + k_H/k_L}(p_{b,G} - k_H C_{b,L}). \tag{1.33}$$

This result is often compared to an electric circuit containing two resistances in series. The flux corresponds to the current, and the concentration difference $(p_{b,G} - k_H C_{b,L})$ corresponds to the voltage. The resistance is then $\frac{1}{1/k_G + k_H/k_L}$, which is a sum of two resistances in series.
Following equation 1.27, one can write:

$$J_{mass} = K_L(C_L^* - C_{b,L}), \tag{1.34}$$

where K_L is the overall liquid-side mass transfer coefficient and C_L^* is the hypothetical liquid concentration that would be in equilibrium with the bulk gas, i.e.

$$C^* = \frac{p_{b,G}}{k_H}. \tag{1.35}$$

Thus we get the following expression for the overall liquid-side mass transfer coefficient:

$$K_L = \frac{1}{1/k_L + 1/k_G k_H}. \tag{1.36}$$

Following the same procedure, we can get the overall gas-side mass transfer coefficient K_G:

$$K_G = \frac{1}{1/k_G + k_H/k_L}. \tag{1.37}$$

Typically, the gaseous resistance is much smaller than the liquid resistance [110], leading to $k_G \gg k_L$. Considering such typical values, Sobieszuk [111] showed that we can neglect the gaseous resistance to mass transfer if $k_H > 10^{-6}$m^3.atm.mol^{-1}. Thus, the gaseous resistance to mass transfer can not be neglected for highly soluble solutes, such as the systems ammonia/water and chlorine/water. In this this thesis, the solutes (CO_2, N_2, O_2) are moderately soluble in the liquids involved (Henry's constant from 10^{-4} to 10^{-3} m^3.atm.mol^{-1}). This allows us to neglect the gas side resistance compared to the liquid side resistance:

$$K_L = k_L. \tag{1.38}$$

Moreover, when investigating the transfer of a pure gaseous phase into a liquid phase, only the liquid phase resistance needs to be taken into account as the gas resistance is null. The transfer of a species from a pure gaseous phase to

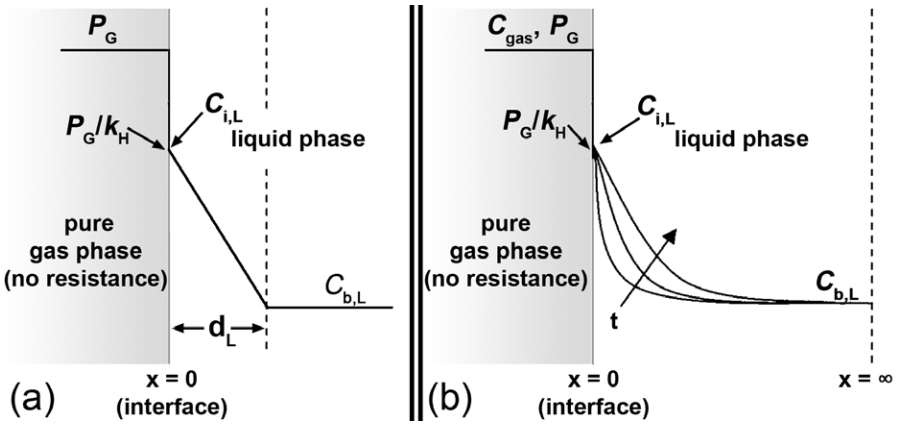

FIG. 1.16: Schematic representation of concentration profiles for the transfer of solute from a pure gaseous phase to a liquid phase. The stagnant-film model (a) and the penetration model (b) applied to the liquid phase.

a liquid phase is displayed in figure 1.16 when considering either the stagnant film model or the penetration model for the liquid phase.

1.6 Mass exchange in microscopic segmented flows

In addition to the fact that the segmented flow regime (other denomination of the slug or Taylor flow regime) is obtainable for a large range of gas and liquid flow rates, it presents several characteristics that enhance mass exchange processes: (1) a high gas-liquid interfacial area, i.e more surface to exchange species per unit of volume compared to conventional setups, (2) the large pressure required to drive liquids in microgeometries enhances the concentration gradient (3) the recirculation motion within the liquid plugs allows for a rapid homogenization of the diffusants. Here, we review some of the works that have provided a better understanding of the mass exchange within a microchannel.

1.6.1 Mass transfer in Taylor flow

An important advantage of microreactors for gas-liquid reactions is the significant intensification of the mass transfer processes. For illustration, a

Type of contractor	$k_L \times 10^5$ (m/s)	a (m^2/m^3)	$k_L a \times 10^2$ (s^{-1})
Bubble columns [112]	10-40	50-600	0.5-2.4
Couette-Taylor flow reactor [113]	9-20	200-1,200	3-21
Packed columns/beds [112]	4-60	10-1,700	0.04-102
Spray column [114]	12-19	75-170	1.5-2.2
Static mixers [115]	100-450	100-1,000	10-250
Stirred tank [114]	0.3-80	100-2,000	3-40
Tube reactors [112]	10-100	50-700	0.5-70
Gas-liquid microchannel [116]	40-160	3,400-9,000	30-2,100

Table 1.1: Comparison of micro structured reactors performance with conventional contractors for gas-liquid mass transfer with a being the specific interfacial area and k_L the liquid side mass transfer coefficient [23, 117]

comparison of the characteristic values governing gas-liquid mass transfer in a variety of conventional equipment and microreactors is given in table 1.1. The values in this table indicate that the volumetric mass transfer coefficient, $k_L a$, is 10^1 to 10^2 times greater in microreactors compared with that in conventional process equipment.

However, it is interesting to note that, as pointed out by Sobieszuk et al. [78], this intensification of mass transfer is principally due to a huge increase in the specific interfacial area in microstructured devices. The mass transfer coefficient itself is of the same order of magnitude as that obtained in static mixers and tubular reactors.

Using the definition of the liquid mass transfer coefficient from equation 1.34, one can write:

$$\frac{dC_L}{dt} = k_L a \Delta C = k_L a (C_L^* - C_L), \tag{1.39}$$

where a is the specific interfacial area, $a = A/\Omega_L$, with A being the interfacial area and Ω_L the volume of reactor.

Upon integration of the above equation from initial time ($t = 0$) to residence time ($t = \tau$) and concentration from inlet (C_L^{in}) to outlet (C_L^{out}), the overall volumetric mass transfer coefficient $k_L a$ becomes:

$$k_L a = \frac{1}{\tau} \ln \Big(\frac{C_L^* - C_L^{in}}{C_L^* - C_L^{out}} \Big) \tag{1.40}$$

Regime and system	Conditions and definition	Global volumetric mass transfer coefficient
Irandoust et al. (1992) • Slug (Taylor) flow–vertical reactor • Absorption of oxygen from air into water, ethanol and ethylene glycol	d_t=1.5, 2 mm L=0.6 m u=0.092–0.56 m/s	k_La=0.01–0.29 s^{-1} $k_La = 4\frac{\delta(d_H-\delta)uy_m + D_m Sh_L d_b}{d_t^2 L_{UC}}$ $y_m = \frac{C_m - C_2^{in}}{C_2^* - C_2^{in}}$
Berčič and Pintar (1997) • Slug (Taylor) flow–vertical reactor • Non-reacting system: methane–water	d_t = 1.5,2.5,3.1 mm L = 1.12 m u = 0.02–0.43 m/s k_La: Eq. (6)	k_La=0.005–0.115 s^{-1} $k_La = \frac{0.111(u_L+u_G)^{1.19}}{((1-\varphi_G)L_{UC})^{0.57}}$
van Baten and Krishna (2004) • Slug flow–vertical reactor • Non-reacting system Air–water	d_t = 1,2,3 mm L = 0.2–1.4 m u = 0.22–0.43 m/s k_La: Eq. (6)	k_La=0.08–0.47 s^{-1} $k_La = 4.1\sqrt{\frac{D_m u_G}{L_{UC}}}\frac{1}{d_t}$
Yue et al. (2007) • Slug flow, slug-annular, churn flow • Reacting system CO_2/buffer solution of 0.3 M $NaHCO_3$, 0.3 M Na_2CO_3, NaOH	d_H = 667 μm u_G = 0–2 m/s u_L = 0.09–1 m/s $k_La = \frac{u_L}{L}\ln\left(\frac{C_2^* - C_2^{in}}{C_2^* - C_2^{out}}\right)$	k_La=0.3–21 s^{-1} Slug flow (Physical absorption): $Sh_L a d_H = 0.084 Re_G^{0.213} Re_L^{0.937} Sc_L^{0.5}$ $Sh_L = \frac{k_L d}{D_m}; Re_i = \frac{\rho_i u_i d}{\mu_i}; Sc_L = \frac{\mu_L}{\rho_L D_m}; i = G$ or L

FIG. 1.17: Literature on gas-liquid mass transfer in Taylor flow [23]

This equation is the most commonly used to evaluate the value of the overall mass transfer coefficient.

A section of the literature review is listed on table 1.17. Most of the previous studies tackled the mass transfer in Taylor flow in circular capillaries. Applying these results to rectangular channels necessarily involves a high degree of uncertainty as the film thickness along the perimeter cannot be expected to be uniform (thicker at the edges). However, it is important to review the works done with circular capillaries, as they can help building models for square capillaries.

In 1997, Bercic and Pintar [118] proposed a correlation for the estimation of the mass transfer coefficient in a circular capillary. Their correlated k_La is a function of the slug length, but hardly of the bubble length. This result was surprising, as Higbie [107] had demonstrated that the liquid contact time was a function of the bubble length. This behavior can be explained by assuming that the lubrication film near the wall is completely saturated each time the bubble passes by. Then, a longer bubble does not improve mass transfer

and the mass transfer becomes independent of the bubble length. Moreover, the correlation by Bercic and Pintar showed no impact of channel diameter, and the specific interfacial area associated with the transfer from the caps is independent of channel diameter. Therefore, Bercic and Pintar suggest that transfer from the caps is important and that the liquid film surrounding the bubble is saturated.

We now consider the more fundamental approach to describe mass transfer from Taylor bubbles in circular capillaries developed by van Baten and Krishna [119]. Their model considers two contributions to mass transfer: (1) the caps (assumed to be hemispherical) at either end of the bubble and (2)the liquid film surrounding the bubble. They put forward the following relationship for the overall volumetric mass transfer coefficient: $k_L a = k_{L,cap} a_{cap} + k_{L,film} a_{film}$. They estimate the mass transfer coefficients $k_{L,cap}$ and $k_{L,film}$ by using the Higbie penetration mass transfer model (see equation 1.24) combined with a simple model for liquid element average contact time with the bubble. The authors assume short contact time between the bubble and the stagnant liquid film, consequently considering the impact of the film on the dissolution process. Van Baten and Krishna [119] obtained excellent agreement between their model predictions and their CFD simulations of mass transfer from Taylor bubbles in circular capillaries. However, two assumptions greatly restrict their results: (1) the idealized geometry, with a bubble consisting of a cylindrical body and hemispherical caps and (2) the free slip condition assumed at the gas liquid interface.

Yue et al. [116] proposed a dimensionless empirical correlation for the dissolution in rectangular microchannel without comparing their data to any available model. In 2009, Yue et al. [117] used a square microchannel and compared the model by van Baten and Krishna to their experimental data. They found that van Baten and Krishna model yields higher $k_L a$ values compared to their measurements. They ascribed this to poor mixing between the stagnant liquid film and the liquid slug, which leads to a non-homogeneous concentration within the liquid phase.

Roudet et al. [120] compared their data obtained in a rectangular microchannel and showed that none of the model available yields satisfactory results. They ascribed such discrepancies to an inadequate description of the mass transfer mechanisms through bubble surface in contact with liquid film.

This quick overview of the literature on the mass transfer performance of gas-liquid segmented flow in microchannels demonstrates the poor understanding of the dissolution process at the microscale. Some models were produced, but none of them gives satisfactory results when compared to experiments. Researchers have also presented empirical correlations, but they all give unsatisfactory results when compared to other works. Finally, disparate results demonstrate and unsatisfactory understanding of the processes, as some suggest the importance of the dissolution through the caps, while others emphasize the dominant contribution of the thin liquid film on the dissolution process.

Chapter 2

Experimental methods for visualizing two-phase flow in a microchannel

2.1 Techniques for flow visualization

The spatial dimensions and the dynamic nature of multiphase microfluidic systems imposes unique requirements on the time and spatial attributes of the flow observation techniques. Table 2.1 summarizes different experimental techniques for characterizing microscale multiphase flow as well as their associated spatial and temporal measurement resolutions. Intrusive measurement probes are generally not an option for micro- and nanofluidic systems [121].

Optical microscopy, the most commonly used imaging technique, requires direct optical access to the microfluidic network. A popular option is to use bright-field microscopy and a sufficiently short camera shutter time. Digital

Technique	Spatial dimension	Spatial resolution	Temporal resolution
Brightfield microscopy	2D	~ 1 μm	0.2-33 ms
Fluorescence microscopy	2D	~ 1 μm	33 ms
Confocal microscopy	2D/3D (SC)[a]	~ 1 μm	$\sim$500 ms (2D), $\sim$1 min (3D)
	2D/3D (SD)[a]	~ 1 μm	$\sim$70 ms (2D), 0.1-1 min (3D)
Transient magnetic resonance imaging (MRI)	2D/3D (SC)[a]	~ 800 μm	150 ms

Table 2.1: Experimental techniques available to study multiphase flow in microsystems with their spatial and temporal resolution [121]

cameras that acquire several thousand frames per second are often used to record fast transient events such as microdroplet formation and breakup. If at least one of the liquid phases is fluorescently labeled with an organic dye, fluorescent microscopy reveals the phase distribution, the shape of the fluid interphase, or the local species concentration inside one phase in a multiphase microfluidic network. However, for time-dependent microflows (e.g., bubble and droplet flows) the temporal resolution is often too low to capture the details of the flow. One can obtain a time-averaged value of the fluorescent field by illuminating the whole channel and then integrating the fluorescence information over the entire channel depth, h (see figure 2.1(b)).

Another microscope-assisted technology is microscale particle image velocimetry (μPIV). This method determines velocity vector fields within the depth of field (the distance between the nearest and the furthest objects that give an image judged to be in focus in a camera) by locally cross-correlating two successive particle-images and thereby determining the local displacement of the seeding particle images [122]. The dominance of surface tension and the regularity of interfaces (microbubbles/drops) in microscale flows are advantageous and make PIV a much more suitable technique to study microscale multiphase flows compared to the case of macroscale flow. For steady or periodic flows, two-dimensional velocity fields can be reconstructed by successively obtaining velocity fields in different image planes.

Confocal microscopy excludes out-of-plane information in fluorescence measurements and allows, for steady systems, three-dimensional information to be acquired slice-by-slice. It is therefore often the technique of choice to obtain local intensity measurements for steady microscale flow and transport problems. However, for multiphase microfluidic systems, poor temporal 3D resolution often limits the applicability of the technique.

2.2 Design for gas-liquid contactor

In section 1.3.6, we presented the flow regimes observed when a gas and a liquid flow through a square microsystem with a square cross-section. There

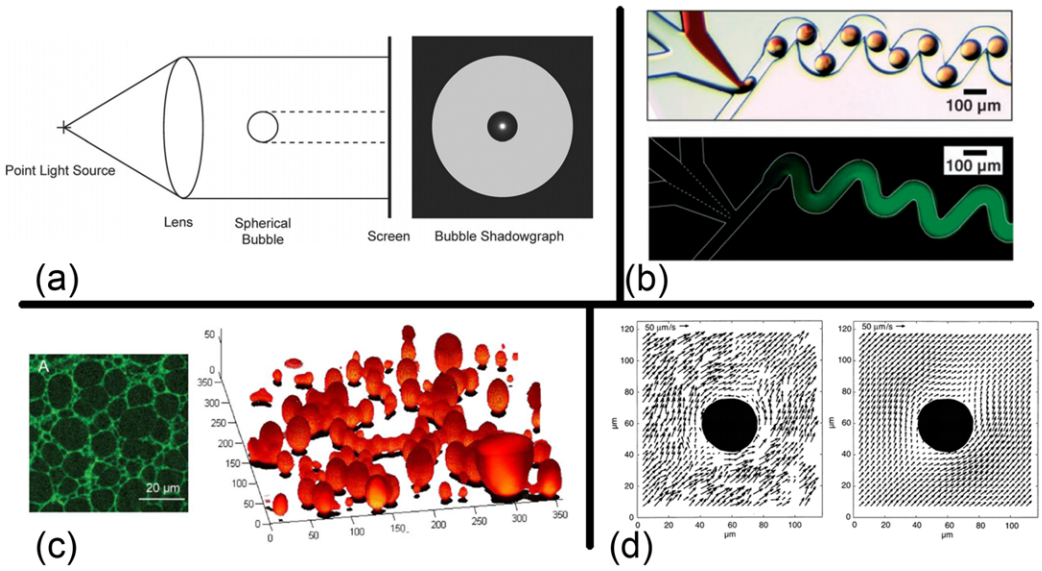

FIG. 2.1: (a) Basics of shadowgraphy for a spherical gas bubble in a liquid medium. Shadowgraphy provides much more accurate information on the bubble (droplet) shape and size than front lighting photography and is a suitable method to investigate bubbles dynamics in fluid mechanics. For a bubble, light refraction is strongest at the gas-liquid interface. No refraction occurs in the liquid or exactly at the center of a spherical bubble; and the interface reflects a considerable amount of backlight [123]. (b) Bright-field and fluorescence microscopy images of plugs moving through winding channels. The observed fluorescence is a time average of the fluorescence of many plugs passing through the field of view [124]. (c) Examples of Confocal Scanning Laser Microscopy images of liquid/liquid dispersions.Two dimensional micrograph and the three-dimensional reconstruction of an oil-in-water emulsion [125]. (d) Instantaneous and averaged vector field measurement by µPIV microscopy of a Hele-Shaw flow around a 30 µm obstacle [122].

are countless microchannel geometries possible to manipulate fluids , but there RE only a few designs achievable to generate a gaseous dispersed phase at the mixing section of a microdevice. Depending on the mixing section layout, one can obtain different regimes or different flow characteristics (e.g. bubble velocity, size and spacing) for the same flow rates. Moreover, most empirical, theoretical and numerical relationships established are geometry-specific, dependent not only on the cross-sectional shape but also on the mixing area characteristics.
Here we present the different approaches that have emerged to generate a regular, stable and mono disperse flow of bubbles in a microdevice.

Centerline injection

A typical example representing the geometry of co-flow devices is shown in figure 2.2(a). A cylindrical glass tube is aligned within an outer channel of square or circular cross-section. The gas is injected in the inner tube, while the liquid flows in the outer channel. This design was first applied to microfluidics by Cramer [126].

T-junction

In this approach, a liquid phase pinches the gaseous thread at the T-shaped junction of three channels (two inlets, one outlet). It was first implemented by Thorsen [127] (see figure 2.2(b)).

Focusing sections

(i) Flow-focusing: In this design, first implemented by Anna et al. [128], bubbles are generated at the junction of three inlet channels and one outlet. The gaseous phase is injected in the center channel, and is pinched by the liquid flowing from the two side channels. A constriction focuses the flow and facilitates the generation of bubbles (see figure 2.2(c)). Typically, such devices have a plane geometry with a very large aspect ratio, i.e a height much smaller than the width, resulting in strong 2D effects.

(ii) Hydrodynamic focusing: In this mixing section geometry, a gas thread is pinched by two opposite liquid streams perpendicular to the gaseous inlet channel. This geometry differs from the flow focusing design, as the gaseous thread is focused solely by hydrodynamic effects and is not assisted by the presence of a constriction. This approach is usually implemented using a cross-shaped mixing section.

In this thesis, we chose this approach (figure 2.2(d)), as it has several advantages compared to other geometries. First, its simplicity makes it an attractive choice, as the cross-shaped mixing section using square microchannels exhibits a single length scale to describe the geometry. In other layouts relying on the flow focusing technique, there is a multitude of possible length scales [129] (see figure 2.2(c)). Moreover, bubbles generated in a cross-shaped section detach from the gaseous thread at the center of the junction, allowing the accurate examination of the pinching processes.

The ability to generate periodic monodisperse bubbles in a cross-shaped mixing section by hydrodynamic focusing relies on the supply of two identical liquid streams from the side channels. The precise symmetry of the junction and the regularity of the channel's cross-sections are two properties required to satisfy this condition, which can be attained by micromachining the microdevice. This process is highlighted in the next section.

2.3 Microchannel fabrication

The microchannels used in this thesis were constructed by Thomas Cubaud. The experiments described later in this thesis rely on the unique attributes of the microdevices, which stem from the fabrication processes highlighted here. The microchannels are made of glass and silicon using microfabrication techniques first applied to the microelectronic systems (see figure 2.3). Patterns of etch resist are defined on a silicon wafer and relief structures are then created with reaction-ion etching. A channel mask is printed in positive with a high resolution printer on transparent paper for lithography. Photoresist

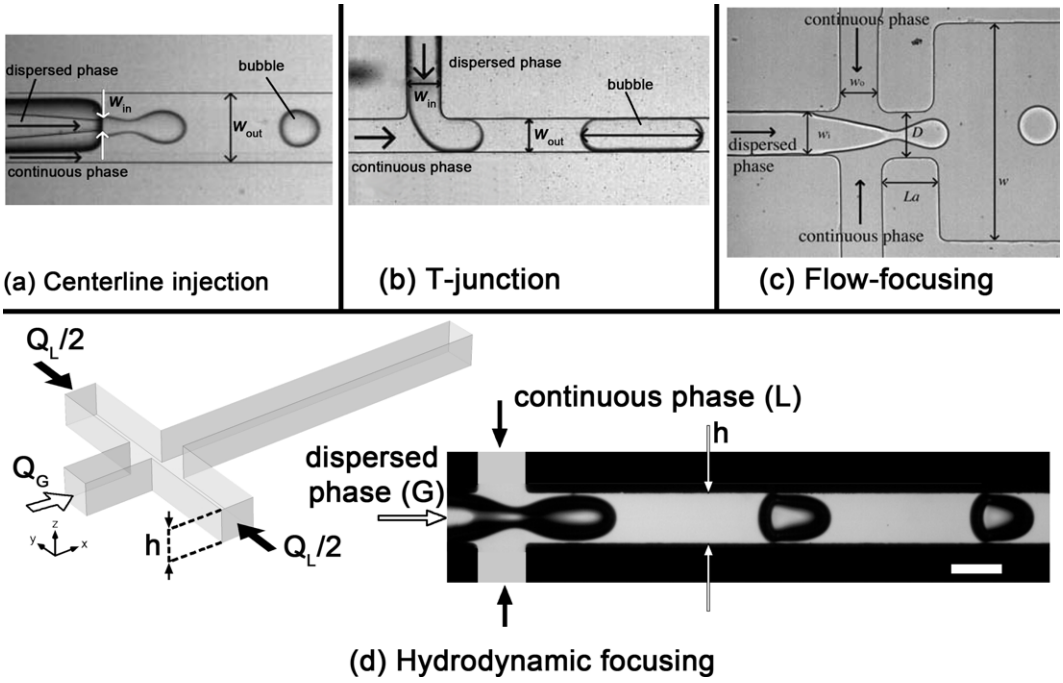

FIG. 2.2: (a-c) PDMS-based microfluidic bubble dispensers using different channel geometries [130]. (d)Bubble generation at the cross-shaped mixing section of a square microchannel. Scale bar is 250μm.

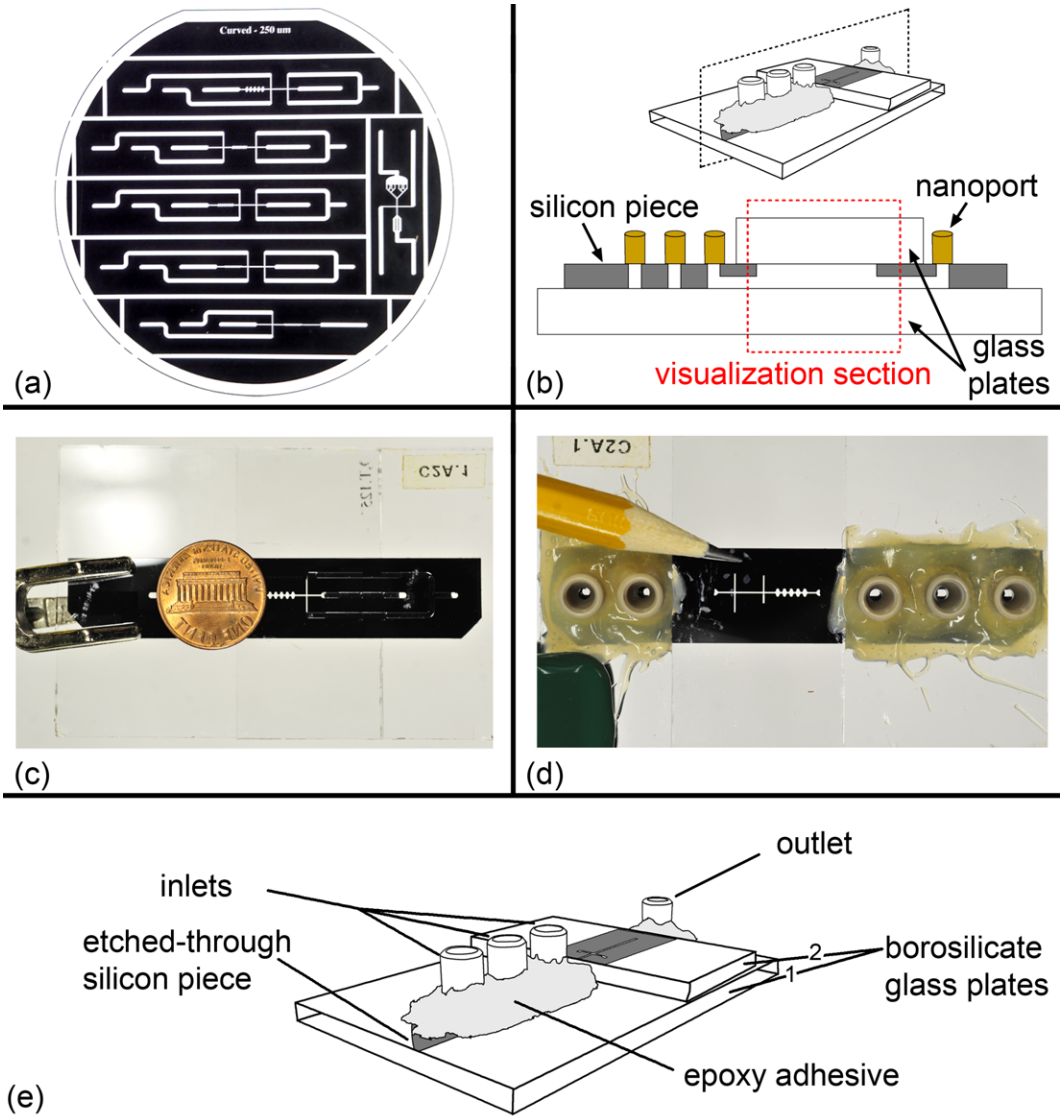

FIG. 2.3: (a) Mask transferred onto a silicon wafer to etch the microchannels using reaction-ion etching. (b) Side view of the final microchannel. (c-d) Pictures of microchannels of square cross section 250 µm , view from bottom (c) and top (d). (e) Schematic of a typical microchannel used in this thesis.

is spin-coated on a polished silicon wafer. The wafer is then exposed to UV light through the mask. The parts of the resin layer exposed to UV light are removed by immersion in a developer bath. Channels are etched at different depths depending on the time and intensity of exposure using deep reactive ion etching. This technology allows a spatial resolution of about 100 nm and the formation of truly vertical walls. The silicon wafer is then cut in several pieces, each of which are then sealed to glass plates, the support of the microdevice (glass plate 1 in figure 2.3(c)). The silicon wafer section dedicated to flow analysis is then covered using another small Pryrex glass plate (glass plate 2 in figure 2.3(c)) using anodic bonding, providing clear visual access. Upchurch Nanoports® are then glued to at the inlets and outlet using with epoxy adhesive to provide a world-to-chip connection. The nanoports are designed to provide consistent fluid connections for Lab-on-a-Chip devices and eliminate the dead volume traditionally associated with chip-based connections.

Similar to the microchips used here, the first microfluidic devices were composed of silicon and glass, since the techniques for fabrication using these materials were well-developed following the integrated circuit revolution. More microfabrication methods have since become available and microchannels can now be created on polymeric, glass and metallic substrates. Here, we briefly discuss the fabrication of microstructure using polymers, but the reader is referred to the recent review by Prakash and Kumar [131] for a general state-of-the-art description of other techniques.

Silicon based techniques are expensive and time-consuming and they require access to specialized facilities such as clean rooms. In the late 1990's, the Whiteside group pioneered the use of the soft lithography method for the rapid prototyping of microfluidic systems in elastomeric materials [132] (most notably cross-linked polydimethylsiloxane or PDMS). A microdevice fabrication using this procedure is easier, more flexible, and much less expensive than other methods.

However, microchips made of glass and silicon confer numerous advantages compared to "soft" microchips. First, the flow visualization in a glass/silicone microdevice using a microscope is remarkable, as the flow is bounded by two

clear glasses pieces. This feature also allows backlight lighting and clear, sharp contrast at the interfaces. Moreover, while soft microchips tend to deform themselves when operated under high-pressure conditions (e.g. when using viscous liquids), silicon-based nano fabrication techniques offer the possibility to construct non-deformable microchannels. Finally, a silicon/glass sandwich structure (the silicon wafer being sandwiched by the two glass pieces) is preferred over a PDMS-made module as (1) it is impermeable to gases, allowing us to perform precise measurements and obtain meaningful quantitative data (2) all the solvents used in this thesis wet both the silicon and the glass very well. This last aspect is especially important because it ensures that bubbles are always surrounded by a thin wetting film.

2.4 Experimental set-up

The experimental set-up described here will be applicable to all experiments described in this thesis unless otherwise noted. Each microchannel has a different channel network geometry and different fluids are employed, but the general set-up is always somewhat similar.
A schematic of the experimental apparatus is displayed figure 2.4 and described in the legend.
The flow rates and pressure are adjusted using the pressure regulator and the syringe pumps. Using the low frame-rate live view of the ultra-rapid camera, we wait for the flow to reach steady-state before triggering the image capture. Depending on the flow characteristics,a typical recording lasts from a few ms to a couple seconds. The images are exported as tif files (typically between 500 to 2000 images per capture) and are examined using ImageJ to validate the steadiness of the flow. The tif sequence obtained is then saved in a folder named using the values of the controlled/measured parameter (i.e flow rates, gas injection pressure and frame rates).

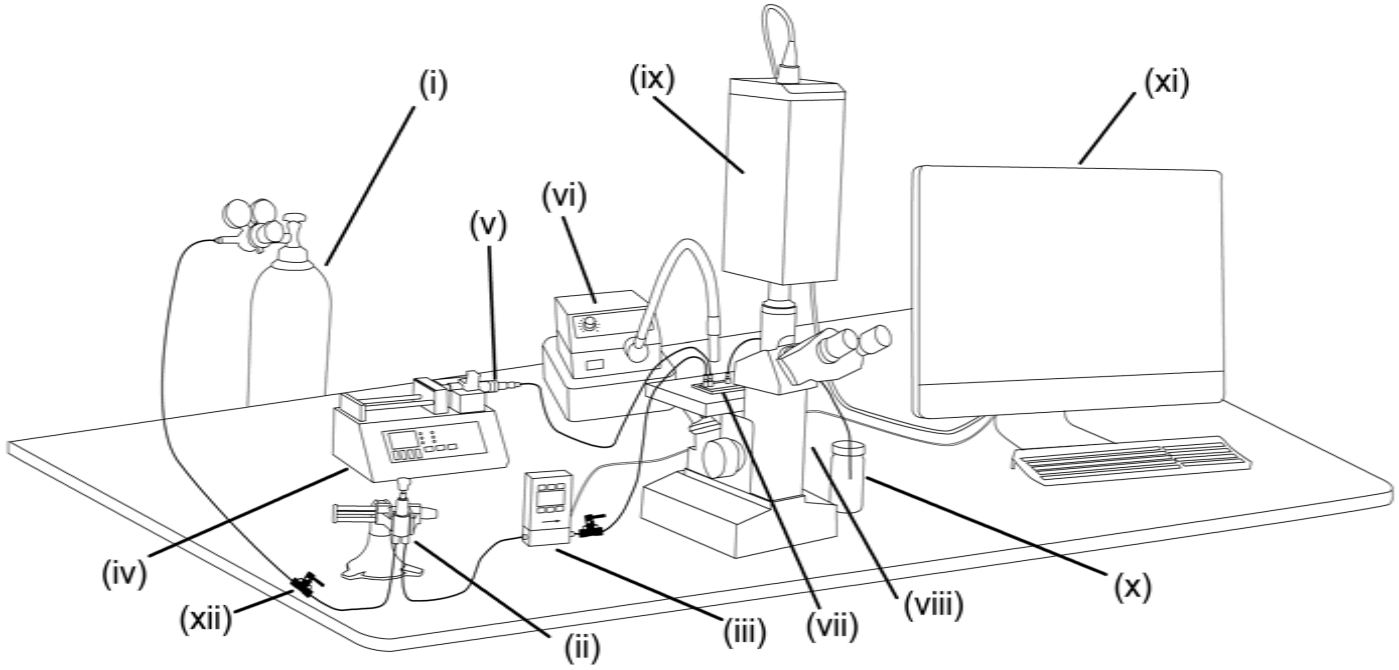

FIG. 2.4: Schematic of the typical experimental set-up. The gas is supplied to the microchannel (vii) by a pressurized tank (i). Prior to reaching the microchannel, the gaseous tubing goes through a miniature pressure regulator (ii) allowing to control the gas inlet pressure P_G which is measured accurately by pressure sensor. A mass flow meter (that can be connected to the computer using Labview) (iii) measures the inlet gas volume flow rate Q_G. The liquid is supplied to the microchannel from the syringe (v) using one or two syringe pumps (iv) depending on the microchannel geometry. The syringe pump(s) deliver the liquid at a flow rate Q_L. As channels are transparent, the light source (fiber light) is placed at the other side of the channel (vi). The flow is examined using an inverted microscope (viii) equipped with a high speed camera (ix). The imaging system is controlled by the experimentalist using the computer interface (xi), allowing to record images at a chosen frame rate. The fluids then exit the microchannel to reach the outlet (x). Perfluoroalkoxy alkanes tubes with an inner diameter of 0.51 mm are used for external connections. Valves (xii) are used to stop the gaseous flow when needed.

The bubbles generated at the hydrodynamic focusing section are recorded as they travel downstream and are monitored along the flow direction to obtain the temporal evolution of the characteristics of individual bubbles, such as position $x_B(t)$, size $d(t)$, and average distance to neighboring bubbles $L(t)$. Analyzing the temporal evolution of individual bubbles is more useful compared to the spatial evolution because of the variation of local average multiphase velocity that depends on the flow's immediate structure. Therefore, the method of description that follows individual bubbles (i.e., Lagrangian approach) is preferred to the method of description that focuses on the properties of the flow at a given location in space (i.e., Eulerian approach). In the next section, we describe how we obtain some of the flow characteristics using image processing and analysis.

2.5 Image processing and analysis

During an experimental session of a few hours, its is possible to collect as much as 10 gigabytes of images. To process such a large amount of data efficiently, we automated parts of the image processing and data analysis stages. The procedure generally followed for processing images can be divided in two portions: (1) determination of the strategy to follow in ImageJ in order to extract the desired information from the original files (2) automation of the process using ImageJ macros. During the first stage, we make use of ImageJ basic functions (rotate, threshold to binary, crop, fill, wand) and advanced plugins (skeletonize, background mod,...) to obtain the wanted data from one image. Once a strategy has been confronted with success to several images from several data sets, we use a combination of ImageJ functions and code-writting to automate the process using a macro. As automated image processing is hardly ever beneficial when run in a fully systematized fashion, I use a combination of user-input parameters and dialog features, allowing the user to interact with the program. Such programs can become relatively complex, but always use the same basic functions, an attribute which facilitates considerably the task and reduces the programing time.
The basic structure of the image processing is presented figure 2.5.

When computing more complex parameters such as the bubble volume, the data is post-processed using MATLAB scripts. Given the high number of variables of interest, including but not restricted to the bubble coordinates over time, its volume, area, variables are saved with a name associating it with its data source, in the same manner of a barcode. Because this name is unique, it allows us to access it quickly without any risk of error when using with IgorPro, the software used for data analysis.

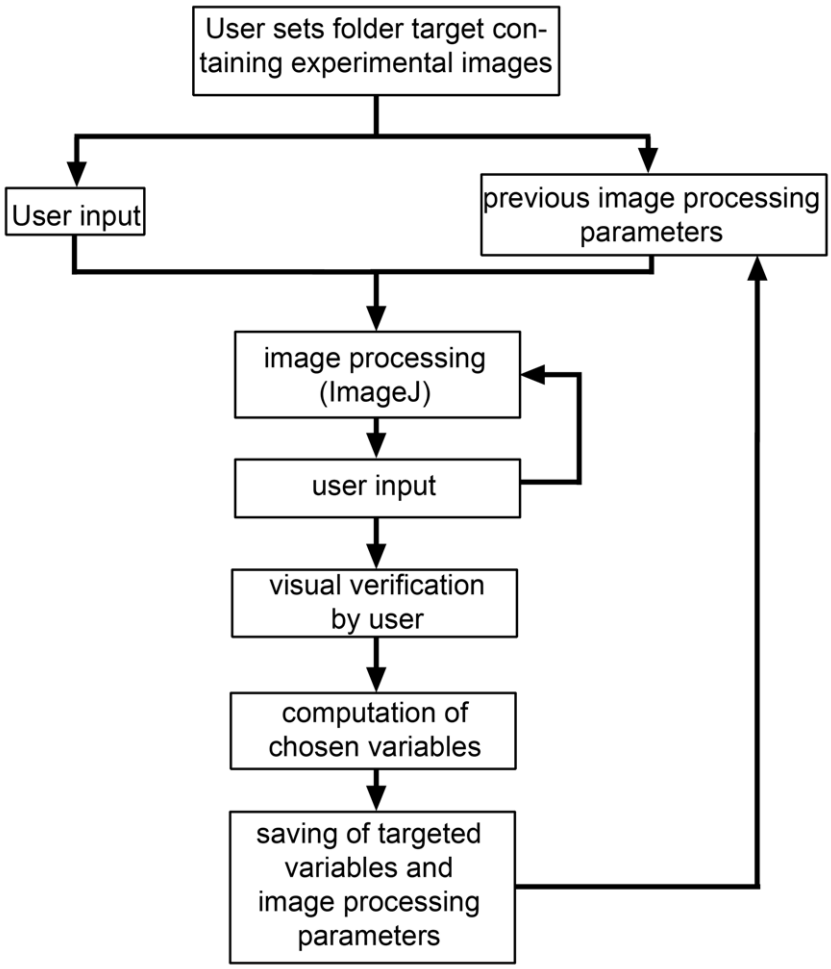

FIG. 2.5: Basic structure of the image processing task. Processing parameters include threshold values for binarization of the images, cropping coordinates, rotation values,... Target variables include the bubble length, volume, area, coordinate, cusp curvature,...

Chapter 3

CO_2 microbubble dissolution in low viscosity solvents

In this section we tackle the dissolution of gaseous CO_2 in low viscosity solvents. The flow of CO_2 micro bubbles in microchannels of width $w \approx 250\mu$m in water, alcohols and alkanes exhibits all the characteristics of the flow observed by Taylor 50 years ago and investigated by many researchers since. It is however important to note that contrary to the situation considered by Taylor, the bubbles here can not be considered semi-infinite (typically, we have $d < 6w$).

In the first section, we investigate the dissolution of CO_2 bubbles in water in a long microchannel. This allow us to observe three flow regimes that we characterize depending on the flow conditions. We also examine interplay between the dissolution process and the structure of the flow.

In the second section, we focus on the initial dissolution behavior of CO_2 bubbles in alcohols and alkanes. Focusing on the initial behavior allows us to build a model for the mass exchange that we later confront to our experimental results with success. We then study the impact of the molecular structure of the solvent on the mass exchange process.

3.1 CO_2 Dissolution in water using a long microchannel

The experiments were conducted by Ruopeng Sun in 2011 at the end of his Master. Data were examined in detail by Thomas Cubaud and myself and published in Biomicrofluidics [133]. This section serves as an introduction to microfluidic multiphase flows and as a preliminary study of the dissolution of CO_2 in microchannels.

3.1.1 Motivations

The system carbon dioxide-water is particularly important to the environment. When CO_2 dissolves in water, it creates a weak acid, which can affect not only marine microorganisms [134] but also the geochemistry of subsurface rocks. The rising global average temperatures have had profound impact on the oceans, the largest CO_2 sink on earth. The changing oceans' temperature and acidity has already affected the ocean ability to uptake CO_2, but the magnitude of potential feedback mechanisms is currently unknown. Researchers address this issue primarily through modeling and time-consuming field studies, but the numerous parameters impacting the seawater solubility (temperature, acidity, pressure, mixing,...) makes it difficult to investigate this issue in a systematic manner. A method for enriching minute amount of water with CO_2 on-chip would facilitate biological and chemical studies concerned with the impact of carbon dioxide on micro environments.

Here, we examine the behavior of diffusive bubble multiphase flows using long serpentine microchannels (see figure 3.1(a)). Multiphase flows are monitored at the bubble level over very long distances, allowing the observation of a wide range of initial conditions and flow rates. While the large specific interfacial area of microscale bubbles enhances mass transfer, dynamic rearrangements between bubble, however, can significantly alter dissolution performance. To better understand the fundamentals of collapsing bubble microflows, the evolution of the bubble size d and inter-spacing L is measured for various flow rates and injection pressures (see figure 3.1(b)). The mor-

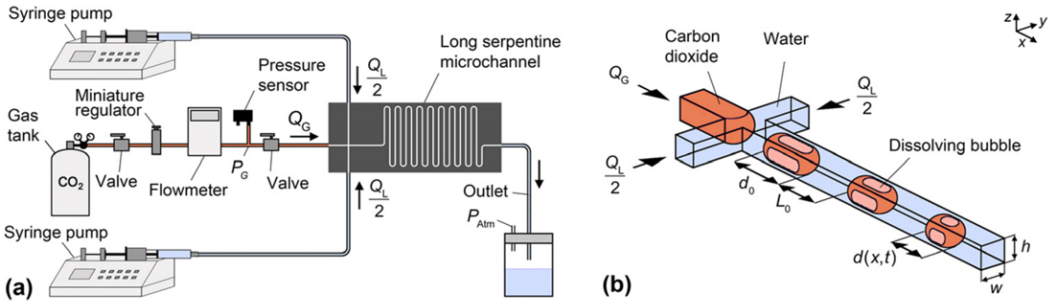

FIG. 3.1: (a) Schematics of experimental setup. (b) Generation of dissolving bubbles in hydrodynamic focusing section [133].

phological transition from segmented to dilute bubbly microflows is examined and we establish the bubble size-velocity relationship taking into account the local volumetric fraction. Over long distances, small bubbles convected in the parabolic flow profile can drift from their relative position in the train. For a specific range of initial sizes and liquid volumetric fractions, the dislocation in the relative bubble position in the arrangement can trigger cascade of coalescence events leading to the formation of a slow leading bubble. This mechanism significantly coarsens the flow and deteriorates the dissolution quality. We discuss the implications between collapsing bubble hydrodynamics and dissolution processes in constrained microgeometries.

3.1.2 Bubble formation and critical volume fraction

Bubbles are produced at the junction made between the CO_2 gas inlet channel (central channel) and the water inlet channels (side channels) (see figure 3.2(a)). The distance x is measured along the main channel axis. The initial bubble size d_0 and spacing L_0 are recorded from experimental micrographs after bubble detachment from the inlet channel.

The bubble size d is measured between the tips of the two end-caps. Experiments are conducted from low to moderate Reynolds number Re varying between 1 and 50. Overall, the bubble size increases with the gas flow rate Q_G while the length of the liquid plugs increases with Q_L . Previous studies [135, 136] have shown that d_0 is inversely proportional to the initial volumetric

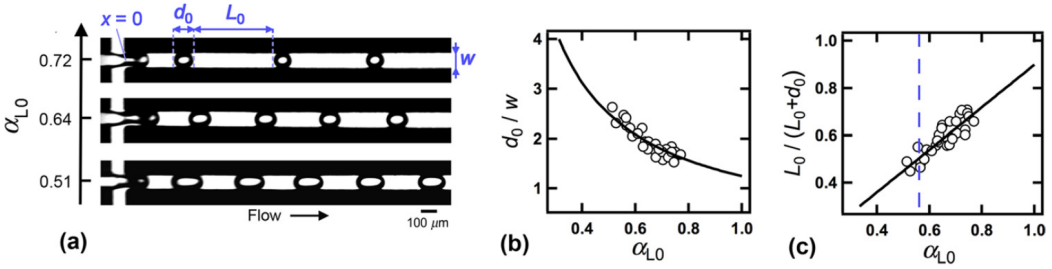

FIG. 3.2: Initial morphology of segmented flows. (a) Examples of CO_2 bubble generation at the focusing section for various initial volumetric liquid fractions α_{L0}. (b) Initial bubble size d_0 vs. volume fraction α_{L0} and solid line: $d_0/w = 1.25/\alpha_L$. (c) Comparison between calculated liquid fraction $L_0/(L_0 + d_0)$ and injected volume fraction α_{L0} near the focusing section, solid line: $L_0/(L_0 + d_0) = 0.9\alpha_{L0}$, and dashed-line: critical volume fraction $\alpha_{L0} = 0.55$ [133].

liquid fraction

$$\alpha_{L0} = \frac{Q_L}{(Q_L + Q_G)}, \tag{3.1}$$

according to

$$d_0/w \approx a/\alpha_{L0}, \tag{3.2}$$

with a being a prefactor depending on the channel aspect ratio. Here, we find that the value $a \approx 1.25$ yields a good fit of experimental data (see figure 3.2(b)). The normalized initial bubble length d_0/w is varied between 1.5 and 2.5 to probe bubble dynamics associated with the transition from segmented to bubbly flows and to evaluate the performance of the proposed CO_2 dissolution method in long serpentine microchannels.

In addition to determining the initial spatial distribution of the liquid and gas phases, the initial volumetric liquid fraction α_{L0} plays a critical role in the dissolution process. At standard ambient temperature and pressure (i.e., at 25 °C and 1 atm), the solubility of CO_2 in water is relatively low. When expressed in grams of solute per liter of solution, the solubility of CO_2 in water is $S \approx 1.5$ g/l. Therefore, the minimal liquid fraction required to achieve complete CO_2 dissolution in water is

$$\alpha_{LC} = 1/(1 + S/\rho) \approx 0.55, \tag{3.3}$$

where the density of CO_2 is $\rho = 1.8$ g/l. This critical liquid volume fraction α_{LC} remains relatively independent of pressure P in our system since, on the one hand, the solubility S is proportional to pressure P according to Henry's law and reference data for pressure below one MPa, and, on the other hand, the density ρ is also proportional to P assuming ideal gas behavior. Therefore, the parameter S/ρ should not depend on pressure and the critical volume fraction $\alpha_{LC} \approx 0.55$ is assumed independent of the gas injection pressure P_G.

In steady segmented flows, mass conservation between each bubble yields a simple relationship between the geometrical parameters d_0 and L_0 and the initial volume fraction according to

$$L_0/(L_0 + d_0) \sim Q_L/(Q_L + Q_G). \tag{3.4}$$

Bubble measurement introduces an error due to the bubble caps and experimental data are fit with $L_0/(L_0 + d_0) \approx k\alpha_{L0}$, with the prefactor $k \approx 0.9$ (see figure 3.2(c)). This functional relationship is particularly useful for estimating the evolution of the volume fraction $\alpha_L(t)$ along the serpentine microchannel from micrographs. During dissolution, the effective gas flow rate along the channel decreases as

$$Q_G(t) \approx Q_G - Q_{Diff}(t), \tag{3.5}$$

with Q_{Diff} being the rate of gas volume absorbed in the liquid, while the liquid flow rate Q_L remains essentially constant given the large difference between liquid and gas densities. Complete dissolution is obtained when the liquid fraction $\alpha_L = 1$, which should, in principle, be possible for multiphase flows formed when $\alpha_{L0} > \alpha_{LC}$.

3.1.3 Bubble dissolution

Convective liquid/gas mass transfer is enhanced in confined geometries due to the recirculation motion inside the liquid plugs. This motion facilitates the homogenization of dissolved CO_2 in the water (figure 3.3(a)). For a given set of flow parameters, the local bubble concentration varies in opposite way compared to the local CO_2 concentration in the liquid plugs. According to

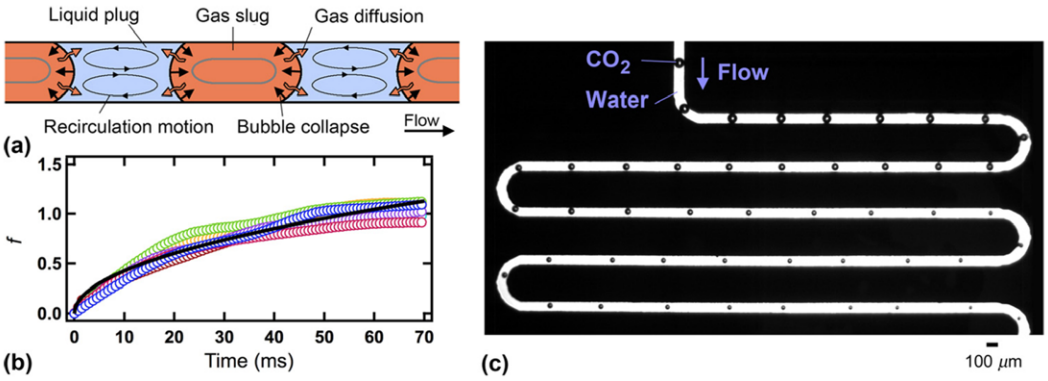

FIG. 3.3: Bubble dissolution process in long microchannel. (a) Schematic of enhanced gas/liquid diffusion mechanism. (b) Temporal evolution of $f = (d_0 - d(t))/w$ *for* P_G= 12 *psig with an initial volume fraction* α_{L0} *ranging between 0.56 to 0.77. Solid line:* $f = at^{1/2}$*, with* $a = 4s^{-1/2}$*. (c) Transformation from segmented to dilute bubbly multiphase flows,* P_G= 10 *psig and* $Q_L = 100\mu L/min$ *[133].*

Fick's law, mixing in the plugs is expected to increase the diffusion flux since the local reduction of CO_2 concentration in water near the bubble interface accentuates the concentration gradient ∇C. Here, we do not focus on the chemical reactions occurring between dissolved carbon dioxide and water, but rather turn our attention to the dynamics of bubble collapse and its implication for multiphase flows in microgeometries.

For elongated bubbles, the initial shrinkage rate depends on the gas inlet pressure P_G. The parameter

$$f = d_0/w - d(t)/w \tag{3.6}$$

is useful for removal of the dependence on the initial size d_0 and is related to the diffusion volumetric flow rate according to

$$df/dt \sim Q_{diff}/hw \tag{3.7}$$

for elongated bubbles $d > w$. For relatively long periods of time ($t > 1$ ms), we previously showed that bubbles follow a Fickian behavior according to

$$f \sim t^{1/2}. \tag{3.8}$$

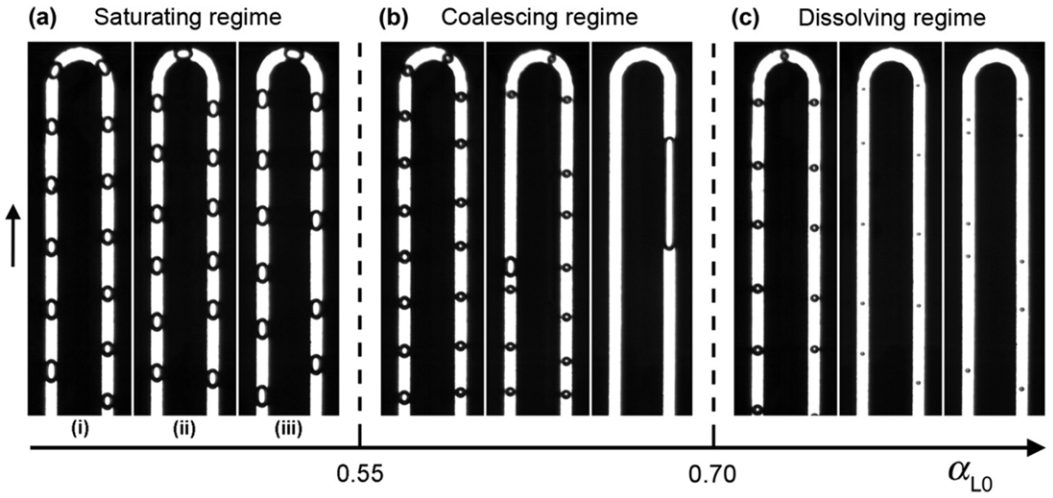

FIG. 3.4: Operating regimes as a function of initial volume fraction α_{L0}, spatial evolution of flow at various locations: (i) high-pressure region, $x/w \sim 50$, (ii) medium-pressure region, $x/w \sim 450$, and (iii) low-pressure region, $x/w \sim 900$ [133].

In the present study, we focus on detailed bubbles dynamics for relatively large pressure P_G= 12 psig and long periods of time. We find that the function $f = at^{1/2}$, with $a = 4s^{-1/2}$, approximates well experimental behavior for a range of initial bubble sizes d_0 (see figure 3.3(b)). Similar to previous findings by Sun et al. [41], data points collapse onto a master curve (figure 3.3). For long time evolution, differences arise depending on the local CO_2 concentration and for small bubbles $d < w$, but overall the initial trend is similar.

The bubble size $d(x, t)$ plays an important role on diffusive multiphase flow dynamics. When $d > w$, the flow consists of arrays of elongated bubbles, or gas slugs, separated by continuous liquid plugs. This regime is usually referred to as segmented flow. For small sizes, when $d < w$, bubbles are not directly confined by the walls and adopt a spherical shape. This regime corresponds to the bubbly flow. A consequence of the bubble size reduction is the spatial transition from segmented flow (upstream region) to dilute bubbly flow (downstream region) (figure 3.3(c)). The morphological evolution of bubbles as they progress along the channel induces complex dynamics.

The use of serpentine channels allows us to examine the long time evolution

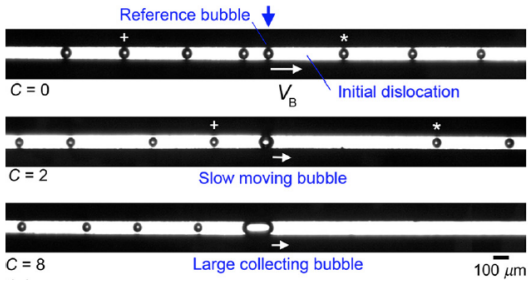

FIG. 3.5: Time-series of the evolution of a large reference bubble generated by successive coalescences. The symbols $\star$ and $+$are used to label specific bubbles, while C is the number of coalescence events [133].

of flow morphologies. Lengthy channels also permit the building of rather large pressures, which is practical for enhancing gas dissolution processes. Given our long microchannel $L/w \sim 10^3$ and approximating a linear pressure drop, we label channel sections such as high-, medium-, and low-pressure regions. A complexity of this type of flow is rooted in the fact that the diminution of the local pressure $P(x)$ along the flow direction reduces solubility and slows down dissolution dynamics. Although the overpressure inside a bubble is inversely proportional to its radius r according to Young-Laplace law, we experimentally find that dissolution rates do not necessarily self-accelerate for tiny bubbles and the bubble size appears to saturate in the downstream region. In the low-pressure region, we also observe instances where bubbles grow in size, possibly due to a combination of decompression and lower solubility effects. In addition, coalescence phenomena can significantly alter flow morphologies and dissolution efficiency. Over the range of parameters investigated, we identify three typical operating conditions depending on the initial volume fraction α_{L0}, namely "saturating regime" for $\alpha_{L0} < \alpha_{LC} \approx 0.55$, "coalescing regime" for α_{L0} ranging between 0.55 and 0.70, and finally "dissolving regime" for $\alpha_{L0} > 0.70$ (see figure 3.4).

In the saturating regime, bubbles shrink in the high-pressure region but their size remains large ($d > w$) and relatively constant in the medium- and low-pressure regions. The flow is stable since bubbles are elongated and convected near the average multiphase flow velocity J_{tot}. For larger α_{L0}, the transition from segmented to bubbly flow is accompanied with an increase

of bubbles velocity V_B compared to J_{tot}. Depending on the initial distance between bubbles L_0, neighboring bubbles may coalesce into larger bubbles. This situation, depicted figure 3.5, is triggered by small fluctuation in size and spacing for neighboring bubbles and is oveall detrimental to dissolution since the liquid/gas interfacial area is reduced. For large α_{L0}, however, coalescence events become rare and stable dilute bubbly flows of tiny bubbles are observed. The dissolving regime corresponds to an efficient operating regime for CO_2 dissolution in water using symmetric hydrodynamic focusing sections in microchannels.

3.1.4 Conclusions

In this section, we investigated the properties and operating conditions of a simple CO_2 /water continuous micromixer. Dissolving microbubbles are produced using a hydrodynamic focusing section connected to a long serpentine channel. For the carbon dioxide-water fluid pair, the saturation concentration of dissolved gas in liquid corresponds to a volumetric liquid volume fraction $\alpha_L \approx 0.55$, which is independent of injection pressure near atmospheric conditions. The relationship between the phase distribution (i.e., bubble size and spacing) and the initial volumetric liquid fraction α_{L0} in microchannels is established.

Three characteristic regimes, including saturating, coalescing, and dissolving are located as a function of α_{L0}. We examine the morphological and dynamical transition from segmented to dilute bubbly flows. For segmented flows, the bubble spacing remains approximately constant, while for bubbly flows, the bubble spacing increases when bubbles shrink. Monitoring individual bubbles along the flow direction is used to calculate the temporal evolution of the liquid volumetric fraction, which in turn is utilized for computing the average flow velocity at the reference bubble location. Experimental findings show that the instantaneous bubble velocity normalized by the average flow velocity is a simple function of the bubble size. Finally, we examine the implication of this relationship during coalescing flows that severely limit the efficiency of the dissolution process.

For practical applications, the dissolving regime appears optimum for achieving CO_2 dissolution in water using a simple microfluidic apparatus. Various target CO_2 concentrations in water can be realized for $\alpha_{L0} > 0.7$. Microfluidic systems connected to pressurized inlet and outlet ports would permit a wider range of CO_2 mass concentration in water. In particular, since fast dissolution dynamics are expected at large pressures, devices operating at large pressures may prevent drifting bubbles from merging before attaining the plateau velocity (i.e., near the maximal velocity of the parabolic profile), which should, a priori, suppress the coalescing regime. The saturating flow regime is also of interest due to its robust hydrodynamic stability and the possibility for reaching the saturation limit of CO_2 concentration in water. In this case, segmented flow with long bubbles is advantageous because bubbles can make direct contact with the walls depending on dynamic wetting conditions and be removed from the flow using hydrophobic porous membranes [137, 138]. A variety of microfluidic designs can be implemented to circumvent current limitations in the manipulation of carbonated microflows.

3.2 Proposed model for initial gas-liquid mass exchange in microgeometries

In this section we propose a model for mass exchange in segmented flow for short time after the generation of the bubble.
The gas phase resistance to mass exchange being negligible compared to the liquid phase resistance, we can write (cf. section 1.5.3)

$$J_{mass} = k_L \Delta_C = k_L (C_i - C_L) \tag{3.9}$$

where J_{mass} is the net mass flux (mass of CO_2 exchanged per unit area of interface), k_L is the overall (i.e liquid here) mass transfer coefficient, C_i the concentration of CO_2 the interface, and C_L the CO_2 concentration in the liquid bulk.
According to Henry's Law, which states that the solubility of a gas in a liquid

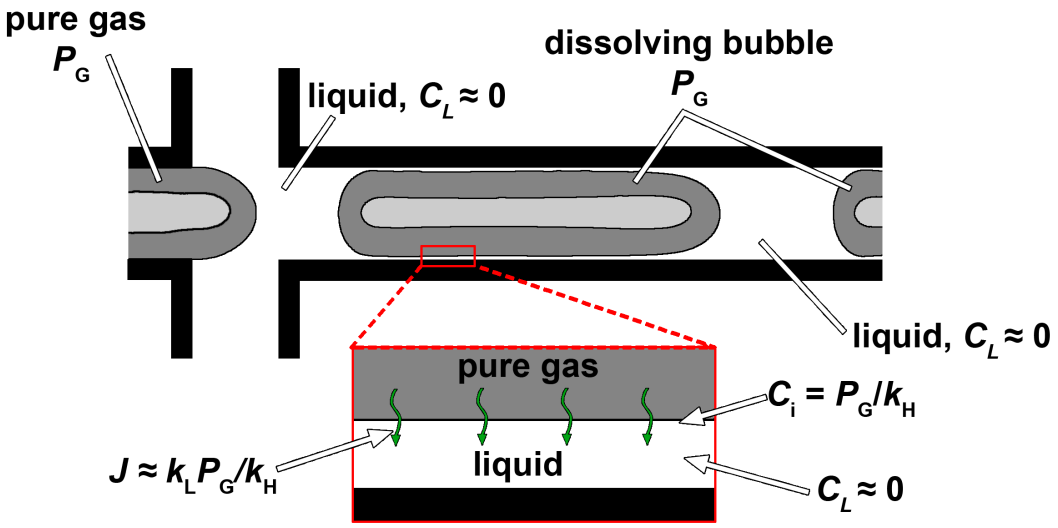

FIG. 3.6: Schematic of the model proposed for the early dissolution of a pure gaseous species in a liquid. The species concentration in the liquid is initially negligible and stays negligible as only a little dissolution occurs during this early regime.

is directly proportional to the partial pressure of the gas above the liquid, we have the following relationship between the CO_2 concentration at the interface C_i and the CO_2 partial pressure in the gas phase P_G:

$$C_i = P_G/k_H \tag{3.10}$$

where k_H is Henry's constant.

In the following discussion, we assume that the gaseous phase consists purely of CO_2, which implies that the partial pressure in CO_2 is equal to the gaseous pressure. As we are interested in the mass exchange in a liquid phase that was stored in contact with air at atmospheric pressure, we can reasonably assume that the liquid concentration in CO_2 is negligible due to the low partial pressure of CO_2 in air. Moreover, because we are interested here in the early behavior of the mass exchange process, i.e. just after the two phases are brought in contact, one can reasonably assume that only little

gaseous CO_2 reaches the liquid phase:

$$C_L \approx 0 \tag{3.11}$$

Combining these assumptions with Henry's Law (equation 3.10), equation 3.9 gives:

$$J_0 = k_L \Delta C \approx k_L P_G / k_H \tag{3.12}$$

According to this proposed model, the early mass flux J_0 is expected to scale with P_G with a coefficient k_D:

$$k_D \equiv \frac{k_L}{k_H} \tag{3.13}$$

where k_D [g.m^{-2}.atm^{-1}.s^{-1}] is the dissolution coefficient associated with our system. k_L [m.s^{-1}] and k_H [atm.m^2.g^{-1}] are respectively the liquid mass transfer coefficient and Henry's constant for the system CO_2/liquid. Overall, the coefficient k_D is a reliable parameter for characterizing the dissolution rate of given fluid pairs and it combines the two fundamentals of gas absorption, namely, saturation through k_H and the dynamics at which the system approaches equilibrium with k_L [82].
We therefore expect the initial mass flux to be proportional to the gas injection pressure P_G:

$$J_0 \approx k_D P_G \tag{3.14}$$

A schematic of the model is presented figure 3.6.

3.3 Dissolution in Alcohols and Alkanes

In this section we focus on the early dissolution process in a segmented flow at low capillary number. We confront our experimental data with the proposed model with success.

Carbon dioxide capture, and subsequent storage (CCS), can be a viable route to reduce emissions of CO_2 into the atmosphere. The widespread use of CCS is currently limited by the cost and energy required for absorption

and solvent regeneration. Selective and fast absorbing solvents are needed to achieve commercial process efficiencies and to minimize capital cost. To design processes and select solvents or mixtures thereof, the intrinsic properties of the mass exchange process must be assessed. However, screening of the continuous composition space becomes prohibitive with standard slow methods. Here, we present a microfluidic method to characterize the dissolution process.

Following the presentation of our proposed model, where we found that the dissolution mass transfer coefficient k_D is a practical parameter to quantify diffusive multiphase flow phenomena in microgeometries, we estimate the dissolution of gaseous CO_2 in both Alkanes and Alcohols by assessing k_D. Systematic studies in the homologous series of n-alkanes and I-alkanols (alcohols), are useful as these liquids might serve as simple model substances. The systematic characterization of the k_D is useful for comparing data with forced-convection mass transfer processes and fluid properties models.

The test fluids for the study of CO_2 in Alkanes range from n-Hexane to n-Dodecane and from in Alkanes ranges from Butanol to Undecanol for the Alcohols. Such a range allows for a clear estimation of the impact of the carbon number on the gas dissolution dynamic. Here, our region of interest is limited to the first $10w \sim 2.5$mm, but the pressures involved are limited, as the test fluids all have a low viscosity. This results in a segmented flow in the microchannel, a thin film of liquid separating the bubble and the micro channel walls. As the bubbles travel downstream, they reduce in size due to the dissolution of CO_2 in the continuous phase.

3.3.1 Elimination of entrance effects

The generation of bubbles in low viscosity solvents at moderate Reynolds numbers creates entrance effects, which impede us to study precisely the dissolution process. In figure 3.7 is represented the flow of two bubbles just after their separation from the gaseous thread. Two cases are represented here:
(1) the case of a moderate Reynolds number (Re $\sim O(1)$) (figure 3.7(a)) where the entrance effects are very important. The associated evolution of the length of the bubble is plotted and exhibits between 3 and 4 large oscillations initially.

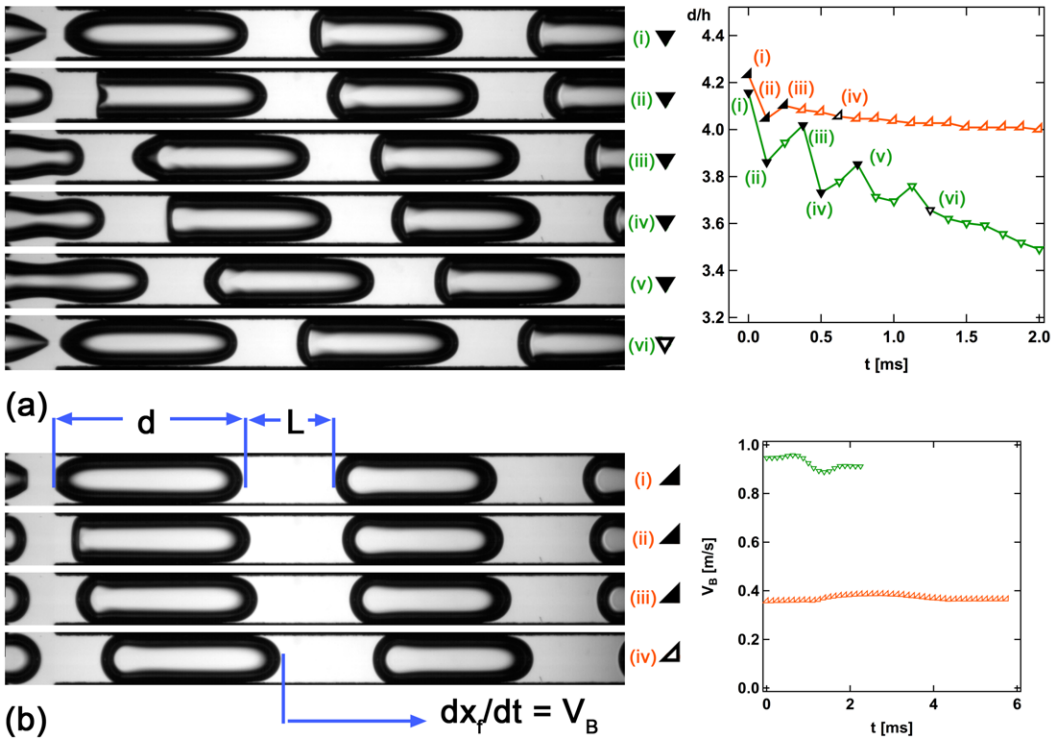

FIG. 3.7: Early behavior of the flow of bubbles at moderate Reynolds number (a); Octane, P_G = 18 psi; Q_L = 1,500μL/min, Re=322, and (b) low Reynolds number; Decane, P_G= 16.54 psi; Q_L =900μL/min, Re=78.

This is due to the generation of surface waves following the release of surface energy when the bubble snaps. The waves are however dampened after the bubble is convected over a distance $L_{entrance} \approx 6w$.
(2) the case of a low Reynolds number (figure 3.7(b)) where the entrance effects are very quickly dampened. Because of the low value of the Reynolds number, the impact of the bubble generation disappear after the bubble travels a distance $L_{entrance} \approx 2w$.

Such entrance effects impedes our ability to accurately follow the evolution of the bubble length, we thus start our analysis of the mass exchange process once the bubbles has been convected over a distance $x_r > L_{entrance}$.
A more systematic study of the entrance effects will be tackled chapter 5.

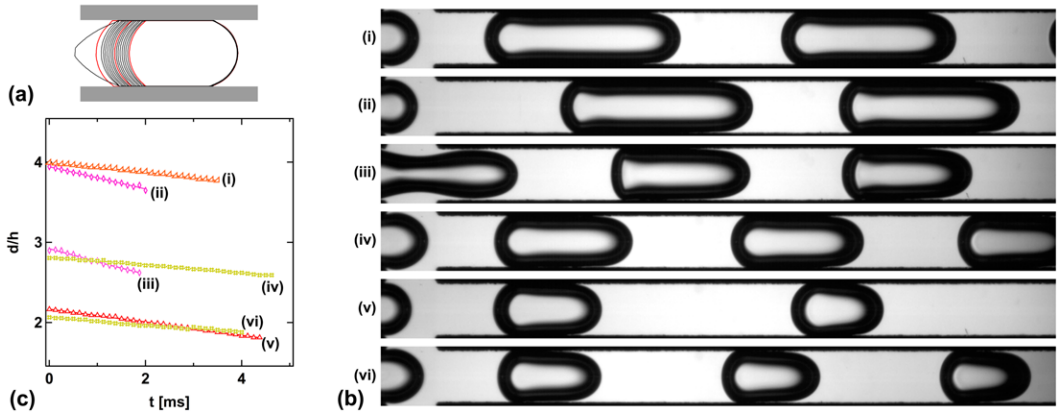

FIG. 3.8: (a) Superimposition of the contours of a bubble dissolving at low capillary number. (b) Micrographs after the vanishment of entrance effect for (i) Decane, P_G = 16.54 psi; Q_L = 900µL/min (ii) Nonane, P_G = 17.54 psi; Q_L = 1,100µL/min (iii) Nonane, P_G = 17.92 psi; Q_L = 1,400µL/min (iv) Dodecane, P_G = 17.24 psi; Q_L = 600µL/min (v) Heptane, P_G = 16.04 psi; Q_L = 1,000µL/min (vi) Dodecane, P_G = 17.66 psi; Q_L = 900µL/min (c) Associated evolution of the bubble length

3.3.2 Early dissolution behavior

Contrary to the long scale dissolution of CO_2 bubbles presented earlier, the dissolution within our Region Of Interest (ROI) has a limited impact on the structure of the flow. The bubble shape is constant, with only a variation in length, as exemplified by the contours superimposition displayed figure 3.8(a). Therefore, the volumetric rate of CO_2 dissolved in the continuous phase can be approximated by:

$$Q_{diff} \approx -h^2 \frac{dd}{dt} \tag{3.15}$$

Here, we have neglected the presence of thin liquid film surrounding the bubble. This is justified because at low capillary number (Ca$< 10^{-2}$), we have $\delta \approx 0.02h$ [79].

The evolution of d versus t for a few experimental sets is displayed figure 3.8(b), and the associated first micrographs once $x_r > L_{entrance}$ is displayed figure 3.8(c). The length of the bubbles appear to be decreasing linearly with time, demonstrating a fast-diffusive behavior, as shown in the article by Sun and Cubaud [41]. This regime is associated with early diffusive behavior, when

the concentration is essentially localized in the thin interfacial region between the liquid and the gas phases. Typically, investigations on the mass exchange in microgeometries overlook this regime to focus on the normal-diffusive regime. To estimate the diffusive mass flux, the interfacial area of the bubble needs to be estimated. To do so, one has two possibilities: (1)consider that the mass exchange occurs through the entire bubble area (2)consider that the mass exchange occurs solely through the cusp because the thin liquid film is saturated. Because of the periodic contact of bubbles with the stagnant liquid film, it is reasonable to assume that the concentration of CO_2 in the liquid film could saturate along the channel length [120]. This argument implies that the mass exchange occurs only through the cusps, a consideration consistent with some experimental results [117, 139]. Here, we approximate the cusps of the bubbles by two hemispherical caps, leading to:

$$A \approx 4\pi(h/2)^2 \tag{3.16}$$

We therefore have the following expression for the mass flux of CO_2:

$$J_{mass} = \rho_{CO2}\frac{Q_{diff}}{A} \approx -\rho_{CO2}\frac{1}{\pi}\frac{dd}{dt} \tag{3.17}$$

The temporal evolution of $\frac{dd}{dt}$ is plotted figure 3.9 for a few representative flows employing alcohols and alkanes. The legend specify the number of carbon n_C in the solvent (e.g. $(n_C)_{alkanes} = 12$ denotes the use of dodecane and $(n_C)_{alcohols} = 8$ the use of octanol). The rate at which the bubble length decreases varies only slightly within the ROI, but do not display the saturation drop that occurs when reaching the normal diffusive mode (where $dd/dt \sim t^{-1/2}$). This suggests that within our region of interest, we are always within the early, fast diffusive regime.

We define the initial mass flux as the averaged flux over the entire ROI:

$$J_{mass,0} = \langle J_{mass} \rangle \tag{3.18}$$

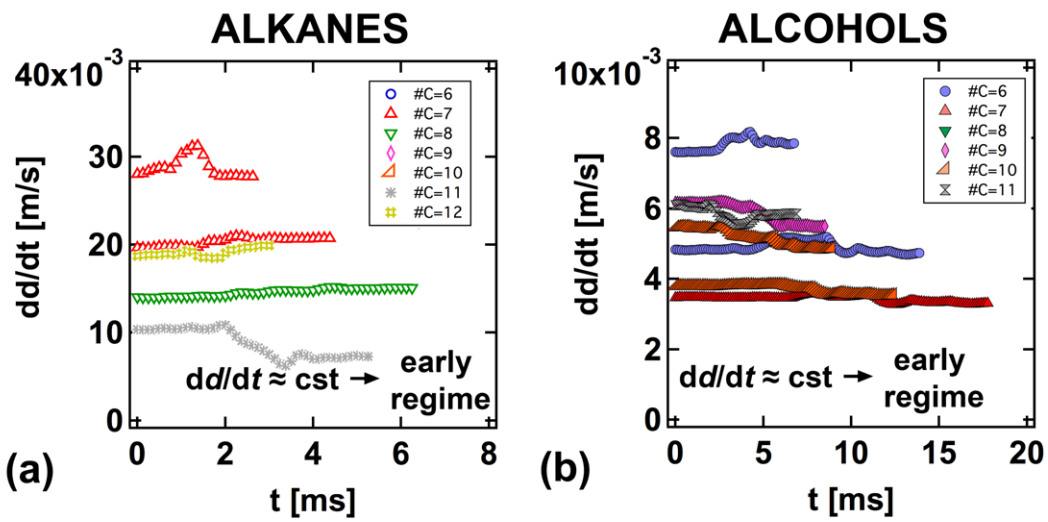

FIG. 3.9: Evolution of the rate at which the bubble's axial length decreases for representative flow conditions. The rate can be considered constant for both alkanes (a) and alcohols (b), resulting in a constant mass flux J_{mass} within the ROI (according to equation 3.17).

3.3.3 Comparaison to proposed model: the bubble as a mass exchanger

To compare our experimental results to our model (see equation 3.14), we plot the initial mass flux as a function of the gas injection pressure figure P_G (see figure 3.17) for the entire experimental data of alkanes and alcohols. While our model predicted the initial mass flux to scale with P_G, our experimental results for the mass exchange in alcohols display a clear dependence on the gauge injection pressure $\Delta P = P_G - P_{atm}$ (see figure 3.10(b)). This fact suggests an exchange of species with absorption of carbon dioxide and desorption of oxygen and nitrogen, both present in the liquid phase since they were stored at atmospheric pressure.

Let us now consider the data for the dissolution in alkanes (see figure 3.17(a)), as it display a slightly different behavior. Indeed , for a given solvent, the mass flux appears to be proportional to neither to P_G nor $P_G - P_{atm}$ but $P_G - P_0$ with $P_0 > P_{atm}$ and distinct for each solvent. These results argue that the hypothesis of the bubble acting as a gas exchanger (CO_2 out, N_2 and O_2 in)

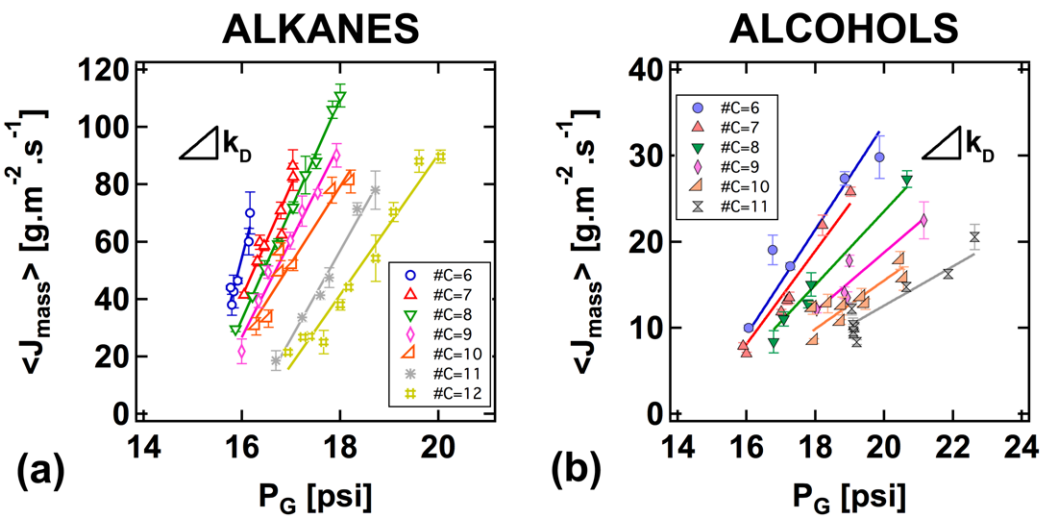

FIG. 3.10: CO_2 Mass flux vs. the gas injection pressure for alkanes (a) and alcohols (b). The slope of the fit for a same solvent gives an approximation of the dissolution coefficient k_D.

during the early regime is sound. Let us first consider the fact that nitrogen is much less soluble in alcohols than in the alkanes by a factor of about a hundred [140], which signifies that there is much less nitrogen in alcohols than in alkanes. This means that alkanes are much more susceptible to transfer N_2 to the bubble while CO_2 is dissolved from the bubble to the solvent. This behavior consequently affects the mass flux we measure at the interface, as we do not measure only the transfer of several species through the interface.It seems that the microbubble acts as an efficient gas exchanger, both releasing CO_2 (that dissolves in the surrounding liquid) and receiving nitrogen and oxygen (species dissolved in the liquids, stored at atmospheric pressure). As a result, the solvent effectively behaves as initially saturated with CO_2 at a pressure P_0. The higher solubility of N_2 in alkanes compared to alcohols thus explains why our experimental result $(P_0)_{alkanes} > (P_0)_{alcohols} \approx P_{atm}$.

The fact that P_0 increases with increasing molecular weight for the alkanes also follow this hypothesis, since nitrogen is much more soluble in dodecane than in hexane.

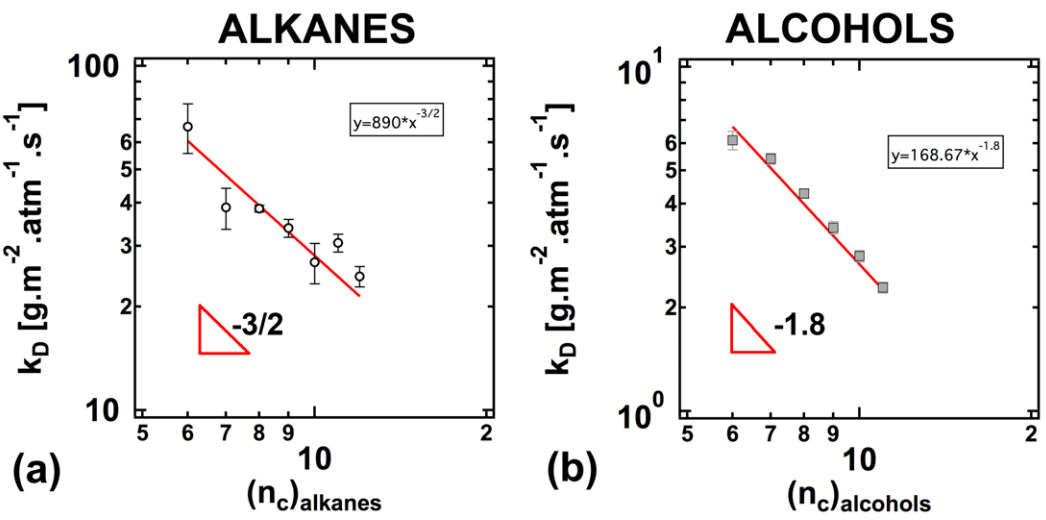

FIG. 3.11: Coefficient of dissolution k_D for alkanes (a) and alcohols (b) as a function of the length of their carbon chain.

3.3.4 The dissolution coefficient k_D

The dissolution coefficient associated with the transfer of CO_2 in a solvent can be approximated by calculating the slope of the mass flux versus the gas injection pressure (see figure 3.11). An interesting result is that the coefficient $k_D \approx k_L/k_H$ is independent of the flow conditions other than the gas injection pressure. This result suggests that a stagnant film model (see section 1.5.2) describes accurately the dynamics of the mass exchange through the caps, since other models depend on a time scale dependent on the flow conditions (e.g. the rate of fluid replacement).

The dissolution coefficient k_D associated with a solvent is plotted as a function of the length of the carbon chain in the solvent figure 3.11. For both alkanes and alcohols, k_D decreases with n_c, meaning that at similar pressure, the dissolution of CO_2 is more effective in low molecular mass solvents than in large. This result can seem surprising, as CO_2 is typically more soluble in large n_c solvents, but this consideration is flawed as it only takes into account the system at equilibrium. The dissolution coefficient on the other hand also takes into account the dynamics at which the system reaches equilibrium.

We now consider the dependence $k_D = k_L/k_H$ for alcohols. In figure 3.12,

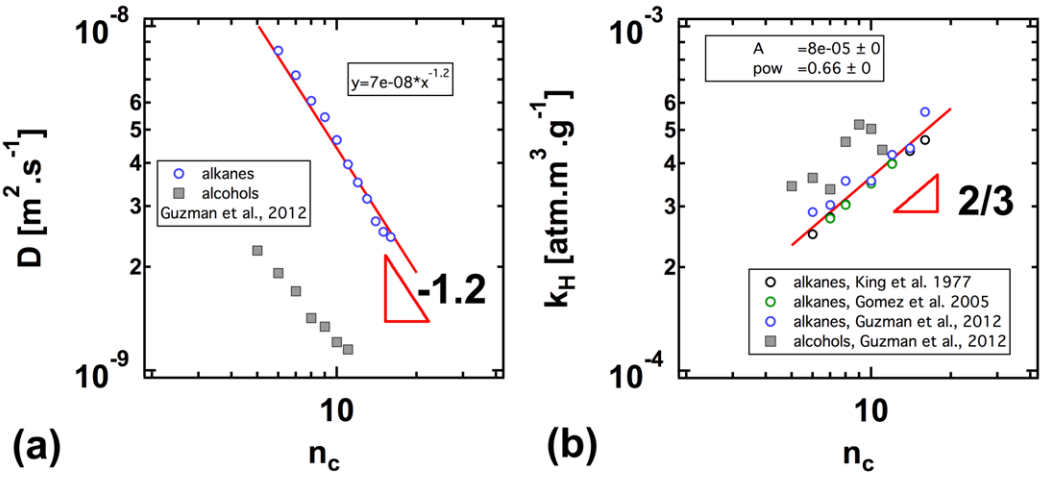

FIG. 3.12: Reported values[141–143] for the coefficient of diffusion and Henry's constant for the system CO_2/alcohols and CO_2/alkanes. The values are plotted as a function of the solvent carbon chain length.

experimental values [141–143] of the coefficient of diffusion D and Henry's constants k_H for the systems CO_2/alcohols are plotted as a function of the length of the carbon chain of the solvent. Since our results suggest that the stagnant film model is appropriate here, we have $k_L \sim D$. The literature values exhibit a behavior $D \sim n_c^{-1.2}$, leading to $k_L \sim n_c^{-1.2}$. Moreover, the data obtained by Guzman et al. show $k_H \sim n_c^{2/3}$. Combining the result, we get $k_D \sim n_c^{-1.86}$, very close to the $k_D \sim n_c^{-1.8}$ we obtained experimentally. This rapid scaling analysis suggest the possibility to obtain some correlation for the dissolution solely based on the fluids physicochemical properties. This topic will be expanded section 4.4.

3.3.5 Conclusions

In this section we investigated the microfluidic dissolution of a pure CO_2 gaseous phase in alcohols (n_c from 6 to 11) and alkanes (n_c from 6 to 12) just after bubble generation. The dissolution is assumed to take place only through the bubbles caps, and we compute the instantaneous mass flux from the bubble to the liquid by tracking the reduction in bubble's axial length.

Within our ROI of length $10w$ after the hydrodynamic junction, the mass flux is shown to be constant, suggesting that we observe an early, fast dissolution regime during which the solvent is far from saturation.

The value of the mass flux is then compared to the gas injection pressure and is successfully qualitatively compared to our model if the adsorption of species from the liquid to the bubble is taken into account. The bubble behaves as a gas exchanger and we have $J_{mass} \propto P_G - P_0$, where P_0 increases for increasing desorption from the liquid to the bubble. By considering that the mass exchange occurs as if the bubble dissolves itself in a solvent with a partial pressure of CO_2 P_0, we obtain values k_D: $J_{mass} \approx k_D(P_G - P_0)$. The dissolution coefficient k_D is independent of the gas flow conditions other than the gas injection pressure P_G, which suggest that a stagnant film model describes accurately the dynamics of the mass exchange through the caps.

A rapid scaling analysis suggest the possibility to obtain some correlation for the dissolution solely based on the fluids physicochemical properties.

We failed to modify our model to take into account the desorption of nitrogen and oxygen from the solvent to the bubble as a 2-species mass exchange across an interface is a complex problem lacking a simple analytical description.

Chapter 4

Early microfluidic dissolution of CO_2 bubbles in viscous oils

The content of this section is adapted from a paper published in Physical Review E as a rapid communication [43].

4.1 Overview

The dissolution of gas in liquid is a physicochemical phenomenon essential to life and the environment. Many natural and industrial flow processes depend on the rate of absorption and desorption of carbon dioxide gas in various fluids, including respiration [144], air-ocean interactions [145], effusive and explosive volcanic eruptions [146], advanced oil recovery [147], and polymer synthesis [148]. Better understanding the dynamics of dissolving bubbles in microgeometries is also important for the development of methods for the efficient capture of greenhouse gases in porouslike media.

In this section, we scrutinize the initial dissolution of CO_2 bubbles within viscous silicone oils under various microflow conditions. Periodic and monodisperse trains of bubbles are generated at a focusing section and the bubble shape is monitored during forced convection mass transfer to study the relationship between dissolution dynamics and oil molecular weight.

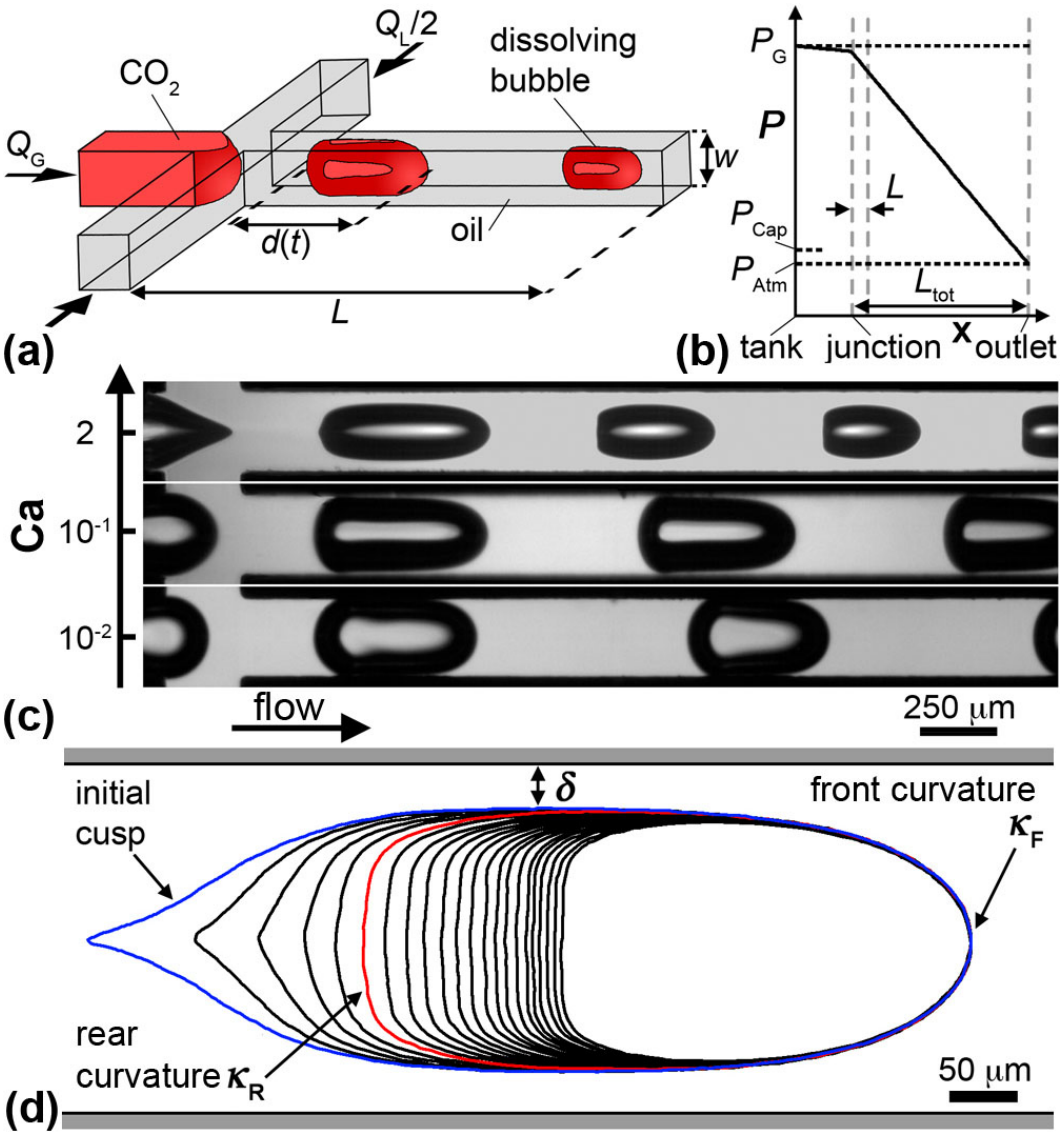

FIG. 4.1: (a) Schematics of the microfluidic contactor. (b) Sketch of the typical pressure P along the central channel with $L \ll L_{tot}$ and $P \sim P_G$ near the fluid junction. (c)Micrographs of flow patterns with similar initial bubble size $d_0/w \approx 2.25$, flow rates in $\mu L/min$, and viscosity in cS: $Ca \approx 2$ ($Q_L = 6$, $Q_G = 25$, and $\nu = 10^4$), $Ca \approx 10^{-1}$ ($Q_L = 380$, $Q_G = 341$, and $\nu = 10$), and $Ca \approx 10^{-2}$ ($Q_L = 800$, $Q_G = 670$, and $\nu = 1$). (d) Time series of bubble contour in the reference frame of the bubble front for $Ca \approx 2$ ($\Delta t = 12$ ms) [43]

4.2 Experimental conditions

The experimental set-up is similar to the one presented in the low viscosity section.

We focus on early bubble dynamics near the fluid junction over a distance $L \approx 10w$. Since the total length of our microfluidic network $L_{tot} \approx 100w$ is large, the hydrodynamic resistance of pure gas flow is negligible in the inlet channel and the typical capillary pressure is small $P_{cap} \sim 4\gamma/w \approx 3 \times 10^{-3}$ atm, we neglect both frictional pressure drop and capillary pressure effects in our region of interest (ROI) and use P_G as a control parameter for the bubble pressure (figure 4.1(b)).

The test liquids are conventional polydimethylsiloxane oils with a kinematic viscosity ν ranging between 1 and 10^4 cS. Silicone oil is useful for investigating viscous flow phenomena since its viscosity depends on molecular weight M while other properties, such as density and surface tension, remain nearly constant. The wide range of viscosities probed, however, introduces large differences in flow rates and pressure for each fluid pair investigated. Indeed, assuming that the multiphase flow pressure drop $\Delta P = P_G - P_{atm}$ is essentially dominated by the large dynamic oil viscosity η according to $\Delta P = c\eta(Q_L + Q_G)L_{tot}/w^4$ with geometrical constant $c \approx 28.45$ [77, 149], large flow rates are obtained with small pressure using low-viscosity oils and small flow rates are produced with large inlet pressure using high-viscosity oils. Nonetheless, our versatile fluid injection method and image acquisition system permit a systematic investigation of multiphase flows with both Q_L and Q_G varying between 10 and 10^3 μL/min and P_G between 1 and 5 atm. Accordingly, the typical bubble residence time $\tau \approx Lw^2/(Q_L + Q_G)$ in the ROI ranges between 1 and 10^3 ms.

Due to significant gas absorption, bubbles display a reduction in size during transport. To decorrelate dissolution from convection, we adopt a Langrangian approach [150] and track individual bubbles to digitally extract their contours as a function of time and location using custom-made IMAGEJ scripts and MATLAB codes. Contours are then superposed onto a composite image for inspection. To visualize bubble deformation, it is convenient to align time-

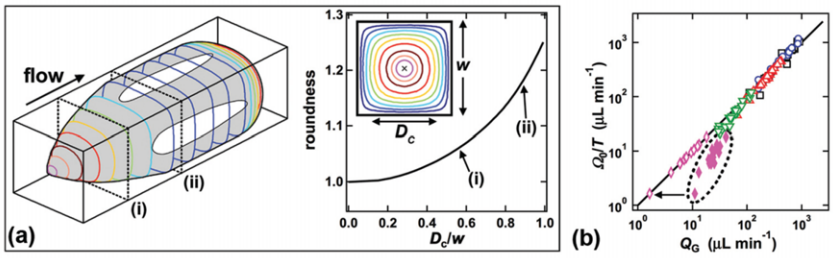

FIG. 4.2: (a) Schematics of volume reconstruction method using the roundness r of velocity contour plots of a single viscous flow in a square duct to calculate the geometrical parameters of each bubble slice. (b) Comparison between local gas flow rate Ω_0/T and the inlet gas flow rate Q_G . Small flow rates Q_G associated with highly viscous oil are calibrated using the local flow rate (arrow). The solid line denotes $\Omega_0/T = Q_G$, with oil viscosity ν = 1 (□), 10 (○),10^2 (△), 10^3 (▽), and 10^4 cS (◊) [43]

series contours with the bubble front (figure 4.1(d)).

4.3 Bubble volume reconstruction

For low Ca flows, elongated bubbles suffer a longitudinal shrinking while front and rear curvatures are set with the channel geometry. In the high Ca case, the very viscous fluid acts as a sheath material and strongly confines bubbles to Stokes flow in a square duct.

To measure the mass diffusion flux during dissolution, it is important to determine the instantaneous bubble volume $\Omega(x,t)$ and interfacial area $A(x,t)$. To this end, we use our two dimensional contours to reconstruct three-dimensional bubble shapes. We assume the profile in the third dimension conforms to the contour plots of the velocity field of a single laminar flow in a square channel. Longitudinally slicing bubbles in pixel-wide "disks" of diameter D_c allows us to estimate their area A_c using the roundness parameter $r = 4A_c/(\pi D_c^2)$ of the associated contour plot of the velocity field circumscribing the bubbles (figure 4.2(a)). The bubble volume $\Omega(x,t)$ is then simply calculated by summing individual areas A_c over the length of the bubble. Similarly, the bubble interfacial area $A(x,t)$ is computed by adding the perimeters of the disks associated with purely viscous flows. We validate our bubble volume

calculation method by comparing the inlet gas flow rate Q_G with its in situ counterpart measurement Ω_0/T, where Ω_0 is the initial volume of the bubble after breakup and T is the period of the bubble formation (figure 4.2(b)). The calculated volume of deformed viscous bubbles (e.g ., $\nu = 10^2$ and 10^3 cS) is in agreement with the input parameter. We note, however, a significant discrepancy between the two measurements for the highly viscous situation ($\nu = 10^4$ cS). The very small gas flow rate produced in this case falls into the lower range of the flow meter operating conditions (for Q_G below $\sim 30\mu$L / min), which systematically overestimates Q_G . In this case, we use the local flow rate measurement Ω_0/T as a reference to compute the actual gas flow rate Q_G .

4.4 Bubble dissolution

For every flow condition, the instantaneous bubble length d, interfacial area A, and volume Ω are computed by digitally processing high-speed movies (figure 4.3). To solely focus on gas dissolution effects, the time is set to zero when the bubble rear is at a distance w from the junction. This method allows for alleviating complex shape effects due to breakup with the presence of quickly damped surface waves for low Ca and rapidly receding rear cusps for large Ca. This approach results in no more than 15% truncation of the total bubble residence time in the ROI. Following this operation, two general trends are apparent. At low Ca, bubble shape parameters decrease steadily, while at high Ca, parameters first exhibit a steady decrease before slowly stabilizing for longer times.

The temporal evolution of bubble shape at a given pressure P_G allows us to measure the net mass flux according to

$$J = \rho_{CO2} \frac{1}{A} \frac{d(\Omega_0 - \Omega(t))}{dt} \tag{4.1}$$

where $\rho_{CO2} = \rho_0 P_G / P_{atm}$ and ρ_0 is the standard density of CO_2. Mass transfer operations are often described using a liquid mass transfer coefficient k_L to

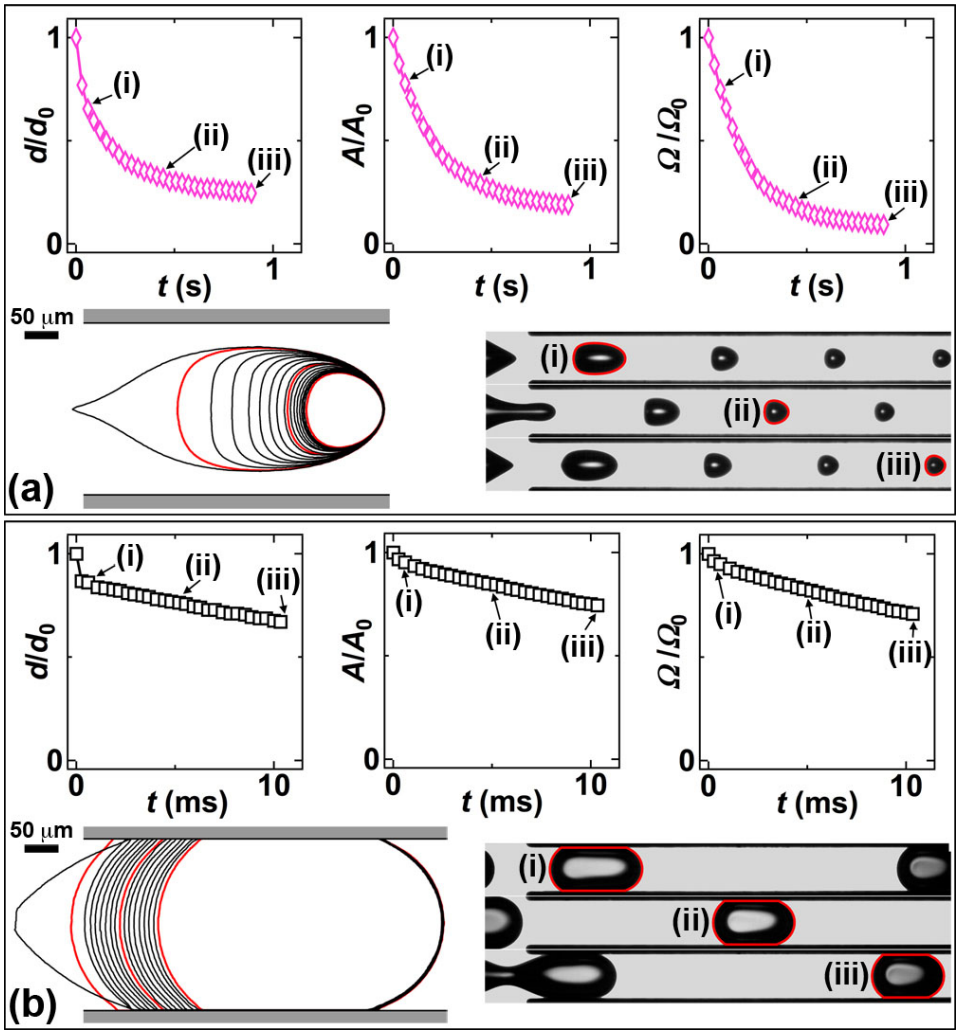

FIG. 4.3: Temporal evolution of the normalized bubble size d/d_0, interfacial area A/A_0, and volume Ω/Ω_0 in the ROI: (a) viscous regime, $Ca = 1.1$, $\nu = 10^4$ cS, and $P_G = 2.7$ atm and (b) capillary regime, $Ca = 9{\times}10^{-3}$, $\nu = 1$ cS, and $P_G = 1.03$ atm [43]

relate mass flux and variation of solute concentration

$$J = k_L \Delta C. \tag{4.2}$$

Here measurements of J at the bubble level are useful to examine the influence of flow and fluid properties on gas absorption in microgeometries. In the early dissolution regime, data show a linear temporal evolution of both the dissolution rate $W = \rho_{CO2} d(\Omega_0 - \Omega(t))/dt$ and the interfacial area A (figure 4.4(a)), which results in a steady mass flux J_0 before a sharp decrease for long residence times (figure 4.4(b)). The ensuing decline in J is attributed to a solute concentration in the bulk reaching near equilibrium with the interfacial concentration $\Delta C \sim 0$ and is referred to as saturation drop. This phenomenon is not observed for low-viscosity flows due to their short bubble residence times in the ROI. For each fluid pair, we calculate the early steady diffusive flux J_0 and find a linear relationship with pressure according to

$$J_0 = k_D \Delta P, \tag{4.3}$$

where $\Delta P = P_G - P_{atm}$ and k_D is the dissolution coefficient (figure 4.4(c)). This result can seem surprising as our model suggests that we would have $J_0 \propto P_G$(equation 3.14). Our experimental findings show that when the solvent is initially exposed to air, J_0 scales with the gage injection pressure ΔP. This fact suggests an exchange of species with absorption of carbon dioxide and desorption of previously dissolved nitrogen and oxygen molecules into the bubble. As a result, the solvent effectively behaves as initially saturated with CO_2 at atmospheric pressure. Overall, the coefficient k_D is a reliable parameter for characterizing the dissolution rate of given fluid pairs and it combines the two fundamentals of gas absorption, namely, saturation through k_H and the dynamics at which the system approaches equilibrium with k_L [82].

Liquid mass transfer rates k_L through a moving interface are typically determined using a penetration model with $k_L \sim (D/\tau_c^{1/2}$, where D is the diffusion coefficient and τ_c the liquid contact time, i.e., the convective time

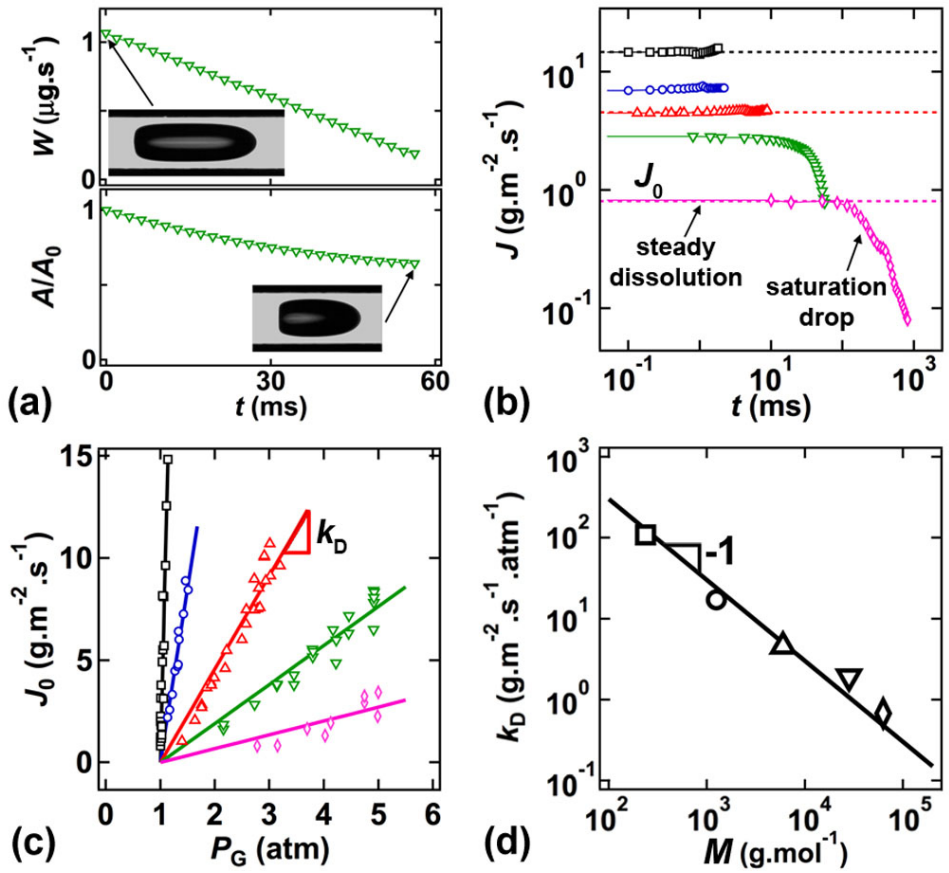

FIG. 4.4: Diffusive mass flux of CO_2 bubbles in silicone oils. (a) Example of evolution of diffusive mass flow rate Wand interfacial area A for $\nu = 10^3$ cS. (b) Examples of mass diffusion flux J with constant initial flux J_0 for various oils, ν = 1 (□), 10 (○),10^2 (△), 10^3 (▽), and 10^4 cS (◊). (c) Early flux J_0 versus pressure P_G for all fluid pairs. The solid lines denote $J_0 = k_D(P_G - P_{atm})$.(d) Dissolution coefficient k_D as a function of oil molecular weight M. The solid line denotes $k_D = 3 \times 10^4 M$ [43]

scale [52]. By contrast, in the case of a stagnant film, only molecular flux is considered and Fick's first law yields $k_L \sim D/\epsilon$, where ϵ is the concentration thickness. A cylindrical bubble in a square channel combines equivalents of both moving and stagnant liquid-gas mass transfer surfaces with (a) the sides in contact with the liquid film near the walls and (b) the end caps. Previous work in the capillary regime showed that dissolution primarily occurs through bubble end caps [41]. This situation is analogous to the stagnant film model since gas is transferred into reservoirs of liquid traveling along with bubbles. Recirculation motion in such liquid plugs tends to homogenize bulk concentration C_{oil} and confines solute concentration variations to a thin liquid boundary layer of thickness ϵ at the transfer surface.

For the CO_2/silicone oil fluid pairs, the dissolution dynamics strongly depend on the oil molecular structure.We express the oil viscosity η as a function of molecular weight M and k_D is found to steadily decrease with M according to $k_D \approx aM^{-1}$, with the prefactor $a = 3 \times 10^4$ g^2/(mol.m^2.s.atm) (figure 4.4(d)). As the concentration thickness is expected to be proportional to the polymer hydrodynamic radius $\epsilon \sim M^{1/2}$, our finding for k_D suggests that

$$D/k_H \sim M^{-1/2} \tag{4.4}$$

According to the theory of the diffusion of polymer, diffusivity depends on polymer concentration and molecular interactions and ranges between $D \sim M^{-1/2}$ for a dilute solution of polymer in a low-viscosity solvent and $D \sim M^{-2}$ for self-diffusion in an undiluted polymer [52]. In particular, if hydrodynamic interactions between individual polymers are neglected, theory predicts $D \sim M^{-1}$. Assuming such scaling for D yields a dependence for the Henry constant such as $k_H \sim M^{-1/2}$ and implies that carbon dioxide solubility $C_i \sim k_H^{-1}$ weakly increases with the polymer molecular weight M. These arguments illustrate the complexity in relating dissolution dynamics to fluid properties since models used for k_L, ϵ, and D strongly affect results for solubility. From a practical standpoint, the determination of k_D for a given liquid-gas pair provides a more reliable and direct estimate of gas impregnation dynamics.

4.5 Conclusions and Prospects

In this study, we analyze the morphology of dissolving carbon dioxide bubbles in oils from low to large capillary numbers and we extract the initial steady mass transfer flux during gas absorption. We show that the dissolution mass transfer coefficient k_D is a practical parameter to quantify diffusive multiphase flow phenomena in microgeometries. In particular, its systematic characterization is useful for comparing data with forced-convection mass transfer processes and fluid properties models. Further developments should consider the influence of gas exchange on partial pressure balance inside bubbles, as well as polymer swelling [151] and potential modification of diffusion and solubility coefficients during absorption [152]. Theoretical and numerical investigations would provide insights into the factors affecting microfluidic dissolution processes. This study is promising for the development of high-viscosity fluid microflow contactors and for better characterizing gas dissolution processes in complex fluids using microfluidic passages.

An interesting study would be to use a slightly longer ROI in order to observe the saturation drop after the early dissolution regime observed figure 4.4. By measuring the solvent concentration at which the saturation drop occurs, one could identify a maximal concentration value after which the solvent is effectively undiluted. This would allow to quantify our assertion that the early dissolution regime happens until the solvent concentration is no longer negligible.

4.6 Gaseous CO_2 exchange in altered silicone oils

A solution to get a better understanding of the gases exchange occurring within the bubble (see section 3.3.3 for instance) is to alter the species concentration within the liquid constituting the continuous phase. There are then two possibilities, either to enrich the liquid or to degas it. Both options were attempted, and enriching the liquid emerged as the easiest solution to imple-

ment in our lab. Using a simple in-house set-up (see figure 4.5(a)), we were able to enrich the liquid within a syringe itself. The syringe is placed on a vertical syringe pump and is connected with a the gas tank of CO_2 at a pressure P_e controlled using a miniature pressure regulator and measured with a pressure sensor embedded along the feeding line. CO_2 bubbles then dissolve in the syringe and the pressure increases within the syringe until reaching apparent equilibrium (i.e. when no more bubble appear in the liquid being enriched), the syringe pump keeping the syringe closed. The syringe is also turned several times around to ensure good mixing. The partial pressure of CO_2 within the liquid is then around P_e. This syringe is then directly used to inject the liquid within the chip by simply turning on the syringe pump, therefore allowing us to be reasonably certain of the partial pressure of CO_2 within the liquid flowing in the microchannel (since the syringe is never let at atmospheric pressure).

The dramatic growth of a CO_2 bubble in an enriched viscous silicone oil can be seen figure 4.5(b). We now try to explain this behavior. Assuming that there was total equilibrium between the CO_2 injected from the tank within the syringe before injecting the solvent, the initial concentration of CO_2 in the oil is given by

$$C_{0,L} = \frac{P_e}{k_H}, \tag{4.5}$$

where P_e is the enrichment pressure (i.e. the tank pressure fed into the syringe prior to the experiment) and k_H the Henry's constant associated with our fluid pair (CO_2/silicone oil).

The CO_2 mass concentration within the bubble, assuming a ideal gas behavior is given by:

$$C_{0,B} = \frac{MP_G}{RT}, \tag{4.6}$$

where M is the molar mass of CO_2(44g/mol), P_G [atm] the gas injection pressure, R [m^3.atm.K^{-1}.mol^{-1}] the ideal gas constant and T [K] the temperature of the system. Neglecting the presence of other species in the system (nitrogen and oxygen notably), there is initially a mass transfer from the liquid to the

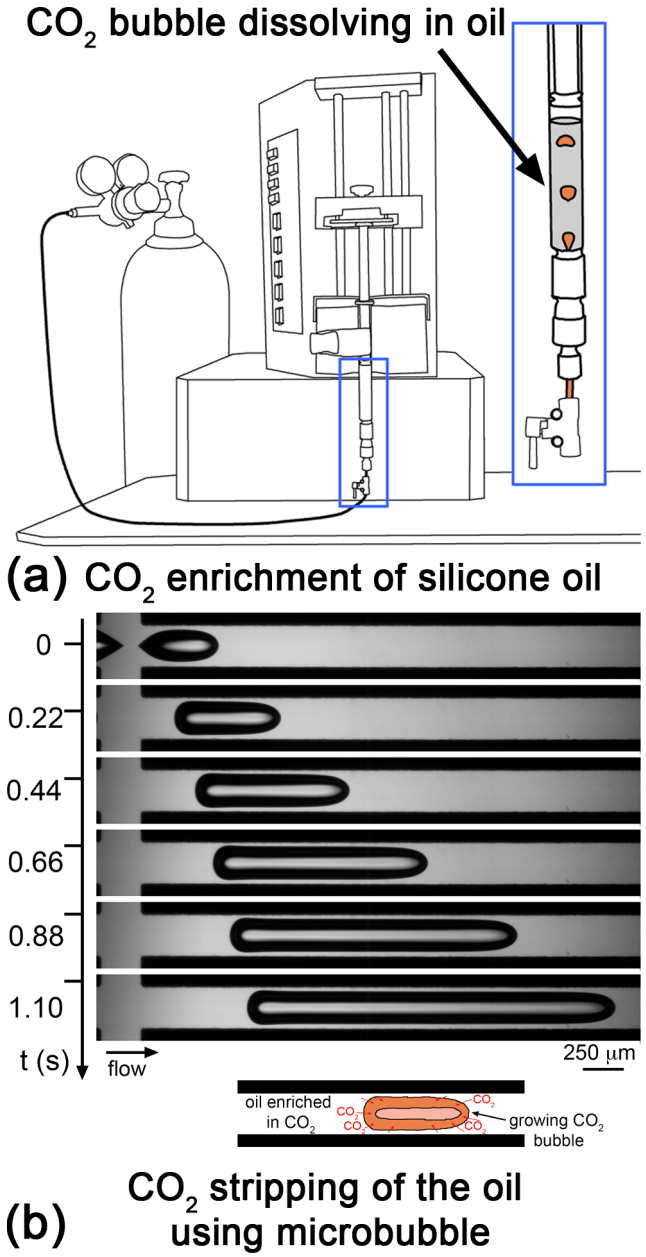

FIG. 4.5: (a) Method to enrich silicone oil. (b)Experimental micrographs showing the growth of a CO_2 bubble as a function of time. The pressure within the bubble is estimated at $2.1atm$ while the continuous phase is a 10^4 cS silicone oil previously enriched with CO_2 at $4.7atm$.

bubble if $C_{0,L} > C_{0,B}$, i.e. if

$$P_e > \frac{Mk_H}{RT} P_G. \tag{4.7}$$

Here we lack accurate values for k_H, but according to the silicone oil manufacturer (Gelest, inc), the solubility of gases in the oils does not vary significantly for oils with viscosities greater than 10cS and is equal to $k_H \approx 5.63 \times 10^{-4}$atm.m^3.g^{-1}. According to this value, we thus have gas exchange from the liquid to the bubble if

$$P_e > 1.01 P_G. \tag{4.8}$$

There is therefore stripping of the CO_2 from the silicone oil if the oil partial pressure in the liquid is higher than the gas injection pressure. This explains the consequent CO_2 sparging when P_e is much higher than P_G as depicted in the example of figure 4.5(b).

While such a growth can be explained by the transfer of dissolved CO_2 from the oil to the bubble, the same experiment with an air bubble displays a much more limited expansion. This experimental finding is unexpected, as the CO_2 gradient is stronger in the case of the air bubble and should result in a more intense gas exchange. This suggests that several complex mechanisms simultaneously occur at the bubble's interface (the bubble certainly acts as a gas exchanger). However, this phenomena needs to be more systematically observed before making any conclusions.

Chapter 5

Microbubbles in confined viscous environments

An important step towards a more widespread usage of microfluidic methods resides in the ability to control and predict the flow behaviors as a function of parameters such as the geometry and size of microfluidic devices, fluids flow rates and properties. We have seen previously that depending on these parameters, distinct flow regimes can be observed (see section 1.3.6), and we focus in this chapter on the characteristics of the segmented regime. The popular geometries of the production of bubbles or droplets in the regime are flow-focusing devices, T-junctions and co-flowing devices. In recent years, the formation of bubbles in microgeometries has been widely applied in various fields such as in materials synthesis [153, 154], encapsulation [155], chemical mixing and reaction [28, 156], all based on the ability to generate a highly uniform disperse phase in a continuous manner (e.g. [157]). Contrary to flows in conventional devices, the laminar flow in microchannels allows for an extensive control both in space and time of the fluid-fluid interface, permitting the relatively easy generation and control of periodic monodisperse bubbles or droplets.

However, the bubble formation mechanisms at the microscale are still not established, as can suggest the literature on the subject over the last few years [73, 77, 136, 158, 159]. Currently, there is not a unifying picture of the bubble

formation at the microscale: the equations predicting the flow characteristics (bubble size, spacing between bubbles, frequency,...) are geometry-specific and usually valid for a limited flow range.
In the first section of this chapter, we focus on the formation of bubbles in flow-focusing devices, emphasizing on the impact of the liquid viscosity. We will compare our experimental results to current models and present a unifying scaling law valid for a wide range of capillary number.
In the second section of this chapter, we tackle the morphology of the flow once the bubbles reach a steady shape, once again focusing on the impact of the capillary number on the flow structure.

5.1 Flow in complex microgeometries

The displacement of gaseous bubbles in a liquid through capillaries of constant cross section is of fundamental importance as it is used as a model in many engineering and natural processes. Such prototypical multiphase flows have been extensively studied using a theoretical approach, numerical tools and experiments.
However, the convoluted paths in rock pores, packed beds and lung bronchiole are much more complex than a single channel with a circular or rectangular base. To incorporate this aspect into prototype pore scale models, researchers have used periodically constricted geometries, as they produce flow fields that are partially extensional and unsteady in the Lagrangian sense [160, 161]. Both characteristics are expected to play a fundamental role to model multiphase flows at the pore scale.

5.1.1 A Gallery of Fluid Motion

The content of this subsection is adapted from a paper that will be published in Physics of Fluids in September 2014. The associated poster won the Gallery of Fluid Motion Award at the 66^{th} Annual Meeting of the APS DFD. The general structure of the flow is depicted figure 5.1 and some of the most striking images are compiled in figure 5.2, while the flows with no contact

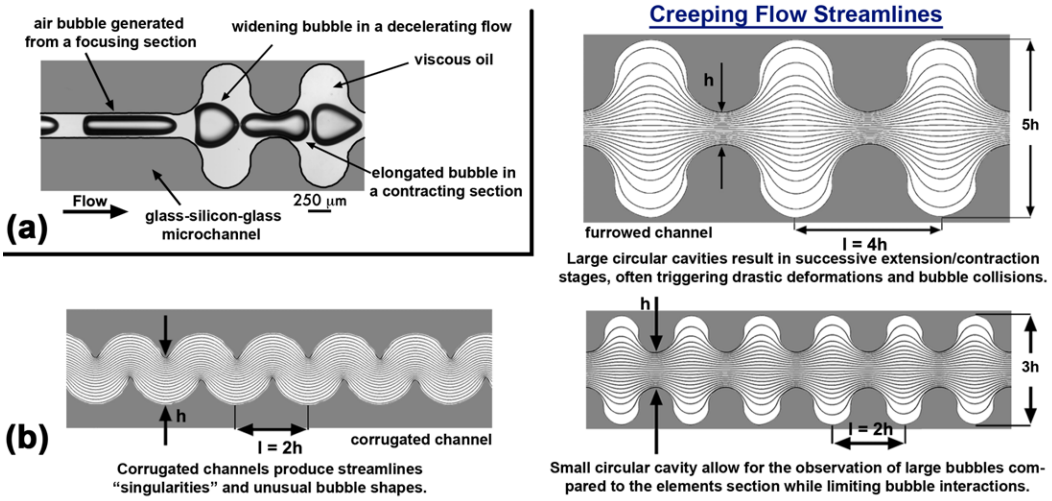

FIG. 5.1: (a) Entrance of a bubble train in the furrowed section of the microchannel. (b) Creeping flow streamlines obtained using COMSOL for each geometry investigated.

between the bubbles are tackled in next subsection.

Multiphase flows in confined geometries can exhibit a variety of intriguing morphologies. At the small scale, the unique balance of forces produces flow patterns that are typically governed by viscous and capillary effects. While surface tension tends to minimize interfacial area with bubbles having spherical shape, viscous laminar flows can also strongly deform bubbles in velocity fields set with the channel geometry.

Here, the deformation of capillary surfaces is accentuated with the use of a highly viscous carrier fluid (viscosity: 1,000 cS) and the presence of circular cavities along a square microchannel ($h = 250$ μm) for smoothly modulating flow velocity. In such viscous-dominated regime, air bubbles adopt a range of shapes depending on their size and packing. In particular, when passing through a series of extensions and constrictions, bubbles are observed to strongly elongate in accelerating flow regions and widen in decelerating flow fields. These experiments illustrate the possibility to control the flow morphology of microbubbles through the interplay between channel geometry and viscous flow.

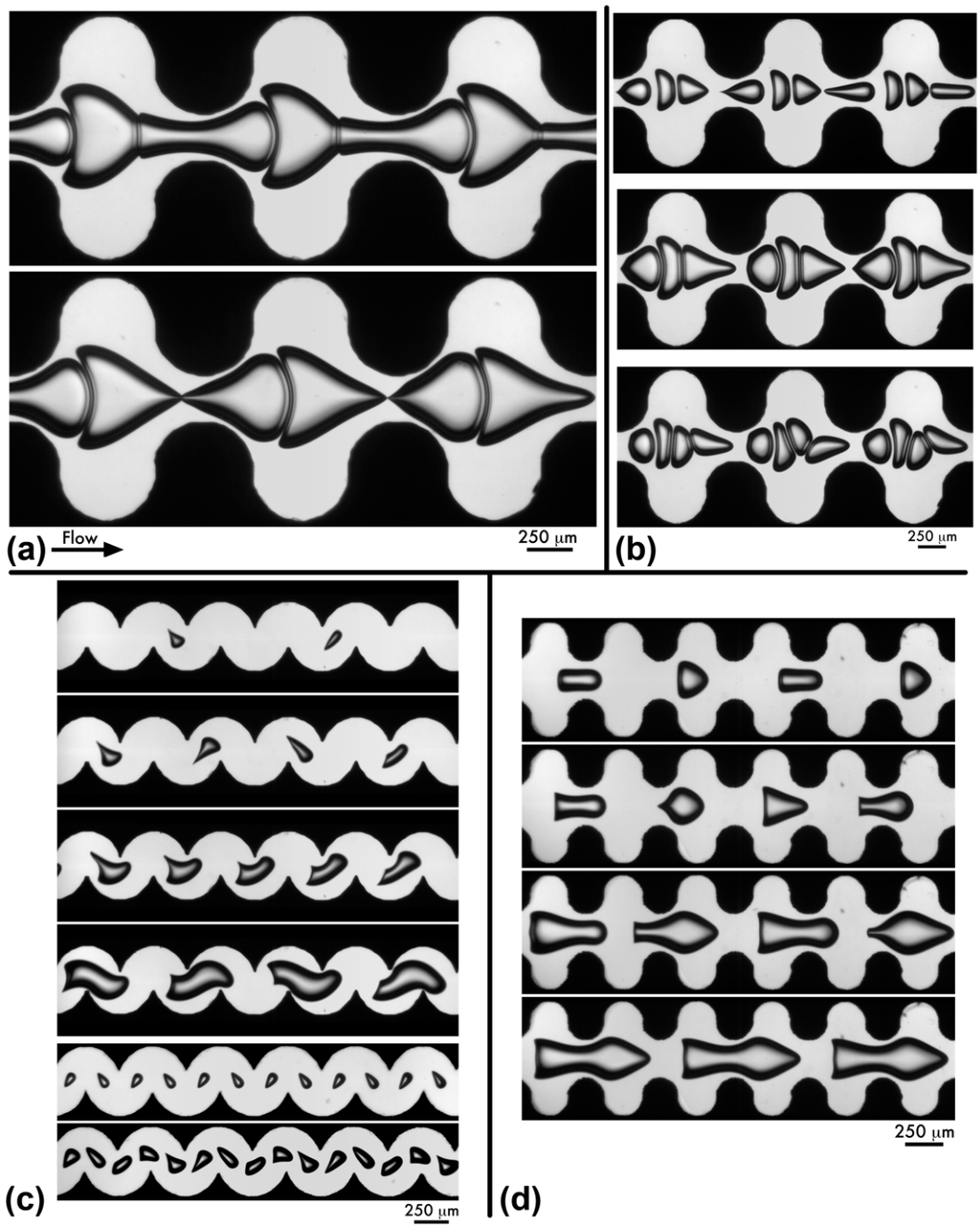

FIG. 5.2: (a) Time series of air bubbles in 1,000 cS oil at high capillary number, (b) Packing and arrangement of dissolving CO_2 bubbles. (c) Increase of the air volume fraction (from top to bottom). The two micrographs at the bottom show the possibility to generate denser patterns with dissolving CO_2 bubbles. (d) Increase of the air volume fraction (from top to bottom). As bubble increase in size they are subject to both extensional and contractive streamlines.

5.1.2 Investigation on the motion of non-colliding bubbles in furrowed microchannels

The displacement of gaseous bubbles in a liquid through constant capillaries is of fundamental importance as it is used as a model in many engineering and natural processes. Such prototypical multiphase flows have been extensively studied using a theoretical approach, numerical tools and experiments. However, the convoluted paths in rock pores, packed beds and lung bronchiole are much more complex than a single channel with a circular or rectangular base. To incorporate this aspect into prototype pore scale models, researchers have used periodically constricted geometries, as they produce flow fields that are partially extensional and unsteady in the Lagrangian sense [160, 161]. Both characteristics are expected to play a fundamental role to model multiphase flows at the pore scale.
Monodisperse CO_2 bubbles are periodically generated at the focusing section of the square channels ($h \approx 250\mu$m), with characteristics governed by the flow conditions. The bubble trains then travel downstream through a square channel before reaching a rectangular channel with a width that varies sinusoidally with the axial position x: $w(x) = h + (M - h)\sin(x\pi/\lambda)^2$, while the channel height is kept constant ($h(x) \approx 250\mu$m).

The bubbles undergo uniaxial extension in the contraction sections and biaxial expansion in the divergent sections of the channel and consequently the bubble speed and shape vary with the bubble's location. In order to understand the flow within such a micro channel, a 3D COMSOL simulation was performed (see figure 5.3) and gave very satisfying results when compared with experimental streamlines, detected by flowing glass beads in the channel. The simulation was intended to obtain results such as the evolution of the velocity in the center of the channel with the axial position in the case of a single phase flow, which will be used to analyze the data.

At small to moderate capillary numbers, the bubbles recover a nearly circular shape in the wide sections of the periodic tube. For large capillary number, the bubbles are constantly deformed. Using an image processing script, we are able to extract the bubbles shapes and velocity as they travel downstream

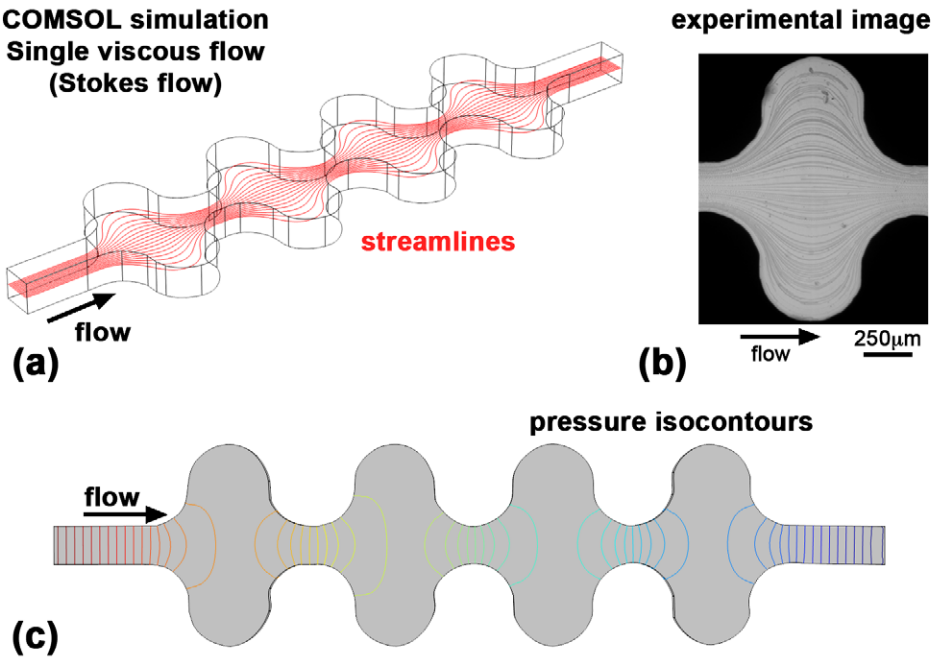

FIG. 5.3: 3D COMSOL simulation for a single phase flow. Simulations are following accurately the images obtained experimentally (b).

(see figure 5.5).

For flows in 10 cS oil, bubbles recover a nearly circular shape in the wide sections of the channels. For large capillary number, the bubbles are permanently deformed in traversing the narrow throat and do not recoil in the wide sections. The asymmetry of the bubble's motion (not the same shape when entering/exiting the contraction) is given by the evolution w_b/h_b as a function of the channel width at the bubble centroid w_{cd} (see figures 5.4 and 5.5). The asymmetry of the bubble motion appears to vary with $\mathrm{Ca}^{1/2}$ (see figure 5.6(a)), a surprising result as the viscous regime is usually associated with higher flow conformity.

A measure of the bubble deformation is given by

$$D_b = \frac{P^2}{4\pi A_b}, \tag{5.1}$$

where P and A_b are the bubble's apparent perimeter and area (see figure 5.4).

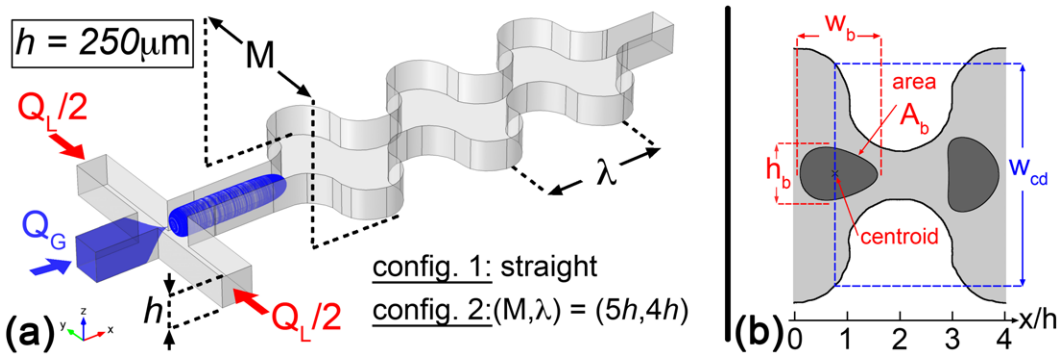

FIG. 5.4: (a)Channel geometry (b)Description parameters

Bubbles of similar size experience higher deformations when flowing through the high viscosity oil (figure 5.6(b)). Moreover, in the viscous regime, the averaged deformation does not depend solely on the bubble size but also in the associated capillary number. This demonstrates and quantifies the impact of viscous stresses on the bubble's motion.

Investigations are still underway to obtain a better understanding of the coupling of high viscosity flows with periodically constricted capillaries. Experimental data using a channel a less significant ratio M/H (see figure 5.7) need to be thoroughly analyzed to quantify the impact of the viscous stresses on the motion.

5.1.3 Bubble division in high viscosity oils using a Y-Shaped Microchannel

The use of high viscosity fluids as a continuous phase and the resulting high capillary flows have an untapped potential in terms of flow control.
When flowing bubbles through a channel splitting symmetrically in two, the bubbles will either flow through one or the other outlet. If the experiment has been carefully realized, one can obtain an alternative flow of bubbles: if one bubble goes to one of the outlet, then the following one will exit the junction through the other one. However, when the continuous phase is a viscous oil, one can easily reproduce the behavior displayed on figure 5.8: the bubble will split exactly in two equal bubbles. Such behavior could be scaled up to

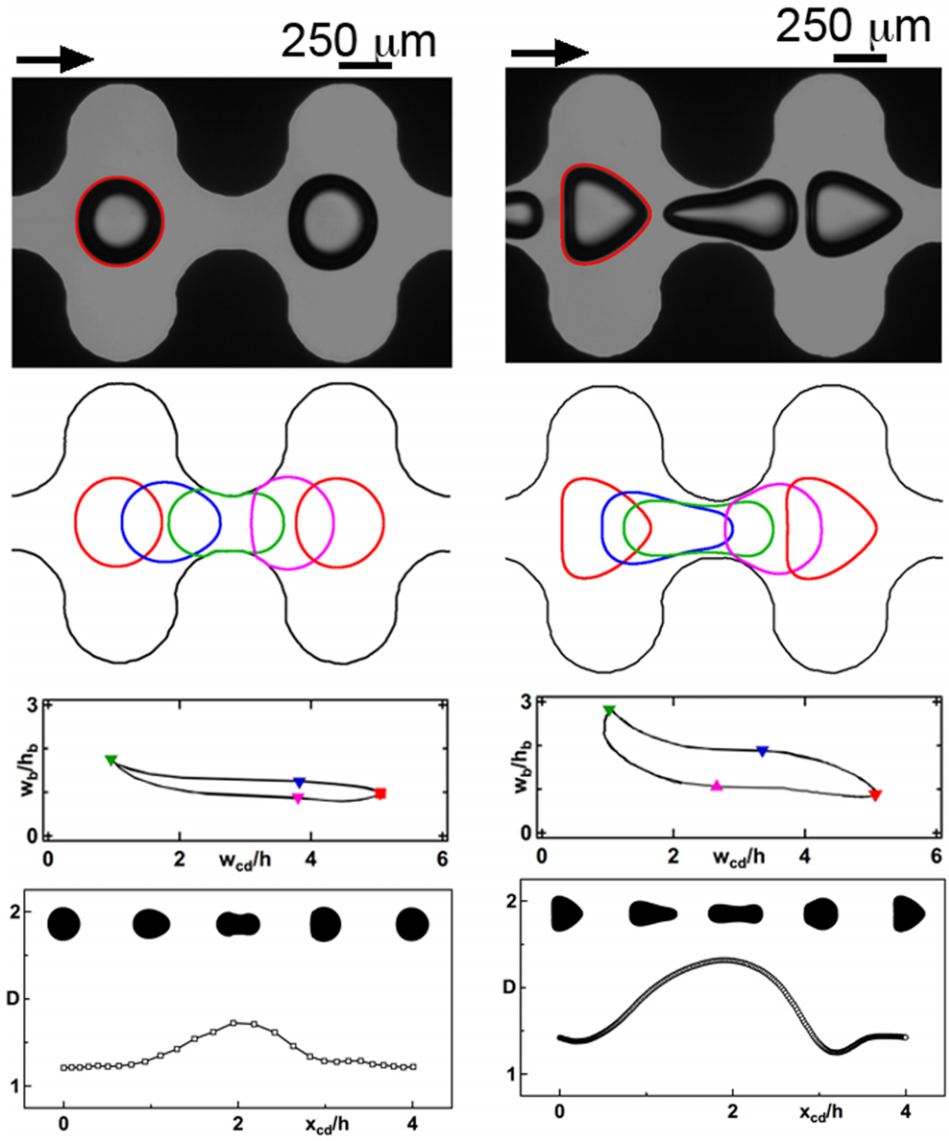

FIG. 5.5: CO_2ubble motion and deformations in 1 and 10^3 cS oils.

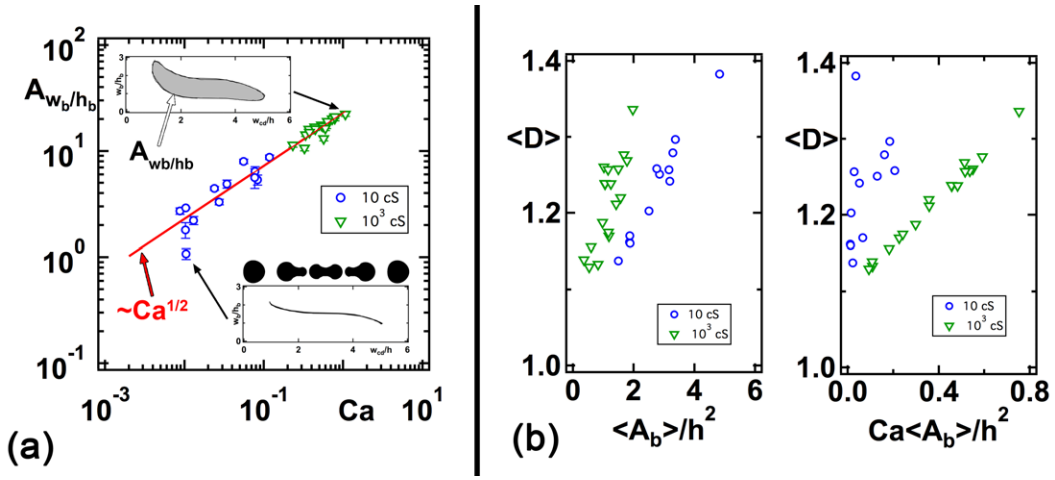

FIG. 5.6: (a) Asymmetry of bubble motion as a function of Ca. (b) Average deformation as a function of the capillary number and the bubble size.

produce smaller and smaller bubbles, depending on the number of Y-shaped junctions.

Another interesting situation is represented figure 5.8: the flow of a multiphase flow through an expanding chamber divided in three section effectively results in the obtention of a single phase enriched liquid through the side outlets and a multiphase flow through the central outlet.

5.1.4 Bubble arrangement in a diverging/converging microchannel

Trains of bubbles are formed by focusing streams of air and viscous silicone oil into a square micro channel ($w \approx 250\mu$m) that is connected to a diverging/converging slit microfluidic chamber. The flow rates necessary to obtain formations deemed interesting, and not only a train of bubble slowing down in the diverging section before accelerating in the converging section, are high. Because the formation of a structure in the chamber affects the bubble generation at the stream junction through a variation in flow rate and pressure, the flows were hardly stable. However, one can sometimes obtain "pseudo-organized" structures in the micro chamber (see figure 5.9). Even if transient and potentially unstable because of a possible coalescence cascade,

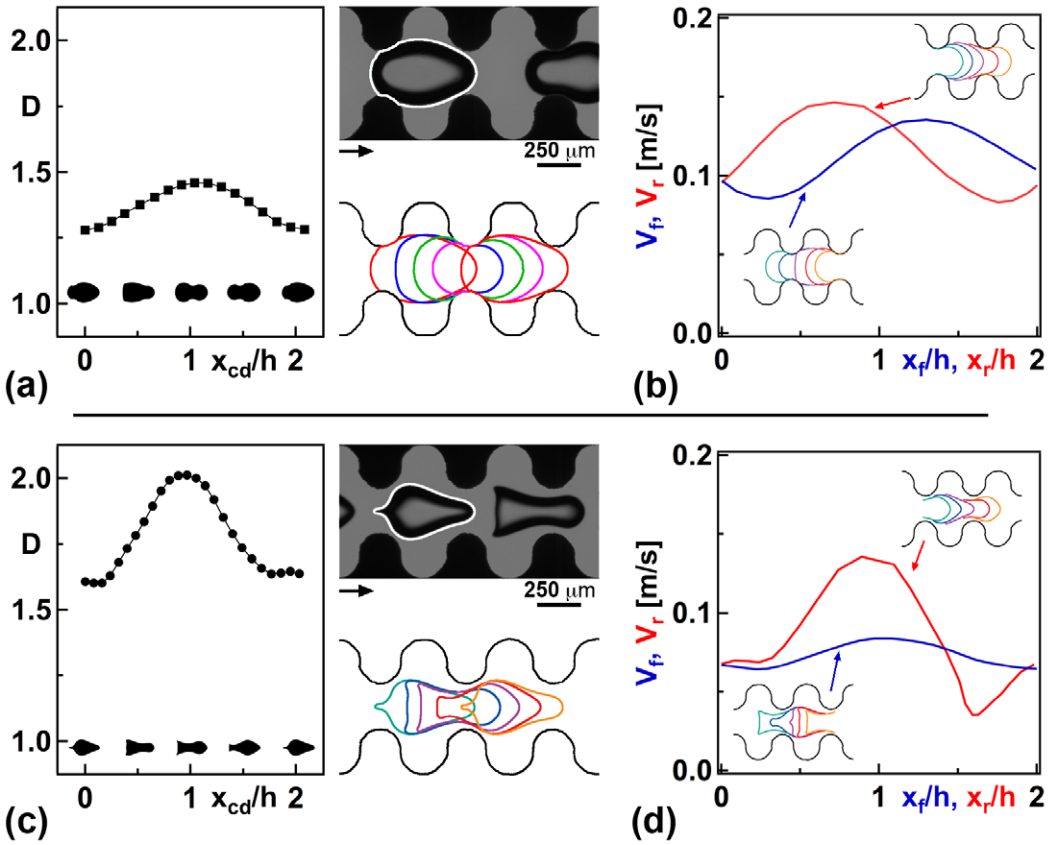

FIG. 5.7: Experimental data using a different microchannel with $M = 2$. Bubble deformation over a cycle for a bubble flow in (a) 1 cS and (b) 10^3 silicone oils. Front and rear bubble velocities as a function of the front and rear bubble coordinate for a bubble flowing in (a) 1 cS and (b) 10^3 silicone oils.

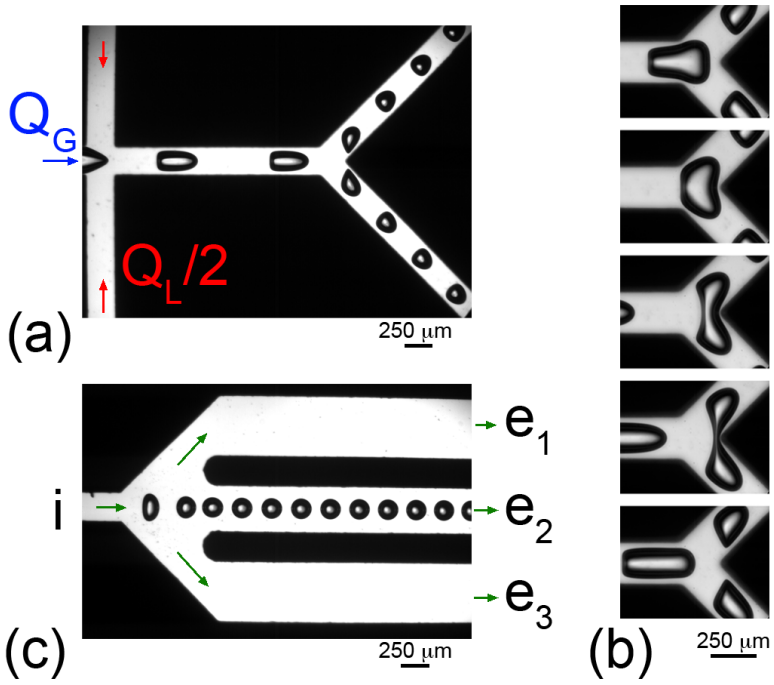

FIG. 5.8: (a)Bubble division using a Y-shaped channel in a high viscosity oil (b)Zoom on the bubble splitting in two (c)A geometry enabling to have a multi-phase flow flowing through inlet i and obtaining enriched liquid from outlets e_1 and e_3

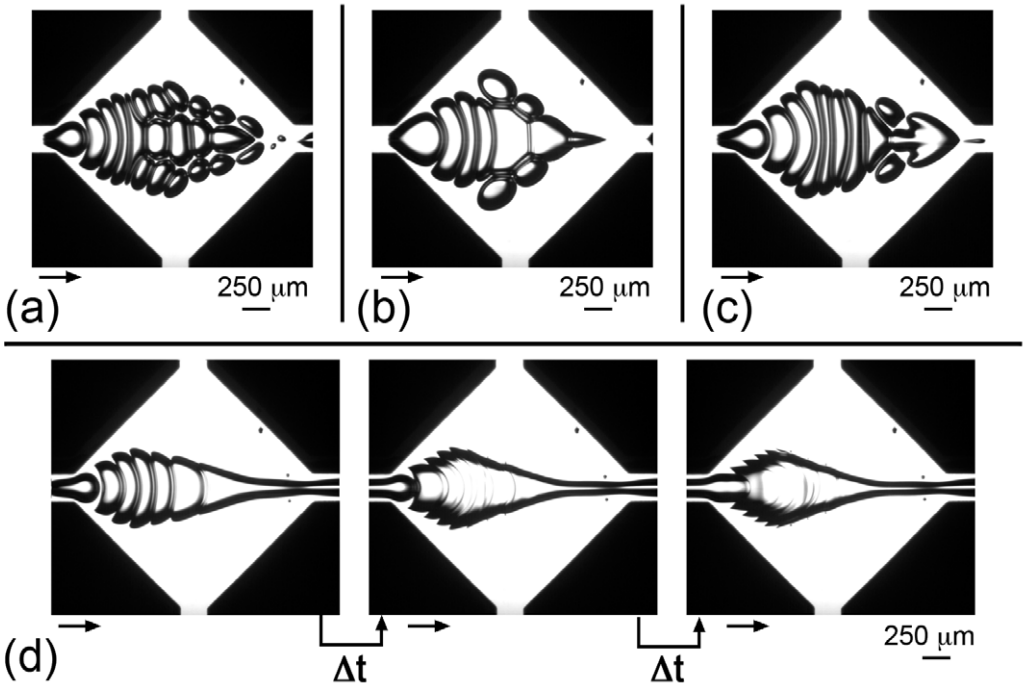

FIG. 5.9: Formation of complex structures when air bubbles flowing into viscous oil ($10^4 cS$) enter the microfluidic chamber. (a)Pseudo-organized structure (b) Time lapse of a catastrophic bubble coalescence, resulting in extreme air/oil interfaces

one can be amazed by the symmetry of these formations. Under the right conditions, we can even observe ultra-rapid catastrophic bubble coalescence, resulting in highly peculiar interface shapes.

5.2 Formation by hydrodynamic focusing at a cross shaped mixing section

In this section, we examine the fluids' dynamics leading to the generation of periodic mono disperse trains of bubbles at the hydrodynamic focusing section of a square micro channel ($h \approx 250\mu$m).

The mechanisms leading to bubble pinch-off in confined geometries at low capillary number have been extensively studied [73, 162, 163] and revealed that the collapse proceeds through a series of equilibria, each yielding the minimum interfacial energy of the fluid-fluid interface. The process is slow in comparison

to typical relaxation speeds of the interface, and it is reversible. Its quasistatic character of collapse forms the basis for controlled, high-throughput generation of monodisperse fluid dispersions.
The mechanisms leading to the generation of bubble trains in a high viscosity fluid have not been unraveled, and while some researchers have presented experimental data [159], we lack a precise description of the dynamics of the pinch-off at large capillary numbers. At low capillary numbers, the bubble formation is supposedly controlled by one of the two mechanisms: the squeezing mechanism or the shearing mechanism. Although both the squeezing mechanism and shearing mechanism for bubble formation could estimate well the bubble size in corresponding experiments, they have significant divergence on evaluating the role of liquid properties during bubble formation. The squeezing mechanism supports that the effect of the liquid viscosity on the bubble formation is negligible.

Overall, the understanding of liquid viscosity on the bubble formation in microfluidic devices remains obscure: the role of the liquid viscosity on the bubble formation is significant according to the shearing mechanism but it is negligible following the squeezing mechanism. This section aims to study the formation of air bubbles in silicone oils with a viscosity ranging from 1cS to 10^4 cS.

5.2.1 Time remaining before pinch off

We examine the fluids' dynamics leading to the generation of periodic monodisperse trains of bubbles at the hydrodynamic focusing section of a square microchannel (h =250μm).

Using a high-speed camera, we visualize the formation of bubbles at the focusing section. The frame rates being limited by the camera specs and the dimensions of the field of view, we are unable to record the bubble generation at frame rates higher than 10,000 frame per second.

Such frame rates are not sufficient to capture the details of the dynamics during the pinch off of the gaseous thread: at low viscosity, the bubble gener-

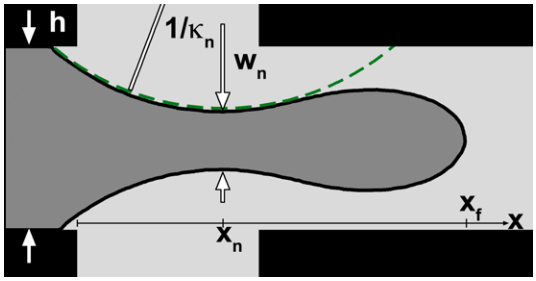

FIG. 5.10: Schematic of the interfacial contour and geometrical parameters of the axisymmetric gaseous neck.

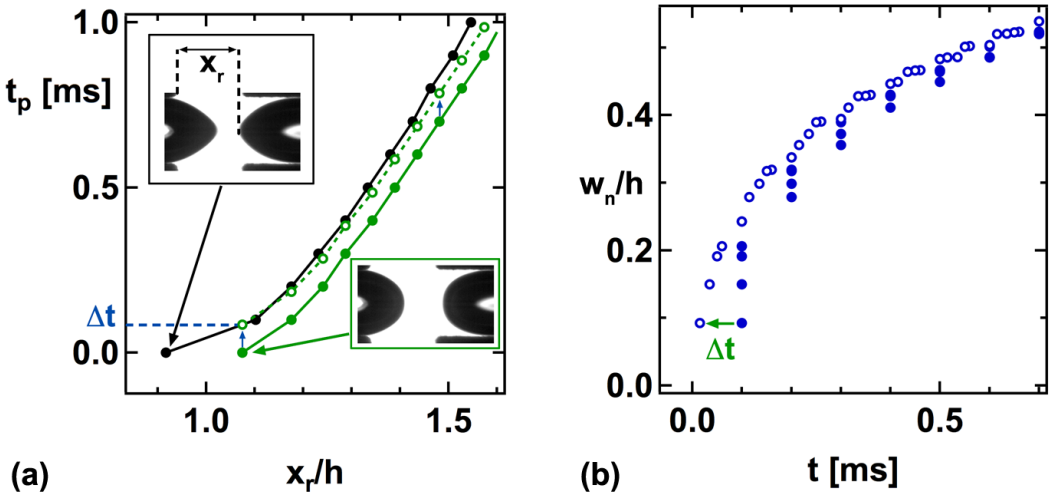

FIG. 5.11: (a) Evolution of the time after separation t_p vs. the x-coordinate of the rear of the bubble. The black curve is the reference curve for which $(x_r)_0)$ is minimum while the continuous green curve is a typical curve from the same data set. For each curve, $(t_p)_0$ is interpolated to be on the reference curve, consequently translating the whole curve by a value Δt (see dotted green curve). Assuming the velocity of the rear of the bubble to be constant in the first instants, it means that the first image of associated with the green curve happens not at $t = 0$ but at $t = \Delta t$. (b) Evolution of the thickness of the neck as a function of the measured (full dots) and interpolated (empty dots) remaining time until pinch-off. Note that because the associated frame rate is 10kfps, the measured data is obtained for $t = 0.1, 0.2, ...$

ation process sometimes takes less than 1 ms. However, the recording time is long compared to the bubble generation period: recordings typically capture at least a dozen bubble generations. We use the periodicity of the multiphase flow to extract additional information by estimating the time before break up for each sequence.

For a given image sequence, we plot the distance between the mixing section entrance and the bubble rear x_r as a function of time after the bubble separation t_p. However, because the rate of discretization (i.e the frame rate) is slow compared to the characteristic time of cusp relaxation, two different states are described to happen just after the bubble separation at $t_p = 0$. In figure 5.11(a) is displayed the two extremum of the image sequence: the bubble for which the initial rear coordinate $(x_r)_0$ is minimum and the one for which it is maximum. The reader has to keep in mind that the flow is highly regular and periodic, such discrepancy between two situations described to happen at the same moment is only due to the low frame rate.

To correct this discrepancy, we use the bubble separation for which $(x_r)_0$ is minimum as a reference and interpolate the other curves assuming that the cusp relaxes at a constant velocity. This allows us to obtain a more accurate description of the dynamics (see figure 5.11).

We define the remaining time to pinch of τ as

$$\tau = T - t, \tag{5.2}$$

where T is the period of bubble generation and t the time after break-up, making τ the remaining time to pinch-off. We normalize τ by the capillary-inertial time scales,

$$\tau_{cap} = \sqrt{\frac{\rho_L h^3}{\gamma}}, \tag{5.3}$$

where ρ_L is the oil density, h the channel height (and width since square cross-section) and γ the surface tension of the system gas/solvent. One should note the values of τ_{cap} hardly change when varying the silicone oil viscosity as we have $\tau_{cap} \approx 0.00085$s within 2% for viscosities from 1 to 10^4 cS. This is due to the fact that the silicone oils properties hardly change when varying its

viscosity.

5.2.2 A few typical flows

The dynamics of the bubble generation are depicted for various viscosity from figure 5.12 to 5.15.
We first describe the evolution of the neck of the gas thread while it is being squeezed by the continuous phase by measuring the curvature at the neck κ_n as well as its width w_n as a function of time (see figure 5.10). At low viscosity, the growth of the curvature leading to the bubble generation appears to be slow before dramatically increasing prior to the separation of the bubble. At high viscosity, the values of the curvature are much lower and its evolution is smoother: there is no catastrophic collapse of the gaseous thread. The basics of the image processing to obtain both the curvature and the width of the neck are described in the appendix.
Depending on the value of the capillary number Ca,

$$Ca = \frac{\eta V_B}{\gamma} \tag{5.4}$$

one can find distinct behavior and time scales associated with the bubble generation. One can notice that the thinning process of the gaseous thread follows a power law within thef last moments of break-up, and that for all capillary numbers:

$$w_n/h = A(\frac{\tau}{\tau_{cap}})^{\alpha}. \tag{5.5}$$

While most studies are limited to a certain range of capillary number and thus report a single value for α, we are able to measure its value for a wide range of capillary numbers. α is plotted figure 5.16 against the flow capillary number.

This is the first time such a wide range of α value is reported in the literature for a bubble break-up in a co-flowing liquid. We are currently building a model to attempt to explain such a behavior for α. Most studies report α values for $Ca \sim 10^{-1}$ and thus obtain $\alpha \approx 1/3$. Studies of bubble break-up due to buoyancy in a quiescent viscous liquid [162, 164] reported an increase of α

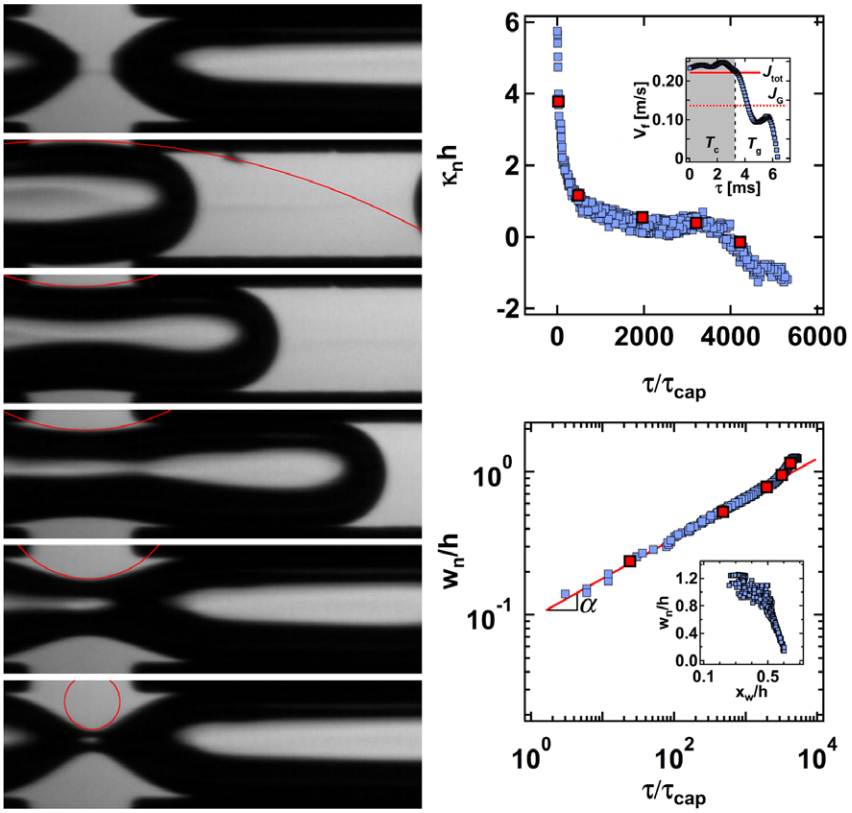

FIG. 5.12: Plot of the curvature and width of the neck vs non-dimensional time remaining after break-up. The silicone oil viscosity is $\nu = 1$ with a flow rate $Q_L = 360\mu L/min$. The CO_2 injection pressure is $P_G = 14.72psi$ and the measured gas flow rate $Q_G = 0.53sccm$. The capillary number associated with this flow is $Ca \approx 10^{-2}$.

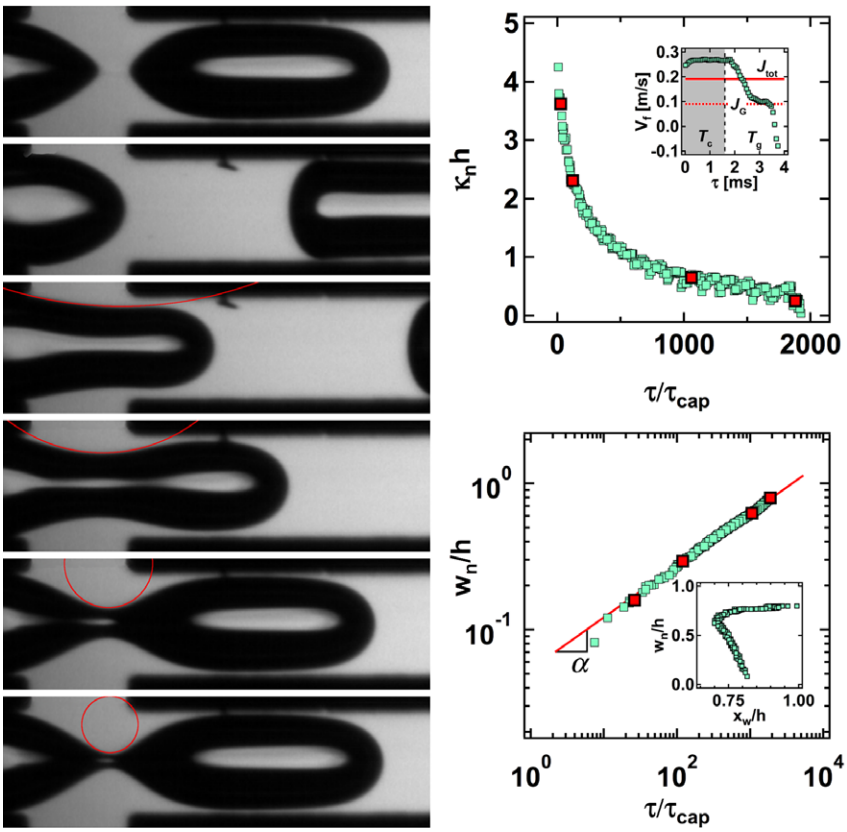

FIG. 5.13: Plot of the curvature and width of the neck vs non-dimensional time remaining after break-up. The silicone oil viscosity is $\nu = 10$ with a flow rate $Q_L = 380\mu L/min$. The CO_2 injection pressure is $P_G = 17.63psi$ and the measured gas flow rate $Q_G = 0.41sccm$. The capillary number associated with this flow is $Ca \approx 0.1$.

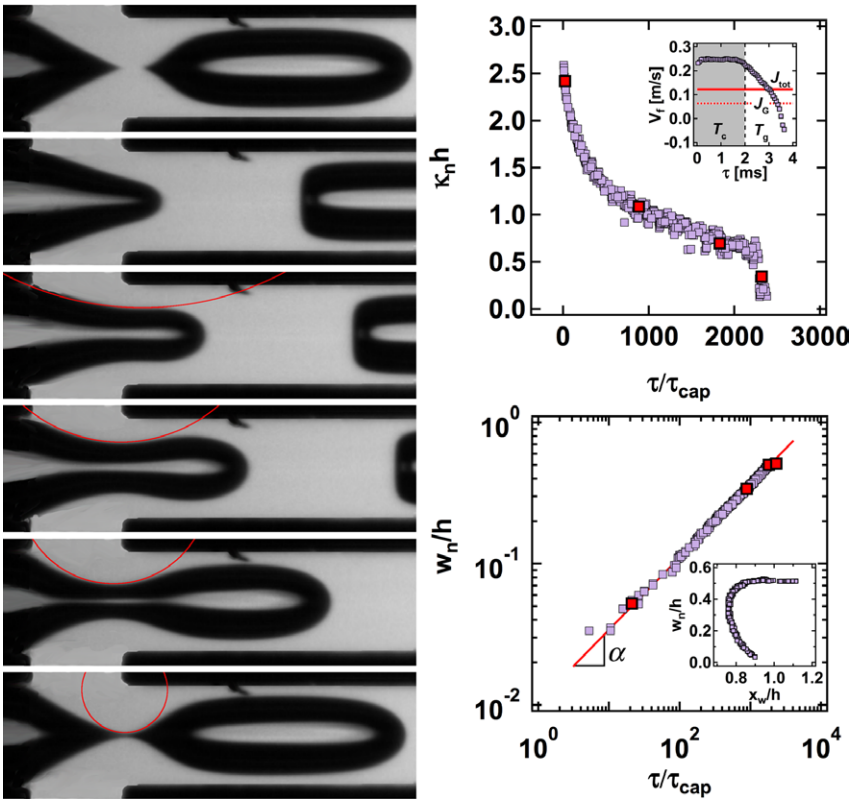

FIG. 5.14: Plot of the curvature and width of the neck vs non-dimensional time remaining after break-up. The silicone oil viscosity is $\nu = 10^3$ *with a flow rate* $Q_L = 220\mu L/min$. *The* CO_2 *injection pressure is* $P_G = 32.13psi$ *and the measured gas flow rate* $Q_G = 0.53sccm$. *The capillary number associated with this flow is* $Ca \approx 1$.

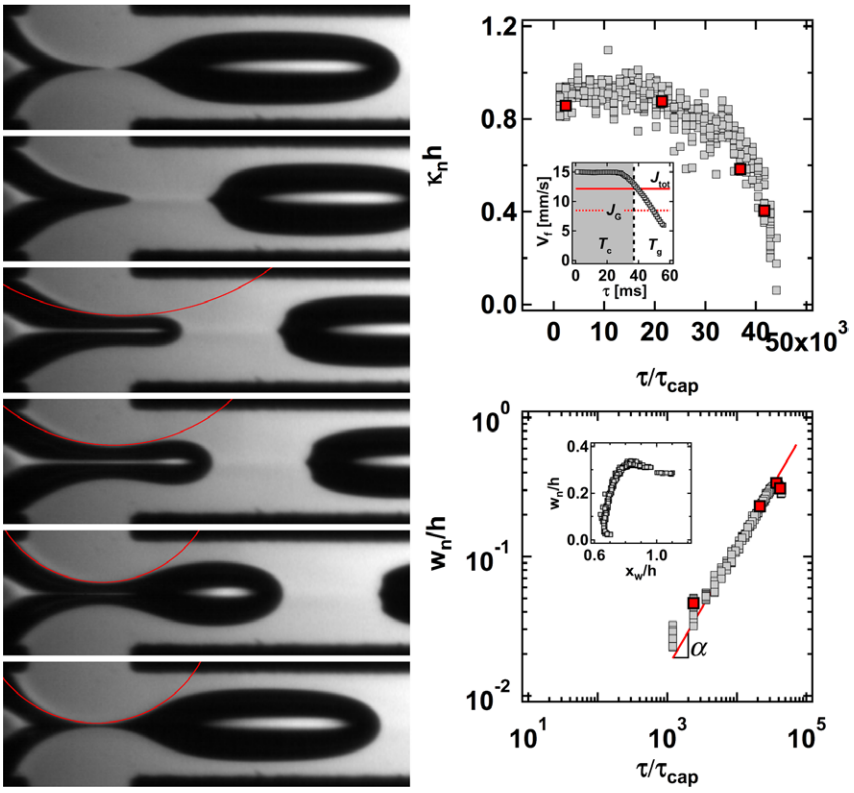

FIG. 5.15: Plot of the curvature and width of the neck vs non-dimensional time remaining after break-up. The silicone oil viscosity is $\nu = 10^4$ with a flow rate $Q_L = 14\mu L/min$. The CO_2 injection pressure is $P_G = 68.81psi$ and the measured gas flow rate $Q_G = 0.15sccm$. The capillary number associated with this flow is $Ca \approx 7$.

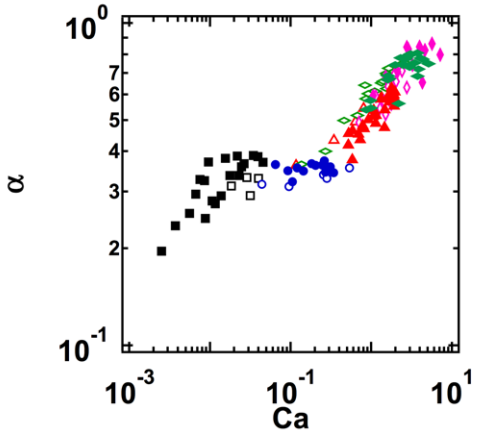

FIG. 5.16: Plot of α versus the capillary number for an oil viscosity ν = 1 (□), 10 (○),10^2 (△), 10^3 (▽), and 10^4 cS (◊). Filled symbols refer to the break-up of CO_2 bubbles while empty symbol refer to the break-up of air bubbles.

with the liquid viscosity. However, their model is not applicable to our case.

Additionally, one can notice a different behavior in the curvature of the neck for high value of Ca (see figure 5.15), as the curvature stays constant during the last moment of break-up. On the other hand, at lower capillary numbers, the curvature tends to rapidly increase in the last instants (see for instance figure 5.14). In that case, the neck becomes less and less slender, while the opposite happens at high Ca. We suspect that this can be explained by the fact that at high capillary numbers the viscous stress convects the bubble further from the junction as it is being pinched. However, a more systematic study of our data is needed to systematically inspect this phenomenon.

5.3 Segmented flow in square microchannel

In the following paragraph, we describe the shape of the bubbles generated in silicone oils of various viscosities. As elongated droplets are often described with ellipses [165], we fit the front and rear caps of individual bubbles with ellipses having semi-major axis a and semi-minor axis b. This method allows us to measure bubble front and rear curvature with a/b^2 as well as to estimate the bubble lateral extension with $2b$ (see figure 5.17). Incidentally, although

the liquid film thickness δ near the walls is not uniform along the bubble due to its finite length [88], measurements of b are useful for estimating the film thickness according to $\delta = w - 2b$. For low capillary numbers, we find $2b \sim w$ since the film is very thin and not readily visible. When $Ca > 10^{-2}$, the scaling $2b/w = 0.75Ca^{-0.06}$ yields good agreement with experimental data. The previous scaling enables the development of a simple model to predict the initial bubble volume Ω_0 in the viscous regime. By considering the initial bubble to be a cylinder of radius b and length d_0, we expect $\Omega_0 \sim d_0 b^2$, which leads to a single master curve relating the bubble's initial volume, the liquid volume fraction α_L and the capillary number.
The curvature of the bubble front is evaluated using the ellipse method for all flows and scales as $\kappa_F/w = 5.25Ca^{0.2}$, with values ranging from $2w$ (nearly spherical front cap) to $7w$ for high capillary numbers. We also find that the ratio of the rear to the front curvature κ_R/κ_F is an original and useful parameter to describe bubble shape in confined microgeometries and allows for examining the crossover between capillary and viscous regimes. At low capillary number, the rear curvature matches the front curvature as capillary stresses dominate viscous stresses. As the capillary number increases, the curvature of the rear cap decreases sharply before becoming null around $Ca = 0.5$. As viscous effects become predominant, bubbles adapt to viscous flow conditions and assume a bullet-like shape, see figure 5.18.
At high Ca, the recirculation region located behind the trailing meniscus and surrounding the flow centerline flattens the rear of the bubble and can even produce a reentrant cavity for very large Ca.

Here, we reported for the first time a basic description of the bubble shape over a wide range of capillary number. The simple relationship relating parameters such as a , b and κ_F with the capillary number could be very useful to validate numerical simulations for various flow conditions.

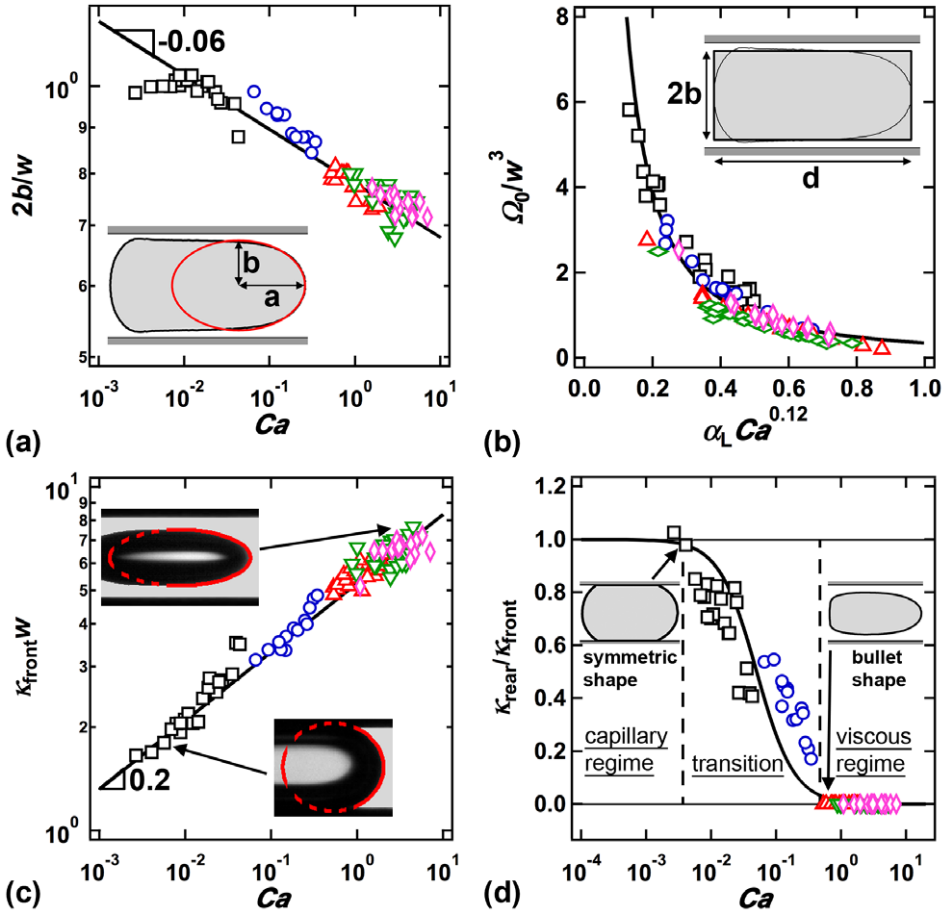

FIG. 5.17: Bubble description as a function of the capillary number with oil viscosity $\nu = 1$ (□), 10 (○),10^2 (△), 10^3 (▽), and 10^4 cS (◊). (a) Fit of the bubble front using an ellipse. (b) Initial calculated volume (c) Curvature of the bubble front. (d) Ratio between the rear cap curvature and the front cap curvature vs capillary number.

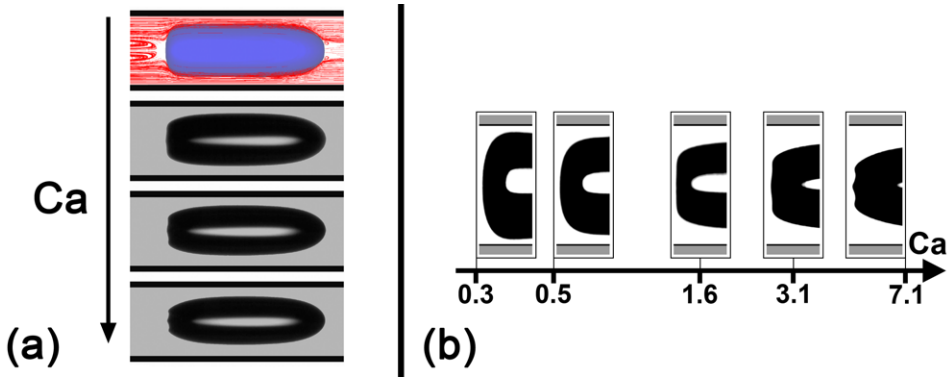

FIG. 5.18: (a) Evolution of the bubble shape as the capillary number increases. The first image is from a simulation by Taha et al. [81]. (b) Evolution of the bubble rear as the capillary number increases.

Chapter 6

Conclusions and prospects

This thesis presents several contributions to the field of multiphase flows in microgeometries:

- The investigation of the long scale behavior of dissolving CO_2 bubbles in water allowed us to establish a relationship between the phase distribution and the gaseous and liquid flow rates. The saturating, coalescing and dissolving regimes are scrutinized and characterized. The morphological and dynamical transition from segmented to bubbly flow is also examined, while the bubble velocity is showed to depend solely on its size.

- A simple model is proposed for the initial gas-liquid mass exchange in microgeometries and is successfully confronted to experimental results with different solvents (alkanes, alcohols, silicone oils). A practical coefficient k_D is presented to assess the initial dissolution rate of given fluid pairs which combines the two fundamentals of gas absorption, namely saturation and the dynamics at which the system approaches equilibrium.

- The early behavior (just after the two phases are brought in contact) of CO_2 micro bubbles in alkanes and alcohols is investigated. In this regime during which most of the mass exchange occurs, the dissolution dynamics appear to depend solely on the concentration gradient between the two phases and not on the hydrodynamics. This result is fundamentally different from what researchers had found at longer times and suggests that in this regime the mass exchange is non-inhibited.

- The initial microfluidic dissolution regime of CO_2 in oils is investigated over a wide range of viscosity from low to very high. By analyzing the morphology of dissolving bubbles from low to large capillary numbers, we extract the initial steady mass transfer flux during gas absorption. Again, our basic model is respected at the early times and the dissolution coefficient k_D is used to quantify the mass exchange process.

- The flow morphology of microbubbles in confined viscous environments is explored within several microgeometries. We show that bubbles shapes depend on the capillary number and that an increase in viscosity has a tremendous impact on the flow structure. Using complex microgeometries, we present a wealth of patterns attainable at large capillary number.

- We scrutinize the bubble generation by hydrodynamic focusing at a cross shaped mixing section and specifically consider the impact of the viscosity on the formation dynamics. We show that the capillary number has a considerable impact on the process, but that most of the general scaling law are still valid at large capillary number.

Appendix A

ImageJ Script for Bubble Tracking

Listing A.1: ImageJ macro for the obtention of the coordinates and curvature

```
1  //Path to the folder where are located the original images
2  folder_src ="/Users/martin/Documents/EXP3/SOURCES/CO2 PDMS/1cst/";
3  //Path to the folder where the processed images will be saved
4  folder_dest_parent="/Users/martin/Documents/cusp_study/CO2/";
5  //definition of the identifiers to keep info. regarding gas and viscosity
6  gas="CO2";
7  digit="1";
8
9  //Listing of the content of the folder "folder" before starting the loop. The name of each subfolder is stored
       in an
10 //array of strings "folder_name" and the number of processed images it holds (needed when importing the
       image sequence)
11 list_f=getFileList(folder);
12 folder_name = newArray("");
13 folder_length= newArray("");
14 for (i=0; i<list_f.length; i++) {
15     if (endsWith(list_f[i], "kfps/")==1){
16         folder_name=Array.concat(folder_name, folder+substring(list_f[i], 0, lengthOf(list_f[i])-1));
17         temp_folder_length=getFileList(folder+ list_f[i]);
18         nbr_slice=temp_folder_length.length;
19         folder_length=Array.concat(folder_length, nbr_slice);
20     }
21 }
22 folder_name=Array.slice(folder_name,1);
23 folder_length =Array.slice(folder_length,1);
24
25 //Here begins LOOP1, which goes through each of "folder" subfolder and processes them
26 for (i=0; i<folder_name.length; i++) {
27     run("Clear Results");
28     roiManager("reset");
29     sequence_folder=folder_name[i];
30     nbr_slice_seq= folder_length[i];
31
```

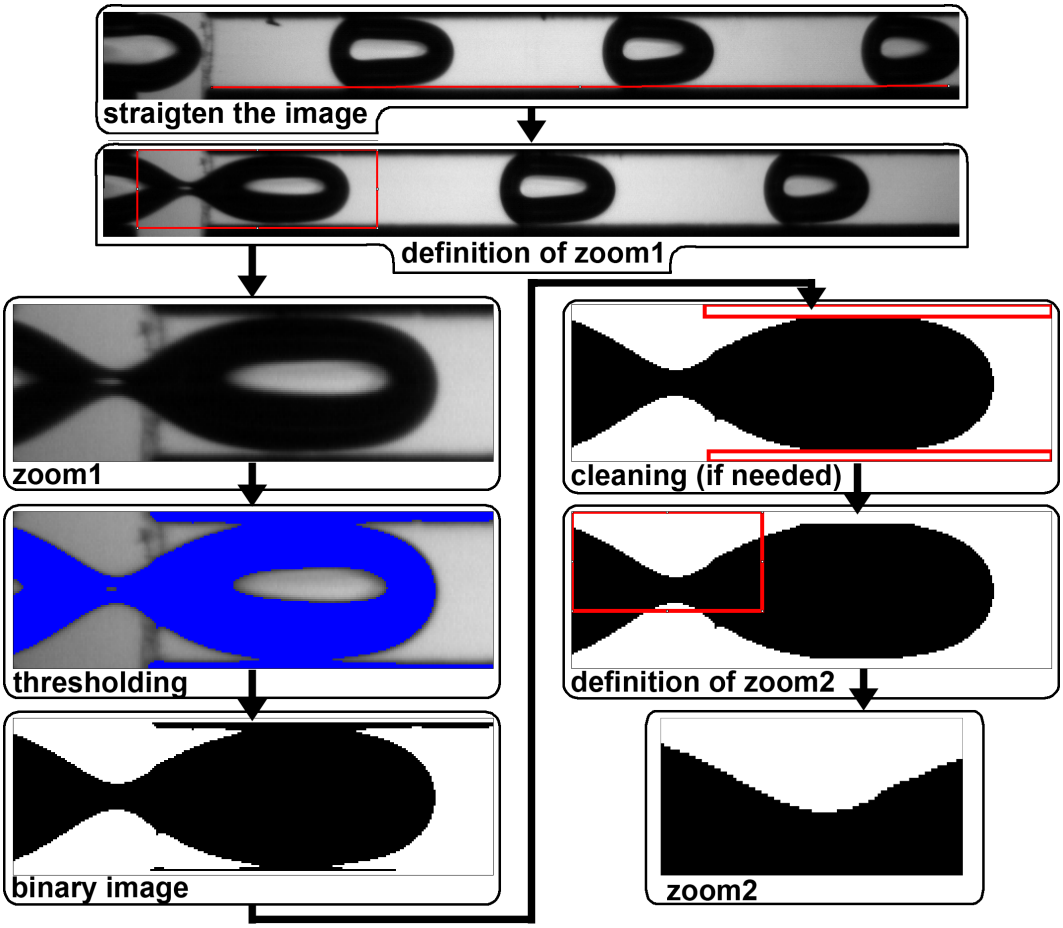

FIG. A.1: Visual summary of the ImageJ macro displayed in listing A.1

```
32  //name_folder contains the path to the folder folder_name[i] of interest
33  name_folder=substring(sequence_folder, lengthOf(File.getParent(sequence_folder))+1, lengthOf(
        sequence_folder));
34
35  //some basic string manipulation are required to extract the identifiers (which are the gas injection
36  //pressure, the gas flow rate sccm, the liquid flow rate QL_2 and the frame per seconds of the
        recording)
37  //from string name_folder
38  sub_name=split(name_folder, "/ psi sccm kfps .");
39  sccm=parseInt(sub_name[0])+parseInt(sub_name[1])/100;
40  pressure=parseInt(sub_name[2])+parseInt(sub_name[3])/100;
41  pressure1= sub_name[2];
42  pressure2=sub_name[3];
43  digit_out=digit_out_ini;
44  QL_2=parseInt(sub_name[4]);
45
46  //Display of the path and the identifiers associated with the
47  //processed folder
48  print("["+i+"]: "+"sccm:",sccm,"pressure:",pressure,"QL/2:",QL_2,"kfps:",kfps);
49
50  //generation of the destination directory "folder_dest_parent" if it does not exist yet
51  if (File.exists(folder_dest_parent)!=1)
52      File.makeDirectory(folder_dest_parent);
53  //create folder_dest_parent +1cst
54  folder_last=substring(folder, lengthOf(File.getParent(folder))+1, lengthOf(folder));
55  dir_dest= folder_dest_parent+folder_last;
56  if (File.exists(dir_dest)!=1)
57      File.makeDirectory(dir_dest);
58
59  //formation of the text file name using a string
60  //structure similar to the one used to save the original
61  //files: 0.15sccm15.69psi.625.625.10kfps for the file
62  //corresponding to the flow of CO2 in 1cSt oil (see digit and
63  //gas at the beginning of the code) with a gas flow rate of
64  //0.15 CCM (STP), injected at 15.69psi, with an oil flow
65  //of 625+625=1250 muL/min and recorded at 10kfps
66  new_name=toString(sccm)+"sccm"+toString(pressure)+"psi."+toString(QL_2)+"."+toString(kfps)+"
        kfps";
67  //definition of the paths where the results will be saved
68  dir_dest_TIF=dir_dest+new_name+".tif";
69  dir_dest_ZIP=dir_dest+new_name+".zip";
70  dir_dest_TXT=dir_dest+new_name+".txt";
71  dir_dest_resliceTIF=dir_dest+"reslice"+new_name+".tif";
72  //results column name
73  name_parameter="par_"+gas+digit+"_"+d2s(pressure1,0)+"_"+d2s(pressure2,0)+"_"+d2s(QL_2,0);
74  name_xfront="xfront_"+gas+digit+"_"+d2s(pressure1,0)+"_"+d2s(pressure2,0)+"_"+d2s(QL_2,0);
75  name_areafront="areaf_"+gas+digit+"_"+d2s(pressure1,0)+"_"+d2s(pressure2,0)+"_"+d2s(QL_2,0)
        ;
76  name_tsep="tsep_"+gas+digit+"_"+d2s(pressure1,0)+"_"+d2s(pressure2,0)+"_"+d2s(QL_2,0);
77  name_xradius="xcent_"+gas+digit+"_"+d2s(pressure1,0)+"_"+d2s(pressure2,0)+"_"+d2s(QL_2,0);
78  name_yradius="ycent_"+gas+digit+"_"+d2s(pressure1,0)+"_"+d2s(pressure2,0)+"_"+d2s(QL_2,0);
79  name_curvature="curv_"+gas+digit+"_"+d2s(pressure1,0)+"_"+d2s(pressure2,0)+"_"+d2s(QL_2,0)
        ;
80
81  //Import original sequence toi ImageJ
82  run("Image Sequence...", "open=sequence_folder number=nbr_slice_seq starting=1 increment=1 scale
        =100 file=[] sort");
83
84  //the image is straightened if need be
85  run("Line Width...", "line=1");
86  setTool("line");
```

```
87      title = "WaitForUserDemo";
88      msg = "Draw a line following the wall of the channel, then click \"OK\".";
89      waitForUser(title, msg);
90      if (selectionType!=5)
91          exit("Straight line selection required");
92      getLine(x1, y1, x2, y2, lineWidth);
93      getPixelSize(unit, width, height, depth);
94      x1*=width; y1*=height; x2*=width; y2*=height;
95      angle_l = getAngle(x1, y1, x2, y2);
96      if (angle_l>180)
97          angle_l = angle_l-360;
98      run("Rotate... ", "angle=angle_l grid=10 interpolation=Bilinear stack");
99      run("Select All");
100     //record the angle value in a result table
101     setResult(name_parameter, 0, angle_l);
102
103     //the first zoom is set manually and its coordinates saved
104     msg = "Crop from the left of the side channels to the extremity of the gaseous thread just before
            separation (centered relative to the center of the channel). \"OK\".";
105     waitForUser(title, msg);
106     getSelectionBounds(x_zoom1, y_zoom1, width_zoom1, height_zoom1);
107     run("Crop");
108     titre=getTitle();
109     //save zoom1 coordinates
110     setResult(name_parameter, 1, x_zoom1);
111     setResult(name_parameter, 2, y_zoom1);
112     setResult(name_parameter, 3, width_zoom1);
113     setResult(name_parameter, 4, height_zoom1);
114
115     //the threshold is set appropriately (checked visually)
116     title = "WaitForUserDemo";
117     msg = "Set the value of Threshold , BUBBLE IN BLUE [Huang+OverUnder]. Typical 190-255.\"OK
            \".";
118     waitForUser(title, msg);
119     getThreshold(lower, upper);
120     setThreshold(lower, upper);
121     run("Convert to Mask", "method=Huang background=Light");
122     //save threshold values
123     setResult(name_parameter, 5, lower);
124     setResult(name_parameter, 6, upper);
125
126     //image processing to fill the holes (flat interface appears white)
127     run("Invert", "stack");
128     run("Colors...", "foreground=white background=black selection=red");
129     width=getWidth();
130     height=getHeight();
131     temp_w= width+1;
132     run("Canvas Size...", "width=temp_w height=height position=Top-Right");
133     makeRectangle(0, 0, temp_w, 2);
134     run("Fill", "stack");
135     temp_h= height-2;
136     makeRectangle(0, temp_h, temp_w, 2);
137     run("Fill", "stack");
138     run("Fill Holes", "stack");
139     run("Select None");
140     run("Canvas Size...", "width=width height=height position=Top-Right");
141
142     //using zoom1, we determine when the bubble separation occurs
143     //a separation is identified by a discontinuity in the front coordinate of the gaseous thread
144     nb_total_slice=nSlices;
145     x_front=newArray(nb_total_slice);
```

```
146     height =getHeight();
147     for (slice_nb=0; slice_nb<(nb_total_slice); slice_nb ++) {
148         setSlice(slice_nb+1);
149         height =getHeight();
150         run("Select None");
151         doWand(5, round(height/2));
152         getSelectionBounds(x_sb, y_sb, width, height);
153         x_front[slice_nb]=width;
154         setResult(name_xfront, slice_nb, width);
155         getStatistics(area_f);
156         setResult(name_areafront, slice_nb, area_f);
157     }
158     //detection of separation, ie when bubble is generated
159     separation=newArray("0");
160     for (slice_nb=0; slice_nb<(nb_total_slice-1); slice_nb ++) {
161         if ((x_front[slice_nb+1]<(x_front[slice_nb]-0.25*x_front[slice_nb]))&&(separation[separation.
                length-1]!=(slice_nb+1))){
162         separation=Array.concat(separation,slice_nb+2);
163         }
164     }
165     separation = Array.slice(separation,1);
166     separation=Array.concat(separation, separation[separation.length-1]);
167
168     //we generate a time array that is reset at 0 when there is separation
169     j=0;
170     j_sep=0;
171     delta_t=separation[0]-1;
172     do{
173         p=0;
174         do {
175             value_t=-delta_t+p;
176             setResult(name_tsep,j, value_t);
177             j=j+1;
178             p=p+1;
179         } while (value_t<0);
180         j_sep=j_sep+1;
181         delta_t=separation[j_sep]-separation[j_sep-1]-1;
182     } while (j_sep<(separation.length-1));
183
184     //here we define zoom2, the zoom necessary to extract info. on the gaseous neck
185     run("Select All");
186     setTool("rectangle");
187     setSlice(separation[0]-1);
188     msg = "Crop from the left of the side channels to the extrimity of the curve just before separation.
            CUT IT below the center. \"OK\".";
189     title = "WaitForUserDemo";
190     waitForUser(title, msg);
191     getSelectionBounds(x_zoom2, y_zoom2, width_zoom2, height_zoom2);
192     run("Crop");
193     //save zoom2 coordinates
194     setResult(name_parameter, 7, x_zoom2);
195     setResult(name_parameter, 8, y_zoom2);
196     setResult(name_parameter, 9, width_zoom2);
197     setResult(name_parameter, 10, height_zoom2);
198     }
199     //visual verification of the result using ROI manager
200     // visual validation
201     title = "WaitForUserDemo";
202     msg = "Check if it works well. Then press \"OK\".";
203     waitForUser(title, msg);
204     //if validated, data is saved un text files. The ROI is also saved for future use.
```

```
205     roiManager("Save", dir_dest_ZIP);
206     roiManager("reset");
207     saveAs("Tiff", dir_dest_TIF);
208     selectWindow("reslice"+titre);
209     saveAs("Tiff", dir_dest_resliceTIF);
210     saveAs("Results", dir_dest_TXT);
211     run("Close All");
212 }
```

Listing A.2: ImageJ macro for the obtention of the coordinates and curvature

```
1  //Path to the folder where are located the processed images obtained previously [zoom2]
2  folder_src="/Users/martin/Documents/cusp_study/CO2/1cst/";
3  //identifiers used to name the text files under which the results of this macro are saved
4  gas="CO2";
5  digit="1";
6
7  //Listing of the content of the folder "folder_src" before starting the loop. The name of each subfolder is
       stored in an
8  //array of strings "folder_name" and the number of processed images it holds (needed when importing the
       image sequence)
9  list_f=getFileList(folder_src);
10 folder_name = newArray("");
11 folder_length= newArray("");
12 for (i=0; i<list_f.length; i++) {
13     if ((endsWith(list_f[i], ".tif")==1)&&(startsWith(list_f[i],"reslice")==0)){
14         folder_name=Array.concat(folder_name, folder_src+substring(list_f[i], 0, lengthOf(list_f[i])));
15         temp_folder_length=getFileList(folder_src+ list_f[i]);
16         nbr_slice=temp_folder_length.length;
17         folder_length=Array.concat(folder_length, nbr_slice);
18     }
19 }
20 folder_name=Array.slice(folder_name,1);
21 folder_length =Array.slice(folder_length,1);
22
23 //Here begins LOOP1, which goes through each of "folder_src" subfolder and processes them
24 for (i=0; i<folder_name.length; i++) {
25     run("Clear Results");
26     roiManager("reset");
27     sequence_folder=folder_name[i];
28     name_folder=substring(sequence_folder, lengthOf(File.getParent(sequence_folder))+1, lengthOf(
           sequence_folder));
29     //name_folder contains the path to the folder folder_name[i] of interest
30     //some basic string manipulation are required to extract the identifiers (which are the gas injection
31     //pressure, the gas flow rate sccm, the liquid flow rate QL_2 and the frame per seconds of the
           recording)
32     //from string name_folder
33     sccm_i=indexOf(name_folder, "sccm");
34     sccm=parseFloat(substring(name_folder, 0, sccm_i));
35     psi_i=indexOf(name_folder, "psi");
36     pressure=parseFloat(substring(name_folder, sccm_i+4, psi_i));
```

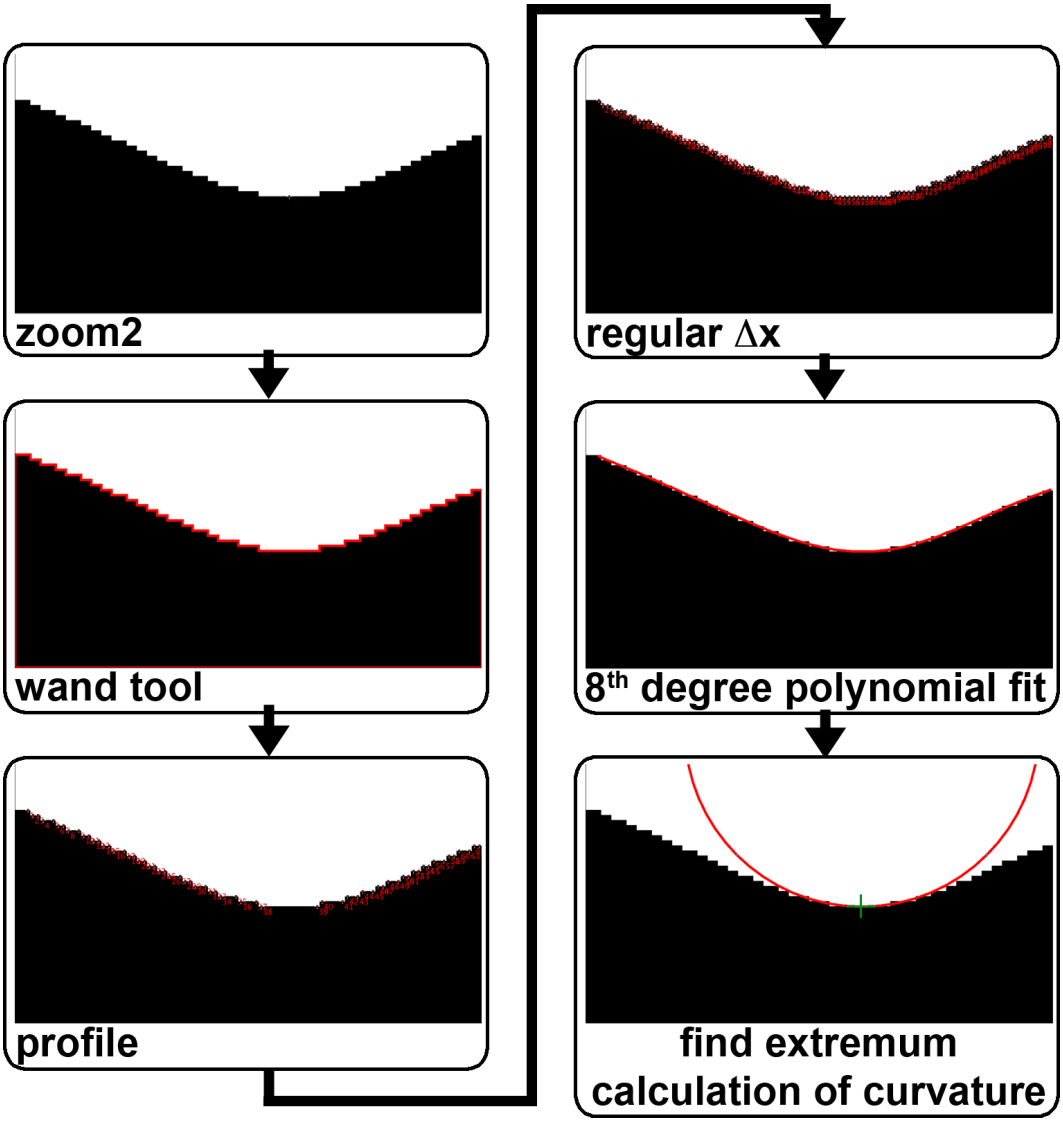

FIG. A.2: Visual summary of the ImageJ macro described in listing A.2

```
37      pressure1=floor(pressure);
38      pressure2=(pressure-floor(pressure))*100;
39      QL__2__i=indexOf(substring(name__folder, psi__i+4), ".");
40      QL__2= parseInt(substring(name__folder,psi__i+4, psi__i+4+QL__2__i));
41      kfps__i=indexOf(substring(name__folder, psi__i+4+QL__2__i), ".");
42      kfps__2i=indexOf(substring(name__folder, psi__i+4+QL__2__i), "kfps");
43      kfps = parseFloat(substring(name__folder, psi__i+4+QL__2__i+kfps__i+1, psi__i+4+QL__2__i+kfps__2i));
44      //Display of the path and the identifiers associated with the
45      //processed folder
46      print(name__folder);
47      print("["+i+"]: "+"sccm:",sccm,"pressure:",pressure,"QL/2:",QL__2,"kfps:",kfps);
48      //generation of the destination directory "dir__dest" if it does not exist yet
49      dir__dest=folder__src+"/curvature/";
50      if (File.exists(dir__dest)!=1)
51          File.makeDirectory(dir__dest);
52      //formation of the text file name using a string
53      //structure similar to the one used to save the original
54      //files: 0.15sccm15.69psi.625.625.10kfps for the file
55      //corresponding to the flow of CO2 in 1cSt oil (see digit and
56      //gas at the beginning of the code) with a gas flow rate of
57      //0.15 CCM (STP), injected at 15.69psi, with an oil flow
58      //of 625+625=1250 muL/min and recorded at 10kfps
59      new__name=toString(sccm)+"sccm"+toString(pressure)+"psi."+toString(QL__2)+"."+toString(kfps)+"
            kfps";
60      //destination path where the results and the associated ROI will be saved
61      dir__dest__TXT=dir__dest+new__name+".txt";
62      dir__dest__ZIP=dir__dest+new__name+".zip";
63      //definition of the column names under which the results will
64      //be saved. The output of the macro are the coordinates
65      //and the curvature of the point where the neck is minimum
66      name__xthread ="xthread__"+gas+digit+"__"+d2s(pressure1,0)+"__"+d2s(pressure2,0)+"__"+d2s(QL__2
            ,0);
67      name__ythread ="ythread__"+gas+digit+"__"+d2s(pressure1,0)+"__"+d2s(pressure2,0)+"__"+d2s(QL__2
            ,0);
68      name__curvature="curv__"+gas+digit+"__"+d2s(pressure1,0)+"__"+d2s(pressure2,0)+"__"+d2s(QL__2,0)
            ;
69      //the processed images (zoom2), stored in sequence__folder are imported into ImageJ
70      open(sequence__folder);
71
72      //here begins LOOP2 which goes through each image from the folder folder__name[i]
73      nb__total__slice=nSlices;
74      for (slice__nb=0; slice__nb<nb__total__slice; slice__nb ++) {
75          setSlice(slice__nb+1);
76          //get the contour of the processed gaseous thread
77          doWand(0,y__sb+height__sb/2);
78          //only get the profile
79          get__profile();
80          //create a regular grid in the x-direction
81          //and put the coordinates of the function to fit in (x__,y__)
82          get__regular__gridx();
```

```
83          getSelectionCoordinates(x__, y__);
84
85          //fit the curve with an 8th degree polynom
86          //a+bx+cx2+dx3+ex4+fx5+gx6+hx7+kx8
87          Fit.doFit("8th Degree Polynomial", x__, y__);
88          a=Fit.p(0);
89          b=Fit.p(1);
90          c=Fit.p(2);
91          d=Fit.p(3);
92          e=Fit.p(4);
93          f=Fit.p(5);
94          g=Fit.p(6);
95          h=Fit.p(7);
96          k=Fit.p(8);
97          //x_fit and y_fit are the coordinate of the polynom fitting the curve
98          p_max=x__.length;
99          x_fit=newArray(p_max);
100         y_fit=newArray(p_max);
101         for (j=0; j<p_max; j++) {
102             x_fit[j]=x__[j];
103             y_fit[j]=Fit.f(x__[j]);
104         }
105         //determination of the coordinates where the gas neck is
106         //minimum and computation of the curvature
107         //so I discretize the fitted function in 200 sections (to
108         //get better precision on where the first minimum is)
109         length_discretization=200;
110         //creation of arrays to store the 200 coordinate of the
111         //interpolated fit function
112         x_disc=newArray(length_discretization);
113         y_disc=newArray(length_discretization);
114         //and to store its first and second derivative
115         sec_derivative =newArray(length_discretization);
116         first_derivative=newArray(length_discretization);
117         //we use the function "Fit." to interpolate the polynomial fitting the neck profile
118         //since it is a polynom, we have an analytical expression of its derivatives
119         for (j=0; j<length_discretization; j++) {
120             x_disc[j]=minx_fit+j*(maxx_fit-minx_fit)/(length_discretization-1);
121             y_disc[j]=Fit.f(x_disc[j]);
122             first_derivative[j]=b+2*c*x_disc[j]+3*d*pow(x_disc[j], 2)+4*e*pow(x_disc[j], 3)+5*f*pow(
                    x_disc[j], 4)+6*g*pow(x_disc[j], 5)+7*h*pow(x_disc[j], 6)+8*k*pow(x_disc[j], 7);
123         }
124
125         //the first time the derivative changes sign is at the extremum, if extremum there is
126         //we obtain the coordinates of the extremum (maximum usually, minimum for low Ca cases with
                negative
127         //curvature) the first time the first derivative changes
128         //sign
129         j=length_discretization/10;
130         do {
```

```
131             j_limit=j;
132             j=j+1;
133         } while ((first_derivative[j-1]*first_derivative[j]>0)&&(j<(length_discretization-1)));
134
135         //in the case of no minimum (e.g. during growth or
136         //retraction)
137         if (j_limit==(length_discretization-2))
138             j_limit=NaN;
139
140
141         //2 cases either there is a minimum or there is not
142         //again to avoid border effects:
143         if (j_limit<(length_discretization*0.8)){
144             //then there is a minimum
145             x_min=x_disc[j_limit];
146             y_min=Fit.f(x_min);
147             //we add the point where the curvature is calculated at
148             //the ROI manager for visual
149             //verification
150             makePoint(x_min, y_min);
151             roiManager("Add");
152             ///determination of the local curvature using the
153             //analytical expression
154             sec_derivative_xmin=2*c+6*d*x_min+12*e*pow(x_min, 2)+20*f*pow(x_min, 3)+30*g*pow
                    (x_min, 4)+42*h*pow(x_min, 5)+56*k*pow(x_min,6);
155             curvature_n=abs(sec_derivative_xmin);
156             first_derivative_xmin=b+2*c*x_min+3*d*pow(x_min, 2)+4*e*pow(x_min, 3)+5*f*pow(
                    x_min, 4)+6*g*pow(x_min, 5)+7*h*pow(x_min, 6)+8*k*pow(x_min, 7);
157             curvature_d=pow((1+pow(first_derivative_xmin,2)),3/2);
158             curvature=curvature_n/curvature_d;
159             //depending on the sign of the second derivative, we
160             // we add to the ROI manager the curvature computed
161             //we record the point coordinates and its associated
162             //curvature in a Results table
163             if (sec_derivative_xmin<0){
164                 x_left=x_min-radius_c;
165                 y_left=y_min-2*radius_c;
166                 makeOval(x_left, y_left, 2*radius_c, 2*radius_c);
167                 roiManager("Add");
168                 setResult(name_xthread, slice_nb, x_min);
169                 setResult(name_ythread, slice_nb, y_min);
170                 setResult(name_curvature, slice_nb, d2s(curvature,6));
171             } else {
172                 x_left=x_min-radius_c;
173                 y_left=y_min+2*radius_c;
174                 makeOval(x_left, y_left, 2*radius_c, 2*radius_c);
175                 roiManager("Add");
176                 setResult(name_xthread, slice_nb, x_min);
177                 setResult(name_ythread, slice_nb, y_min);
178                 setResult(name_curvature, slice_nb, -d2s(curvature,6));
```

```
179             }
180         //If there is non mimim we fill with NaN
181         } else {
182             setResult(name_curvature, slice_nb, "NaN");
183             setResult(name_xthread, slice_nb, NaN);
184             setResult(name_ythread, slice_nb, NaN);
185         }
186     //to display the evolution of the computation
187     progress=slice_nb/nb_total_slice;
188     showProgress(progress);
189 }
190     //we display the obtained ROI (i.e. the fitted polynomial,
191     //the point and the radius of curvature on top of the images
192     //for visual verification
193     roiManager("Show All");
194     // visual validation
195     title = "WaitForUserDemo";
196     msg = "Check if it works well. Then press \"OK\".";
197     waitForUser(title, msg);
198
199     //We save the ROI
200     roiManager("Save", dir_dest_ZIP);
201     roiManager("reset");
202     //we save the result table obtained
203     saveAs("Results", dir_dest_TXT);
204     run("Close All");
205 }
206 print("done!");
```

Bibliography

[1] L Zhang, J M Koo, L Jiang, M Asheghi, K E Goodson, J G Santiago, and T W Kenny. Measurements and modeling of two-phase flow in microchannels with nearly constant heat flux boundary conditions. *Journal of Microelectromechanical Systems*, 11(1):12–19, 2002.

[2] D J Laser and J G Santiago. A review of micropumps. *Journal of Micromechanics and Microengineering*, 14(6):R35–R64, 2004.

[3] D J Beebe, G A Mensing, and G M Walker. Physics and applications of microfluidics in biology. *Annu Rev Biomed Eng*, 4:261–286, 2002.

[4] A Khademhosseini, R Langer, J Borenstein, and J P Vacanti. Microscale technologies for tissue engineering and biology. *Proceedings of the National Academy of Sciences of the United States of America*, 103(8): 2480–2487, 2006.

[5] A Manz, N Graber, and H M Widmer. Miniaturized Total Chemical-Analysis Systems - a Novel Concept for Chemical Sensing. *Sensors and Actuators B-Chemical*, 1(1-6):244–248, 1990.

[6] Kamentsky and M R Melamed. Spectrophotometric Cell Sorter. *Science*, 156(3780):1364–&, 1967.

[7] Klavs F Jensen. Microreaction engineering : is small better? *Chemical Engineering Science*, 56(2):293–303, 2001.

[8] P S Dittrich and A Manz. Lab-on-a-chip: microfluidics in drug discovery. *Nature Reviews Drug Discovery*, 5(3):210–218, 2006.

[9] E Verpoorte. Microfluidic chips for clinical and forensic analysis. *Electrophoresis*, 23(5):677–712, 2002.

[10] H Craighead. Future lab-on-a-chip technologies for interrogating individual molecules. *Nature*, 442(7101):387–393, 2006.

[11] S Haeberle and R Zengerle. Microfluidic platforms for lab-on-a-chip applications. *Lab on a Chip*, 7(9):1094–1110, 2007.

[12] V M Ugaz, R D Elms, R C Lo, F A Shaikh, and M A Burns. Microfabricated electrophoresis systems for DNA sequencing and genotyping applications: current technology and future directions. *Philosophical Transactions of the Royal Society a-Mathematical Physical and Engineering Sciences*, 362(1818):1105–1129, 2004.

[13] J O Tegenfeldt, C Prinz, H Cao, R L Huang, R H Austin, S Y Chou, E C Cox, and J C Sturm. Micro- and nanofluidics for DNA analysis. *Analytical and Bioanalytical Chemistry*, 378(7):1678–1692, 2004.

[14] J W Hong, V Studer, G Hang, W F Anderson, and S R Quake. A nanoliter-scale nucleic acid processor with parallel architecture. *Nature Biotechnology*, 22(4):435–439, 2004.

[15] M U Kopp, A J de Mello, and A Manz. Chemical amplification: Continuous-flow PCR on a chip. *Science*, 280(5366):1046–1048, 1998.

[16] N Lion, T C Rohner, L Dayon, I L Arnaud, E Damoc, N Youhnovski, Z Y Wu, C Roussel, J Josserand, H Jensen, J S Rossier, M Przybylski, and H H Girault. Microfluidic systems in proteomics. *Electrophoresis*, 24(21):3533–3562, 2003.

[17] A J Hughes, R K C Lin, D M Peehl, and A E Herr. Microfluidic integration for automated targeted proteomic assays. *Proceedings of the National Academy of Sciences of the United States of America*, 109(16): 5972–5977, 2012.

[18] R S Jayashree, L Gancs, E R Choban, A Primak, D Natarajan, L J Markoski, and P J A Kenis. Air-breathing laminar flow-based microfluidic fuel cell. *Journal of the American Chemical Society*, 127(48):16758–16759, 2005.

[19] A V Pattekar and M V Kothare. A microreactor for hydrogen production in micro fuel cell applications. *Journal of Microelectromechanical Systems*, 13(1):7–18, 2004.

[20] J W Lee and E Kjeang. A perspective on microfluidic biofuel cells. *Biomicrofluidics*, 4(4):41301, 2010.

[21] H Tavana, D Huh, J B Groberg, and S Takayama. Microfluidics, Lung Surfactant, and Respiratory Disorders. *Labmedicine*, 40(4):203–209, 2009.

[22] Madhvanand N Kashid and Lioubov Kiwi-Minsker. Microstructured Reactors for Multiphase Reactions: State of the Art. *Industrial & Engineering Chemistry Research*, 48(14):6465–6485, 2009.

[23] Madhvanand N Kashid, Albert Renken, and Lioubov Kiwi-Minsker. GasâĂŞliquid and liquidâĂŞliquid mass transfer in microstructured reactors. *Chemical Engineering Science*, 66(17):3876–3897, 2011.

[24] R Fisher, M K Shah, D Eskin, K Schmidt, A Singh, S Molla, and F Mostowfi. Equilibrium gas-oil ratio measurements using a microfluidic technique. *Lab on a Chip*, 13(13):2623–2633, 2013.

[25] V Berejnov, N Djilali, and D Sinton. Lab-on-chip methodologies for the study of transport in porous media: energy applications. *Lab on a Chip*, 8(5):689–693, 2008.

[26] Margot G Gerritsen and Louis J Durlofsky. Modeling Fluid Flow in Oil Reservoirs. *Annual Review of Fluid Mechanics*, 37(1):211–238, 2005.

[27] Jacob Bear. *Dynamics of fluids in porous media*, New York, 1988. ISBN 0486656756.

[28] R D Chambers, M A Fox, D Holling, T Nakano, T Okazoe, and G Sandford. Elemental fluorine - Part 16. Versatile thin-film gas-liquid multichannel microreactors for effective scale-out. *Lab on a Chip*, 5(2):191–198, 2005.

[29] R Chen, P F Dong, J H Xu, Y D Wang, and G S Luo. Controllable microfluidic production of gas-in-oil-in-water emulsions for hollow microspheres with thin polymer shells. *Lab on a Chip*, 12(20):3858–3860, 2012.

[30] L Yang, K Wang, S Mak, Y K Li, and G S Luo. A novel microfluidic technology for the preparation of gas-in-oil-in-water emulsions. *Lab on a Chip*, 13(17):3355–3359, 2013.

[31] J I Park, A Saffari, S Kumar, A Gunther, and E Kumacheva. Microfluidic Synthesis of Polymer and Inorganic Particulate Materials. *Annual Review of Materials Research, Vol 40*, 40:415–443, 2010.

[32] E Brouzes, M Medkova, N Savenelli, D Marran, M Twardowski, J B Hutchison, J M Rothberg, D R Link, N Perrimon, and M L Samuels. Droplet microfluidic technology for single-cell high-throughput screening. *Proc Natl Acad Sci U S A*, 106(34):14195–14200, 2009.

[33] M Kim, A Sell, and D Sinton. Aquifer-on-a-chip: understanding pore-scale salt precipitation dynamics during CO2 sequestration. *Lab on a Chip*, 13(13):2508–2518, 2013.

[34] A C Hatch, J S Fisher, A R Tovar, A T Hsieh, R Lin, S L Pentoney, D L Yang, and A P Lee. 1-Million droplet array with wide-field fluorescence imaging for digital PCR. *Lab on a Chip*, 11(22):3838–3845, 2011.

[35] N S Gunda, B Bera, N K Karadimitriou, S K Mitra, and S M Hassanizadeh. Reservoir-on-a-chip (ROC): a new paradigm in reservoir engineering. *Lab on a Chip*, 11(22):3785–3792, 2011.

[36] Niall MacDowell, Nick Florin, Antoine Buchard, Jason Hallett, Amparo Galindo, George Jackson, Claire S Adjiman, Charlotte K Williams, Nilay Shah, and Paul Fennell. An overview of CO2 capture technologies. *Energy & Environmental Science*, 3(11):1645, 2010.

[37] S Pacala and R Socolow. Stabilization wedges: solving the climate problem for the next 50 years with current technologies. *Science*, 305(5686): 968–972, 2004.

[38] Jr Franklin M Orr. CO2 capture and storage: are we ready? *Energy & Environmental Science*, 2(5):449, 2009.

[39] J B West. Blood flow to the lung and gas exchange. *Anesthesiology*, 41 (2):124–138, 1974.

[40] Sameer P Nalawade, Francesco Picchioni, and L P B M Janssen. Supercritical carbon dioxide as a green solvent for processing polymer melts: Processing aspects and applications. *Progress in Polymer Science*, 31 (1):19–43, 2006.

[41] R Sun and T Cubaud. Dissolution of carbon dioxide bubbles and microfluidic multiphase flows. *Lab on a Chip*, 11(17):2924–2928, 2011.

[42] Jai Il Park, Zhihong Nie, Alexander Kumachev, and Eugenia Kumacheva. A microfluidic route to small CO2 microbubbles with narrow size distribution. *Soft Matter*, 6(3):630, 2010.

[43] Martin Sauzade and Thomas Cubaud. Initial microfluidic dissolution regime of CO2 bubbles in viscous oils. *Physical Review E*, 88(5), 2013.

[44] Thomas Cubaud and Thomas G Mason. Interacting viscous instabilities in microfluidic systems. *Soft Matter*, 8(41):10573, 2012.

[45] S G Lefortier, P J Hamersma, A Bardow, and M T Kreutzer. Rapid microfluidic screening of CO2 solubility and diffusion in pure and mixed solvents. *Lab on a Chip*, 12(18):3387–3391, 2012.

[46] M Abolhasani, M Singh, E Kumacheva, and A Gunther. Automated microfluidic platform for studies of carbon dioxide dissolution and solubility in physical solvents. *Lab on a Chip*, 12(9):1611–1618, 2012.

[47] V S Ajaev and G M Homsy. Modeling shapes and dynamics of confined bubbles. *Annual Review of Fluid Mechanics*, 38:277–307, 2006.

[48] E M Purcell. Life at low Reynolds number. *American Journal of Physics*, 45(1):3, 1977.

[49] Eric Lauga and Thomas R Powers. The hydrodynamics of swimming microorganisms. *Reports on Progress in Physics*, 72(9):96601, 2009.

[50] R Berker. *Intégration des équations du mouvement d'un fluide visqueux incompressible*, volume VIII/2, 1963.

[51] George M Whitesides and Abraham D Stroock. Flexible Methods for Microfluidics. *Physics Today*, 54(6):42, 2001.

[52] R Byron Bird, Warren E Stewart, and Edwin N Lightfoot. *Transport phenomena*, New York, 2nd, wiley edition, 2002. ISBN 0471410772 (cloth alk. paper).

[53] T M Squires and S R Quake. Microfluidics: Fluid physics at the nanoliter scale. *Reviews of Modern Physics*, 77(3):977–1026, 2005.

[54] R Aris. On the Dispersion of a Solute in a Fluid Flowing through a Tube. *Proceedings of the Royal Society of London Series a-Mathematical and Physical Sciences*, 235(1200):67–77, 1956.

[55] G Taylor. Dispersion of Soluble Matter in Solvent Flowing Slowly through a Tube. *Proceedings of the Royal Society of London Series a-Mathematical and Physical Sciences*, 219(1137):186–203, 1953.

[56] V Hessel, H Lowe, and F Schonfeld. Micromixers - a review on passive and active mixing principles. *Chemical Engineering Science*, 60(8-9): 2479–2501, 2005.

[57] J B Knight, A Vishwanath, J P Brody, and R H Austin. Hydrodynamic focusing on a silicon chip: Mixing nanoliters in microseconds. *Physical Review Letters*, 80(17):3863–3866, 1998.

[58] H Song and R F Ismagilov. Millisecond kinetics on a microfluidic chip using nanoliters of reagents. *Journal of the American Chemical Society*, 125(47):14613–14619, 2003.

[59] B Penth. Superior characteristics - Non-blocking microreactor for process engineering. *Chemie Ingenieur Technik*, 72(7):56, 2000.

[60] L Pollack, M W Tate, N C Darnton, J B Knight, S M Gruner, W A Eaton, and R H Austin. Compactness of the denatured state of a fast-folding protein measured by submillisecond small-angle x-ray scattering. *Proceedings of the National Academy of Sciences of the United States of America*, 96(18):10115–10117, 1999.

[61] J DeMello and A DeMello. Microscale reactors: nanoscale products. *Lab on a Chip*, 4(2):11N–15N, 2004.

[62] V Hessel, P Angeli, A Gavriilidis, and H Lowe. Gas-liquid and gas-liquid-solid microstructured reactors: Contacting principles and applications. *Industrial & Engineering Chemistry Research*, 44(25):9750–9769, 2005.

[63] D Ahmed, X L Mao, J J Shi, B K Juluri, and T J Huang. A millisecond micromixer via single-bubble-based acoustic streaming. *Lab on a Chip*, 9(18):2738–2741, 2009.

[64] B Zhao, J S Moore, and D J Beebe. Surface-directed liquid flow inside microchannels. *Science*, 291(5506):1023–1026, 2001.

[65] F Mugele and J C Baret. Electrowetting: From basics to applications. *Journal of Physics-Condensed Matter*, 17(28):R705–R774, 2005.

[66] A Sidorenko, T Krupenkin, and J Aizenberg. Controlled switching of the wetting behavior of biomimetic surfaces with hydrogel-supported nanostructures. *Journal of Materials Chemistry*, 18(32):3841–3846, 2008.

[67] D Huh, A H Tkaczyk, J H Bahng, Y Chang, H H Wei, J B Grotberg, C J Kim, K Kurabayashi, and S Takayama. Reversible switching of high-speed air-liquid two-phase flows using electrowetting-assisted flow-pattern change. *Journal of the American Chemical Society*, 125(48): 14678–14679, 2003.

[68] T Cubaud, U Ulmanella, and C M Ho. Two-phase flow in microchannels with surface modifications. *Fluid Dynamics Research*, 38(11):772–786, 2006.

[69] M Abkarian, A B Subramaniam, S H Kim, R J Larsen, S M Yang, and H A Stone. Dissolution arrest and stability of particle-covered bubbles. *Physical Review Letters*, 99(18):188301, 2007.

[70] M Hashimoto, P Garstecki, and G M Whitesides. Synthesis of composite emulsions and complex foams with the use of microfluidic flow-focusing devices. *Small*, 3(10):1792–1802, 2007.

[71] B P Binks and S O Lumsdon. Pickering emulsions stabilized by monodisperse latex particles: Effects of particle size. *Langmuir*, 17(15):4540–4547, 2001.

[72] A Groisman, M Enzelberger, and S R Quake. Microfluidic memory and control devices. *Science*, 300(5621):955–958, 2003.

[73] P Garstecki, M J Fuerstman, H A Stone, and G M Whitesides. Formation of droplets and bubbles in a microfluidic T-junction-scaling and mechanism of break-up. *Lab on a Chip*, 6(3):437–446, 2006.

[74] L L A Adams, Thomas E Kodger, Shin-Hyun Kim, Ho Cheng Shum, Thomas Franke, and David A Weitz. Single step emulsification for the generation of multi-component double emulsions. *Soft Matter*, 8(41): 10719, 2012.

[75] A R Abate, P Mary, V van Steijn, and D A Weitz. Experimental validation of plugging during drop formation in a T-junction. *Lab on a Chip*, 12(8):1516–1521, 2012.

[76] N Shao, A Gavriilidis, and P Angeli. Flow regimes for adiabatic gasâĂŞliquid flow in microchannels. *Chemical Engineering Science*, 64 (11):2749–2761, 2009.

[77] T Cubaud and C M Ho. Transport of bubbles in square microchannels. *Physics of Fluids*, 16(12):4575–4585, 2004.

[78] P Sobieszuk, J Aubin, and R Pohorecki. Hydrodynamics and Mass Transfer in Gas-Liquid Flows in Microreactors. *Chemical Engineering & Technology*, 35(8):1346–1358, 2012.

[79] M T Kreutzer, F Kapteijn, J A Moulijn, and J J Heiszwolf. Multiphase monolith reactors: Chemical reaction engineering of segmented flow in microchannels. *Chemical Engineering Science*, 60(22):5895–5916, 2005.

[80] H A Stone, A D Stroock, and A Ajdari. Engineering flows in small devices: Microfluidics toward a lab-on-a-chip. *Annual Review of Fluid Mechanics*, 36(1):381–411, 2004.

[81] T Taha and Z F Cui. CFD modelling of slug flow inside square capillaries. *Chemical Engineering Science*, 61(2):665–675, 2006.

[82] W K Lewis and W G Whitman. Principles of gas absorption. *Industrial and Engineering Chemistry*, 16:1215–1220, 1924.

[83] F Fairbrother and A E Stubbs. Studies in electro-endosmosis Part VI The "bubble-tube" method of measurement. *Journal of the Chemical Society*, pages 527–529, 1935.

[84] G I Taylor. Deposition of a Viscous Fluid on the Wall of a Tube. *Journal of Fluid Mechanics*, 10(2):161–165, 1961.

[85] H L Goldsmith and S G Mason. The Movement of Single Large Bubbles in Closed Vertical Tubes. *Journal of Fluid Mechanics*, 14(1):42–58, 1962.

[86] B G Cox. An Experimental Investigation of the Streamlines in Viscous Fluid Expelled from a Tube. *Journal of Fluid Mechanics*, 20(2):193–200, 1964.

[87] T C Thulasidas, M A Abraham, and R L Cerro. Flow patterns in liquid slugs during bubble-train flow inside capillaries. *Chemical Engineering Science*, 52(17):2947–2962, 1997.

[88] F P Bretherton. The Motion of Long Bubbles in Tubes. *Journal of Fluid Mechanics*, 10(2):166–188, 1961.

[89] W B Kolb and R L Cerro. Coating the inside of a Capillary of Square Cross-Section. *Chemical Engineering Science*, 46(9):2181–2195, 1991.

[90] W Blake Kolb and Ramon L Cerro. The motion of long bubbles in tubes of square cross section. *Physics of Fluids A: Fluid Dynamics*, 5(7):1549, 1993.

[91] T C Thulasidas, M A Abraham, and R L Cerro. Bubble-train flow in capillaries of circular and square cross section. *Chemical Engineering Science*, 50(2):183–199, 1995.

[92] Andrew L Hazel and Matthias Heil. The steady propagation of a semi-infinite bubble into a tube of elliptical or rectangular cross-section. *Journal of Fluid Mechanics*, 470, 2002.

[93] H Wong, C J Radke, and S Morris. The Motion of Long Bubbles in Polygonal Capillaries .2. Drag, Fluid Pressure and Fluid-Flow. *Journal of Fluid Mechanics*, 292:95–110, 1995.

[94] H Wong, C J Radke, and S Morris. The Motion of Long Bubbles in Polygonal Capillaries .1. Thin-Films. *Journal of Fluid Mechanics*, 292: 71–94, 1995.

[95] J Ratulowski and H C Chang. Transport of Gas-Bubbles in Capillaries. *Physics of Fluids a-Fluid Dynamics*, 1(10):1642–1655, 1989.

[96] H L Goldsmith and S G Mason. The flow of suspensions through tubes. II. Single large bubbles. *Journal of Colloid Science*, 18(3):237–261, 1963.

[97] M J Martinez and K S Udell. Axisymmetric creeping motion of drops through a periodically constricted tube. 197:222–234, 1990.

[98] W L Olbricht and D M Kung. The Deformation and Breakup of Liquid-Drops in Low Reynolds-Number Flow through a Capillary. *Physics of Fluids a-Fluid Dynamics*, 4(7):1347–1354, 1992.

[99] Rolf K Edvinsson and Said Irandoust. Finite-element analysis of Taylor flow. *Aiche Journal*, 42(7):1815–1823, 1996.

[100] MariÌĄa D Giavedoni and Fernando A Saita. The rear meniscus of a long bubble steadily displacing a Newtonian liquid in a capillary tube. *Physics of Fluids*, 11(4):786, 1999.

[101] M Kreutzer. *Hydrodynamics of taylor flow in capillaries and monolith reactors*. PhD thesis, 2003.

[102] Hui Liu, Chippla O Vandu, and Rajamani Krishna. Hydrodynamics of Taylor Flow in Vertical Capillaries:Âă Flow Regimes, Bubble Rise Velocity, Liquid Slug Length, and Pressure Drop. *Industrial & Engineering Chemistry Research*, 44(14):4884–4897, 2005.

[103] Petr Zaloha, Jiri Kristal, Vladimir Jiricny, Norbert Völkel, Catherine Xuereb, and Joelle Aubin. Characteristics of liquid slugs in gasâĂŞliquid Taylor flow in microchannels. *Chemical Engineering Science*, 68(1):640–649, 2012.

[104] J M Prausnitz, Ruediger N Lichtenthaler, and Edmundo Gomes de Azevedo. *Molecular thermodynamics of fluid-phase equilibria*, Upper Saddle River, N.J., 3rd edition, 1999. ISBN 0139777458.

[105] F L Smith and A H Harvey. Avoid common pitfalls when using Henry's law. *Chemical Engineering Progress*, 103(9):33–39, 2007.

[106] N Nernst. Theory on the reaction rate in heterogenous systems. *Zeitschrift Fur Physikalische Chemie–Stochiometrie Und Verwandtschaftslehre*, 47(1):52–55, 1904.

[107] R Higbie. The rate of absorption of a pure gas into a still liquid during short periods of exposure. *Transactions of the American Institute of Chemical Engineers*, 31:365–389, 1935.

[108] P V Danckwerts. Significance of Liquid-Film Coefficients in Gas Absorption. *Industrial and Engineering Chemistry*, 43(6):1460–1467, 1951.

[109] E L Cussler. *Diffusion, mass transfer in fluid systems*, Cambridge Cambridgeshire ; New York, 1984. ISBN 052123171X.

[110] Pedro Miguel Pacheco Neves Carteado Mena. *Mass transfer and hydrodynamics in multiphase systems*. PhD thesis, 2005.

[111] PaweÅĆ Sobieszuk, Filip Ilnicki, and Ryszard Pohorecki. Contribution of Liquid- and Gas-Side Mass Transfer Coefficients to Overall Mass Transfer Coefficient in Taylor Flow in a Microreactor. *Chemical and Process Engineering*, 35(1), 2014.

[112] Jean-Claude Charpentier. Mass-Transfer Rates in Gas-Liquid Absorbers and Reactors. 11:1–133, 1981.

[113] E Dluska, S Wronski, and T Ryszczuk. Interfacial area in gas-liquid Couette-Taylor flow reactor. *Experimental Thermal and Fluid Science*, 28(5):467–472, 2004.

[114] F K Kies, B Benadda, and M Otterbein. Experimental study on mass transfer of a co-current gas-liquid contactor performing under high gas velocities. *Chemical Engineering and Processing*, 43(11):1389–1395, 2004.

[115] A Heyouni, M Roustan, and Z Do-Quang. Hydrodynamics and mass transfer in gas-liquid flow through static mixers. *Chemical Engineering Science*, 57(16):3325–3333, 2002.

[116] Jun Yue, Guangwen Chen, Quan Yuan, Lingai Luo, and Yves Gonthier. Hydrodynamics and mass transfer characteristics in gasâĂŞliquid flow through a rectangular microchannel. *Chemical Engineering Science*, 62 (7):2096–2108, 2007.

[117] J Yue, L G Luo, Y Gonthier, G W Chen, and Q Yuan. An experimental study of air-water Taylor flow and mass transfer inside square microchannels. *Chemical Engineering Science*, 64(16):3697–3708, 2009.

[118] Gorazd Berčič and Albin Pintar. The role of gas bubbles and liquid slug lengths on mass transport in the Taylor flow through capillaries. *Chemical Engineering Science*, 52(21-22):3709–3719, 1997.

[119] J M van Baten and R Krishna. CFD simulations of mass transfer from Taylor bubbles rising in circular capillaries. *Chemical Engineering Science*, 59(12):2535–2545, 2004.

[120] M Roudet, K Loubiere, C Gourdon, and M Cabassud. Hydrodynamic and mass transfer in inertial gas-liquid flow regimes through straight and meandering millimetric square channels. *Chemical Engineering Science*, 66(13):2974–2990, 2011.

[121] A Gunther and K F Jensen. Multiphase microfluidics: from flow characteristics to chemical and materials synthesis. *Lab on a Chip*, 6(12): 1487–1503, 2006.

[122] J G Santiago, S T Wereley, C D Meinhart, D J Beebe, and R J Adrian. A particle image velocimetry system for microfluidics. *Experiments in Fluids*, 25(4):316–319, 1998.

[123] M Mohammadi and K V Sharp. Experimental Techniques for Bubble Dynamics Analysis in Microchannels: A Review. *Journal of Fluids Engineering-Transactions of the Asme*, 135(2), 2013.

[124] H Song, D L Chen, and R F Ismagilov. Reactions in droplets in microflulidic channels. *Angewandte Chemie-International Edition*, 45(44): 7336–7356, 2006.

[125] Joëlle Aubin, Montse Ferrando, and Vladimir Jiricny. Current methods for characterising mixing and flow in microchannels. *Chemical Engineering Science*, 65(6):2065–2093, 2010.

[126] Carsten Cramer, Peter Fischer, and Erich J Windhab. Drop formation in a co-flowing ambient fluid. *Chemical Engineering Science*, 59(15): 3045–3058, 2004.

[127] T Thorsen, R W Roberts, F H Arnold, and S R Quake. Dynamic pattern formation in a vesicle-generating microfluidic device. *Physical Review Letters*, 86(18):4163–4166, 2001.

[128] Shelley L Anna, Nathalie Bontoux, and Howard A Stone. Formation of dispersions using âĂIJflow focusingâĂİ in microchannels. *Applied Physics Letters*, 82(3):364, 2003.

[129] A M Ganan-Calvo and J M Gordillo. Perfectly monodisperse microbubbling by capillary flow focusing. *Physical Review Letters*, 87(27 Pt 1): 274501, 2001.

[130] C N Baroud, F Gallaire, and R Dangla. Dynamics of microfluidic droplets. *Lab on a Chip*, 10(16):2032–2045, 2010.

[131] S Prakash and S Kumar. Fabrication of microchannels: A review. *Proceedings of the Institution of Mechanical Engineers, Part B: Journal of Engineering Manufacture*, 2014.

[132] D C Duffy, J C McDonald, O J A Schueller, and G M Whitesides. Rapid prototyping of microfluidic systems in poly(dimethylsiloxane). *Analytical Chemistry*, 70(23):4974–4984, 1998.

[133] T Cubaud, M Sauzade, and R Sun. CO(2) dissolution in water using long serpentine microchannels. *Biomicrofluidics*, 6(2):22002–220029, 2012.

[134] S C Talmage and C J Gobler. Effects of past, present, and future ocean carbon dioxide concentrations on the growth and survival of larval shellfish. *Proceedings of the National Academy of Sciences of the United States of America*, 107(40):17246–17251, 2010.

[135] T Cubaud, M Tatineni, X Zhong, and C M Ho. Bubble dispenser in microfluidic devices. *Phys Rev E Stat Nonlin Soft Matter Phys*, 72(3 Pt 2):37302, 2005.

[136] N Dietrich, S Poncin, N Midoux, and H Z Li. Bubble formation dynamics in various flow-focusing microdevices. *Langmuir*, 24(24):13904–13911, 2008.

[137] D D Meng, T Cubaud, C M Ho, and C J Kim. A methanol-tolerant gas-venting microchannel for a microdirect methanol fuel cell. *Journal of Microelectromechanical Systems*, 16(6):1403–1410, 2007.

[138] C C Liu, J A Thompson, and H H Bau. A membrane-based, high-efficiency, microfluidic debubbler. *Lab on a Chip*, 11(9):1688–1693, 2011.

[139] J Tan, Y C Lu, J H Xu, and G S Luo. Mass transfer performance of gas-liquid segmented flow in microchannels. *Chemical Engineering Journal*, 181:229–235, 2012.

[140] R Battino, T R Rettich, and T Tominaga. The Solubility of Nitrogen and Air in Liquids. *Journal of Physical and Chemical Reference Data*, 13(2):563–600, 1984.

[141] M B King, K Kassim, and H Alnajjar. Solubilities of Carbon-Dioxide, Hydrogen-Sulfide and Propane in Some Normal Alkane Solvents .2. Correlation of Data at 25-Degrees-C in Terms of Solubility Parameters and Regular Solution Theory. *Chemical Engineering Science*, 32(10):1247–1252, 1977.

[142] D Gómez-Díaz and J M Navaza. Gas/liquid mass transfer processes in a carbon dioxide/alkane system. *Journal of Chemical Technology & Biotechnology*, 80(7):812–818, 2005.

[143] J Guzman and L Garrido. Determination of carbon dioxide transport coefficients in liquids and polymers by NMR spectroscopy. *Journal of Physical Chemistry B*, 116(20):6050–6058, 2012.

[144] John B West. *Respiratory physiology : the essentials*, Philadelphia, 9th edition, 2012. ISBN 9781609136406 1609136403.

[145] B Jahne and H Haussecker. Air-water gas exchange. *Annual Review of Fluid Mechanics*, 30:443–468, 1998.

[146] H M Gonnermann and M Manga. The fluid mechanics inside a volcano. *Annual Review of Fluid Mechanics*, 39(1):321–356, 2007.

[147] Hossein Fadaei, Brent Scarff, and David Sinton. Rapid Microfluidics-Based Measurement of CO2Diffusivity in Bitumen. *Energy & Fuels*, 25 (10):4829–4835, 2011.

[148] D L Tomasko, H B Li, D H Liu, X M Han, M J Wingert, L J Lee, and K W Koelling. A review of CO(2) applications in the processing of polymers. *Industrial & Engineering Chemistry Research*, 42(25):6431–6456, 2003.

[149] Frank M White. *Viscous fluid flow*, New York, 2nd edition, 1991. ISBN 0070697124.

[150] G K Batchelor. *An introduction to fluid dynamics*, Cambridge, 1967.

[151] J R Royer, J M DeSimone, and S A Khan. Carbon dioxide-induced swelling of poly(dimethylsiloxane). *Macromolecules*, 32(26):8965–8973, 1999.

[152] F W Wu, L Li, Z H Xu, S J Tan, and Z B Zhang. Transport study of pure and mixed gases through PDMS membrane. *Chemical Engineering Journal*, 117(1):51–59, 2006.

[153] B K H Yen, A Gunther, M A Schmidt, K F Jensen, and M G Bawendi. A microfabricated gas-liquid segmented flow reactor for high-temperature synthesis: The case of CdSe quantum dots. *Angewandte Chemie-International Edition*, 44(34):5447–5451, 2005.

[154] H Zhang, E Tumarkin, R Peerani, Z Nie, R M A Sullan, G C Walker, and E Kumacheva. Microfluidic production of biopolymer microcapsules with controlled morphology. *Journal of the American Chemical Society*, 128(37):12205–12210, 2006.

[155] E Talu, M M Lozano, R L Powell, P A Dayton, and M L Longo. Long-term stability by lipid coating monodisperse microbubbles formed by a flow-focusing device. *Langmuir*, 22(23):9487–9490, 2006.

[156] J Kobayashi, Y Mori, K Okamoto, R Akiyama, M Ueno, T Kitamori, and S Kobayashi. A microfluidic device for conducting gas-liquid-solid hydrogenation reactions. *Science*, 304(5675):1305–1308, 2004.

[157] O A Basaran. Small-scale free surface flows with breakup: Drop formation and emerging applications. *Aiche Journal*, 48(9):1842–1848, 2002.

[158] Taotao Fu, Youguang Ma, Denis Funfschilling, and Huai Z Li. Bubble formation and breakup mechanism in a microfluidic flow-focusing device. *Chemical Engineering Science*, 64(10):2392–2400, 2009.

[159] Yutao Lu, Taotao Fu, Chunying Zhu, Youguang Ma, and Huai Z Li. Scaling of the bubble formation in a flow-focusing device: Role of the liquid viscosity. *Chemical Engineering Science*, 105:213–219, 2014.

[160] W L Olbricht and L G Leal. The creeping motion of immiscible drops through a converging/diverging tube. *Journal of Fluid Mechanics*, 134 (-1):329, 1983.

[161] D R Graham and J J L Higdon. Oscillatory flow of droplets in capillary tubes. Part 1. Straight tubes. *Journal of Fluid Mechanics*, 425:31–53, 2000.

[162] J Burton, R Waldrep, and P Taborek. Scaling and Instabilities in Bubble Pinch-Off. *Physical Review Letters*, 94(18), 2005.

[163] Piotr Garstecki, Howard Stone, and George Whitesides. Mechanism for Flow-Rate Controlled Breakup in Confined Geometries: A Route to Monodisperse Emulsions. *Physical Review Letters*, 94(16), 2005.

[164] S T Thoroddsen, T G Etoh, and K Takehara. Experiments on bubble pinch-off. *Physics of Fluids*, 19(4):42101, 2007.

[165] H A Stone and L G Leal. Breakup of Concentric Double Emulsion Droplets in Linear Flows. *Journal of Fluid Mechanics*, 211:123–156, 1990.